Superfluorescence from Erbium-doped Crystals

Federico Chiossi

Doctoral Thesis

Department of Physics and Astronomy
UNIVERSITY OF PADOVA

Supervisor:

Dr. Caterina Braggio

Co-supervisor:

Prof. Francesco A. Borghesani

December 2019

Acknowledgements

It is my pleasure to acknowledge the following persons for their support and help that was crucial for this work.

First and foremost, I shall thank my supervisor Dr. Caterina Braggio for her extraordinary guidance, expertise and dedication. I am grateful to my co-supervisor Prof. Francesco Armando Borghesani who introduced me to the scientific research, deepening several aspects of the atomic and molecular physics. A special thanks to Prof. Giovanni Carugno who has taught me so much about experimental physics and whose dreaming big is an inspiration to me.

I would like to acknowledge my colleague Dr. Alen Khanbekyan for the help during the experiments. In addition, I would like to express my gratitude towards Fulvio Calaon and Enrico Berto for the technical assistance, Prof. Alberto di Lieto and Prof. Mauro Tonelli at Pisa University for providing us with the fluoride crystals and Dr. Sergey Vasiukov for the several discussions.

I would also like to thank my close friends and laboratory mates Marco Guarise, Nicoló Crescini and Sebastiano Gallo for their company and support in these years.

Contents

Abbreviations

cw	**C**ontinuous **W**ave
MD	**M**acroscopic **D**ipole
PD	**P**hoto**d**iode
SF	**S**uper**f**luorescence
SR	**S**uper**r**adiance

Introduction

RE-doped crystals are widely used as scintillators for high energy radiation, but in this thesis we explore unconventional detection schemes, motivated by searches of the QDC Axion, one of the most promising Dark Matter particle candidate in the (1 μeV-1 meV) energy range. In 2014 Pierre Sikivie, the inventor of the axion haloscope, proposed to have the axion absorbed in the atomic transition between Zeeman sub-levels of the ground state when their splitting energy is tuned on resonance with axion mass by an external magnetic field [1]. The rate of axion absorption that he calculated for a mole of target atoms is smallest, and to improve the detector sensitivity he suggested to exploit the upconversion, a concept first introduced by the Nobel prize N. Bloembergen [2] for the infrared photons sensing. In the so called infrared quantum counter a strong radiation source drives the transition between a low energetic level to a higher emitting one. In this way, a low energy deposition event, such as the axion absorption, is converted to a photon emission in visible range, which can be efficiently detected. In his theoretical work, Sikivie assumed a unitary upconversion efficiency, neglecting the possible processes which might generate spurious signals due to the pump laser.

In the first part of this work, we consider to use Erbium ions doped into crystals as axion targets and analyze the upconversion process in terms of efficiency, required pump laser intensity and its role as noise source. The goal is to determine the effective feasibility of such detector by assessing if the required sensitivity can be achieved. To accomplish this task, we have carried out preliminary spectroscopic measurements on Erbium-doped crystals at liquid helium temperatures and under a magnetic field.

Even though the upconversion process could be efficiently accomplished with a laser intensity of $\sim$1 W/cm^2, the spurious laser induced fluorescence observed in the investigated crystals may affect their applicability to the axion detection. In particular, the laser photon-crystal lattice interaction and the presence of the impurities are the greatest impediments to the feasibility of the Sikivie scheme.

During the high resolution measurements on Er-doped crystals, we observed strong fluctuations of the continuous laser induced fluorescence that we have subsequently attributed to superfluorescence (SF). SF is a strongly directional emission of fast,

coherent photon bunches arising from the spontaneous formation of a macroscopic dipole in largely inverted media. In fact, the synchronization of the atomic dipoles is carried out through the common electromagnetic field of emitted radiation and in this coupled system, each single dipole is correlated with all the others. The atomic transition rate is enhanced by a factor μN, with N the number of correlated atoms and μ a geometrical factor that accounts for interference effects within the volume of the atomic ensemble. The cooperative radiative decay results in the emission of coherent photon bunches whose peak intensity is proportional to μN^2, and their duration scales with $(\mu N)^{-1}$.

We have thoroughly study SF from Erbium doped crystals in several aspects such as the photon bunches propagation properties and the dynamics of macroscopic dipole formation. SF is the subject of the second part of this thesis, that is organized as follows.

Chapter 1 is intended to provide the basic theory of rare earth spectroscopy relevant for this work. It includes a derivation of electronic level structure, as well as the description of the main relaxation processes and the factors that determine the optical coherence time of RE ions transitions.

Chapter 2 introduces the challenge of the QCD axion detection and the scheme we want to investigate. After a brief outline of the experimental apparatus, the first spectroscopic measurements on the Er-doped crystals at (1.6-4.2) K and the discussion about the feasibility of the axion detection scheme are presented.

In Chapter 3, few selected models are introduced to give a theoretical description of SF. Starting from the first concept of superradiance proposed by R. H. Dicke[3], we focus on the so-called "Dicke model" and later on we discuss the equations derived from both semi-classical and quantum mechanical approaches, describing the evolution of coherent emission intensity and the macroscopic dipole formation.

In Chapter 4, we propose a review of the SF experiments reported in the literature. The aim of the chapter is to provide the experimental background in SF to better appreciate the relevance of the results presented in this work.

In Chapter 5, we present the clear signatures of SF from Erbium-doped Y_2SiO_5 and $YLiF_4$ crystals. The process is observed for two infrared transitions and involves the remarkable number of $\sim 10^{12}$ Erbium ions, accelerating the radiative decay by millions times. Several aspects of SF are thoroughly investigated and a good agreement with the theoretical expectation is reported.

We believe that the present results of the spontaneous formation of a large macroscopic dipole in a compact medium such as RE-doped crystals and its hundred nanoseconds-long lifetime represent an ideal test-bed for future experiments regarding cooperative processes.

The $N-$enhancement in the light-matter interaction provided by the correlation among the emitters could be applied in many fields. Recently, the cooperative absorption has been demonstrated for few atoms in a cavity, taking a step towards the realization of efficient light-energy harvesting, advanced light-matter quantum interfaces and weak-signal sensors [4].

Macroscopic dipole is of interest also for particle physicists as the rate of extremely rare processes could be strongly increased via coherent amplification [5]. For instance, two photon emission has been successfully observed from the first vibrational level of para-H_2, where the macroscopic coherent state was provided by the stimulated Raman scattering process [6, 7]. A similar approach has been recently proposed also for axion detection [8], whereas the two neutrino pair emission in RE ions transitions [9, 10], and in Er^{3+} transitions in particular [11], could be probed to determine the remaining neutrino properties, such as the absolute mass value and mass type (Majorana or Dirac).

Chapter 1

Rare earth properties

The term "Rare Earths" (RE) is used to indicate the chemical elements ranging from Lantanum (Z=57) to Lutetium (Z=71), called Lantanides, that share similar electrochemical properties. Scandium (Z=21) and Yttrium (Z=39) are sometimes included as well.

These elements are strongly electropositive and 3+ is the most common oxidation state in their countless compounds for luminescent and magnetic devices. Their electronic configuration is [Xe]$4f^N$ whereby the $4f$ shell is progressively filled from $N = 0$ to $N = 14$ as the atomic number increases. The $4f$ electrons wavefunctions of the RE are compressed by the outer and less localized $5s^2$-$5p^6$ orbitals of the [Xe] configuration. Therefore, the $4f-$electrons are shielded from the environment endowing the RE-doped materials with their remarkable optical properties, such as narrow optical transition linewidths. Moreover, up to 7 unpaired electrons can occupy the $4f$ orbital structure and the resulting high magnetic moment can be exploited to realize permanent magnets.

All trivalent Lantanides ions have the same primary bonding electrons belonging to the $5s^2$-$5p^6$ shells and, along with Y^{3+} and Sc^{3+}, are substitutional in stoichiometric compounds. Actually, many laser and scintillator single crystals are based on RE-doped materials and a very high optical quality can be obtained provided that the strain due to doping does not comprimise the lattice integrity.

This chapter aims at familiarizing the reader with the properties of RE ions that are relevant for the present thesis. The derivation of their energy level structure is presented and their main relaxation processes are described together with the mechanisms that influence the ions transition linewidth. A final section is devoted to the materials used in this work, with a focus on their optical coherence time.

1.1 Energy levels structure

In this section the main interactions that give rise to the complex energy level structure (see for instance Fig. 1.1) of the RE ions are analyzed. A guideline to solve the Schrődinger equation for the N $4f$-electrons and to derive the level energy and wavefunction is introduced, whereas a detailed description of the calculation method can be found elsewhere [12–14].

The energy of each $4f$ RE level varies within a few percent from a crystal to another, thanks to the $5s^2$-$5p^6$ shells screening action on the $4f$ electrons. An approximated free ion Hamiltonian can thus be written to calculate a basis of eigenfunctions that roughly provides the energy values of all $4f$ levels. Higher order hamiltonian terms are subsequently added and handled in the framework of perturbation theory. These terms are expressed as a weighted sum of tensor operators whose parameters are partially obtained by fitting experimental data. In this way, all the level energy values can be estimated with a high accuracy.

The $5d$ electrons are not affected by the same screening effects as the $4f$ electrons and broad $4f - 5d$ transition linewidths are observed, which are not interesting for the purposes of the present work.

1.1.1 Central field Hamiltonian

The most relevant contributions to the Hamiltonian for a RE^{3+} free ion correspond to the kinetic and potential energies of electrons in the field of the nucleus and the electron-electron repulsive Coulomb interaction. We can define the effective Hamiltonian:

$$\begin{aligned} H &= H_0 + H_{\mathrm{e-e}} = \\ &= \left[-\frac{\hbar^2}{2m} \sum_{i=1}^{N} \nabla_i - \frac{1}{4\pi\epsilon_0} \sum_{i=1}^{N} \frac{Z^* e}{r_i} \right] + \frac{1}{4\pi\epsilon_0} \sum_{i<j} \frac{e^2}{r_{ij}} \end{aligned} \tag{1.1}$$

where e and m are the electron charge and mass, respectively. Z^*e is the effective nuclear charge, r_i and $r_{ij} = |r_i - r_j|$ are the radial coordinates of the i-th electron and its distance from the j-th one. The summations are performed on the N $4f$ electrons as the contribution of the other closed configurations can be neglected to a first approximation. Unfortunately, Eq. 1.1 cannot be solved analytically if $N > 1$ because the $H_{\mathrm{e-e}}$ term includes the relative positions of the electrons. In order to overcome this problem, H is replaced by an effective, central-field

Hamiltonian:

$$\begin{aligned} H' &= H_0 + \langle H_{\mathrm{e-e}} \rangle = \\ &= -\frac{\hbar^2}{2m}\sum_{i=1}^{N}\nabla_i - \frac{1}{4\pi\epsilon_0}\sum_{i=1}^{N}\frac{Z^*e}{r_i} + \left\langle \frac{1}{4\pi\epsilon_0}\sum_{i,i<j}\frac{e^2}{r_{ij}} \right\rangle = \\ &= \sum_{i=1}^{N}\left[-\frac{\hbar^2}{2m}\nabla_i - U(r_i)\right], \end{aligned} \tag{1.2}$$

where the $\langle\rangle$ indicates the spherically symmetric component and U is the potential energy experienced by the ith-electron at r_i. The asymmetric contribution of $H_{\mathrm{e-e}}$ is actually small enough to be treated as a perturbation. Likewise to the Hydrogen Hamiltonian, the solution of Eq. 1.2 for each electron can be calculated independently from all remaining ones, and the obtained wavefunction can be decomposed into a radial, angular, and spin components

$$\Psi_{n,l,m_l,m_s}(r,\theta,\phi) = \frac{1}{r}R_{nl}(r)Y_{lm_l}(\theta,\phi)\sigma(m_s), \tag{1.3}$$

in which n, l, m_l, m_s, and Y_{lm_l} are the well-known quantum numbers and the spherical harmonics. The radial function R_{nl} is the only component that depends on the central field potential energy $U(r)$ but it is common to all $4f$ levels and does not influence their relative energy. Finally, a complete eigenfunctions set for a N-electrons system is obtained by using the Slater determinant with the Ψ-wavefunction as parameters.

As the Hamiltonian H' commutes with the total spin angular momentum $\mathbf{S}$, the total orbital angular momentum $\mathbf{L}$, the total angular momentum $\mathbf{J}$, and its projection on z-axis $\mathbf{M}$, the RE ions eigenfunctions are usually expressed by using the notation $|nl\gamma\mathrm{LSJM}\rangle$, in which $\mathrm{L, S, J, M}$ are the good total quantum numbers related to the momentum operator and the "seniority number" γ is introduced to remove the LS-degeneracy in a few cases [13].

The spherically symmetric field does not remove the configuration degeneracy but introduces a energy separation of the order of $10^5\,\mathrm{cm}^{-1}$ between the $4f$ from the $5d$ levels.

1.1.2 Free ion Hamiltonian

The main perturbation terms in the Hamiltonian H' are the non-central components of the electron-electron repulsion and the spin-orbit interaction, which are

respectively defined as:

$$H_{\mathrm{e-e}}^{NC} = \frac{1}{4\pi\epsilon_0}\sum_{i,i<j}\frac{e^2}{r_{ij}} - \left\langle \frac{1}{4\pi\epsilon_0}\sum_{i,i<j}\frac{e^2}{r_{ij}} \right\rangle \qquad H_{\mathrm{SO}} = \sum_{i=1}^{N}\frac{1}{2m^2c^2r_i}\frac{d\mathrm{U}(r_i)}{dr_i}(\mathbf{s}_i\cdot\mathbf{l}_i) \quad (1.4)$$

where $\mathbf{s}_i$ and $\mathbf{l}_i$ are the spin and the orbital angular momentum of the i-th electron. With the introduction of these terms, neither the LS-coupling nor the jj-coupling schemes can be applied because $H_{\mathrm{SO}} + H_{\mathrm{e-e}}^{NC}$ does commute with neither L nor S nor with the total momentum of any electrons. As a result, the wavefunctions $|nl\gamma\mathrm{LSJM}\rangle$ are not eigenfunctions for the Hamiltonian $H' + H_{\mathrm{SO}} + H_{\mathrm{e-e}}^{NC}$. However, according to the perturbation theory and of the so-called "intermediate" LS-coupling, a set of eigenfunctions for this Hamiltonian can be obtained as a linear combination of pure LS-coupling $|nl\gamma\mathrm{LSJM}\rangle$ wavefunctions:

$$|nl\gamma[\mathrm{LS}]\mathrm{JM}\rangle = \sum_{\gamma,\mathrm{L}',\mathrm{S}'} a_{\gamma\mathrm{L}'\mathrm{S}'}\,|nl\gamma\mathrm{L}'\mathrm{S}'\mathrm{JM}\rangle \quad (1.5)$$

The LS symbols in brackets indicates the quantum numbers of the predominant pure Russell-Saunders state. It must be noted that the sum is performed only over the L, S and γ numbers as J and M are still good quantum numbers for the Hamiltonian $H' + H_{\mathrm{SO}} + H_{\mathrm{e-e}}^{NC}$.

Now, the determination of the eigenstates is reduced to search of the coefficients $a_{\gamma LS}$, that can be written as

$$a_{\gamma\mathrm{LS}} = \sum_{\gamma,\mathrm{L}',\mathrm{S}'} \langle nl\gamma[\mathrm{LS}]\mathrm{JM}|H_{\mathrm{e-e}}^{NC} + H_{\mathrm{SO}}|nl\gamma\mathrm{L}'\mathrm{S}'\mathrm{JM}\rangle \quad (1.6)$$

In order to determine these coefficients the perturbation terms must be expressed by one or more tensor operators. The detailed derivation and the relative matrix element calculation [12] go beyond the purposes of this section. We recall here that the eigenstates with different S and L numbers are separated in energy by $10^4\,\mathrm{cm}^{-1}$ because of the effect of the electron-electron repulsion interaction whereas the spin-orbit term removes the J-fold degeneracy by splitting the levels by $10^3\,\mathrm{cm}^{-1}$ to $10^4\,\mathrm{cm}^{-1}$.

The Hamiltonian $H_{\mathrm{free}} = H' + H_{\mathrm{SO}} + H_{\mathrm{e-e}}^{NC}$ predicts the energy values of free ions within a few hundreds of cm^{-1}. In order to improve the accuracy, it is necessary to account for more interactions, including spin-spin, spin-other-orbit, and, for $4f$ configurations with $N > 2$ electrons triplet interactions as well. The standard free ion Hamiltonian H_{free} is made up of several tensor operators and encompasses up to 23 free parameters that are usually obtained by a fit to the experimentally observed energy values.

1.1.3 Crystal field splitting

When RE ions are embedded in host crystals, they experience an electric field whose strength is of several MV/cm due to the surrounding charge distribution that breaks the spherical symmetry and removes the $(J+1)$-fold degeneracy, completely for the Kramers ions (even number of electrons in $4f$ shell) and partially for the non-Kramers ions (odd number of electrons). In the latter case each level is at least doubly degenerate.

The energy of a specific $4f$ level varies in a host material to another within the $10^2 - 10^3\,\mathrm{cm}^{-1}$ range due to the $5s^2$-$5p^6$ screening effect. Thus, the crystal-field interaction H_{CF} can be added to the free ion Hamiltonian as a small perturbation and can be treated as described in section 1.1.2 by introducing additional parameters for H_{CF} that depend on the symmetry of the ion site.

The main effect of the crystal field is the mixing of the state with different J and M quantum numbers, and the $4f$ eigenfunctions are of the following form:

$$|\gamma[\mathrm{LSJM}]\rangle = \sum_{\gamma,\mathrm{LSJM}} a(\gamma\mathrm{LSJM})\,|\gamma\mathrm{LSJM}\rangle \tag{1.7}$$

A good approximation that strongly reduces the computation time is to restrict the summation to the $4f$ configuration in a limited energy range.

The J-mixing significantly affects the optical transition strength, thereby determining consistent variations of the radiative lifetime and photon absorption cross section when the same RE is doping different host materials.

The Hamiltonian $H_{\mathrm{free}} + H_{\mathrm{CF}}$ is commonly adopted to estimate the energy levels of RE ions in an arbitrary crystal. An iterative least squares fitting procedure over some experimentally observed values is employed to fix the several free parameters of the Hamiltonian. In this way, a set of level eigenfunctions can be obtained and the complete $4f$ energy level scheme is calculated with less than a few cm^{-1} uncertainty. The $4f$ energy levels up to $50\,000\,\mathrm{cm}^{-1}$ for the trivalent Lantanides in LaF_3, as calculated by Carnall [15], are shown in Fig. 1.1

The levels are labelled by the notation LSJM or $^{2S+1}\mathrm{L}(\gamma)_{\mathrm{JM}}$ which indicate the dominant pure Russell-Saunders component[1]. A complete $4f$ level scheme up to $200\,000\,\mathrm{cm}^{-1}$ is reported in Ref. 16 but energy levels above the conduction band and the lowest $5d$ level are of little interest as their population is very quickly depleted by energy transfer processes.

[1] In this work we will often use the notation $^{2S+1}\mathrm{L_J(i)}$ where $i = 1, 2...$ labels the Stark levels of the manifold starting from the lowest one.

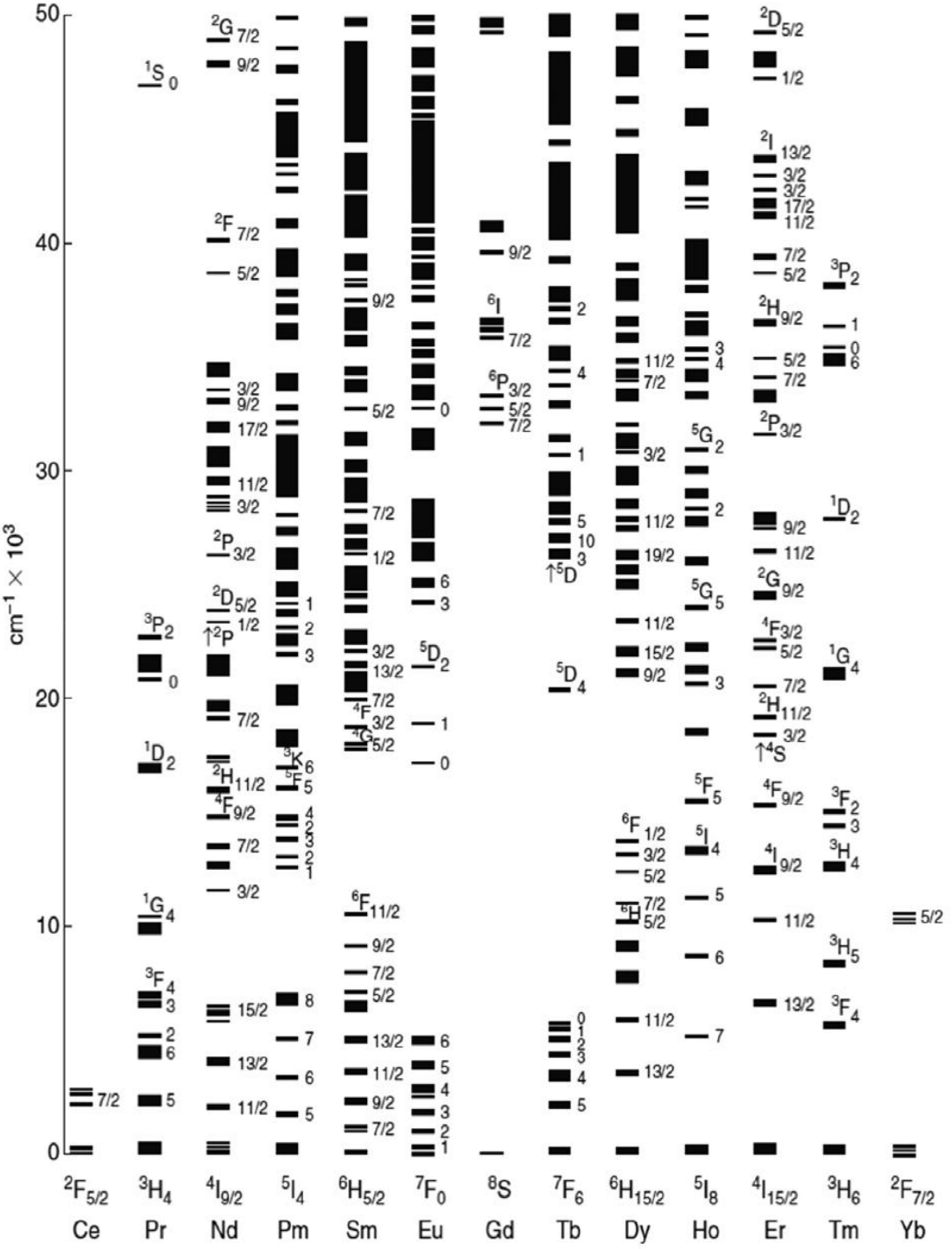

FIGURE 1.1: Energy level structure of RE^{+3}:LaF_3 calculated by Carnall [15].

1.1.4 Hyperfine splitting

Most of the RE ions are endowed with non-zero nuclear spin **I** whose interaction with the total electronic momentum **J** further splits the energy levels up to an extent of few GHz. The number of these hyperfine sublevels is therefore the smaller between (2J+1) and (2I+1). Each sublevel with atomic momentum $\mathbf{F} = \mathbf{J} + \mathbf{I}$ is (2F+1)-fold degenerate.

The sublevels separation is induced by the magnetic field $\sum_{i=1}^{N} \mathbf{B}_i$, generated by the unfilled $4f$ electrons at the nucleus position. This magnetic dipole interaction is thus given by:

$$H_I = -\sum_{i=1}^{N} \mathbf{B}_i \cdot \boldsymbol{\mu}_I = 2\mu_0 \sum_{i=1}^{N} \left(\frac{\mathbf{l_i} - \mathbf{s_i}}{r_i^3} + \frac{3\mathbf{r_i}(\mathbf{r_i} \cdot \mathbf{s})}{r_i^5} \right) \cdot \boldsymbol{\mu}_I \tag{1.8}$$

where $\boldsymbol{\mu}_I$ is the nuclear magnetic moment and μ_0 the vacuum permeability.

The hyperfine terms are always dealt with the second order perturbation theory, i.e., by assuming that their effects on the eigenfunction set of $H_{free} + H_{\mathrm{CF}}$ are negligible. A comprehensive discussion and the matrix element calculation for the hyperfine hamiltonian term can be found in Ref. 12, 13. It is worth noting that the hyperfine magnetic interaction is strongly reduced for non-Kramers ions in low symmetry crystal sites. In this cases, the electric quadrupole interaction becomes the dominant factor in determining the resultant hyperfine level structure. Actually, a hyperfine splitting of the order of some tens of MHz results from the electric quadrupole interaction of nuclei with $I > 1/2$ with the inhomogeneous electric field produced by the surrounding electrons. The magnetic interaction between the RE electrons and the nearby nuclei of the host crystal is also possible, but due to the $4f$ confinement the induced energy separation is less than few MHz on the spectral range.

1.1.5 Zeeman splitting

When the RE ion-doped crystals are exposed to an external static magnetic field **B** directed along the c crystal axis, the electronic Zeeman interaction can be written as:

$$H_{\mathrm{mag}} = g(\mathrm{LSJ})\mu_B \mathbf{J} \cdot \mathbf{B} \quad \text{with} \quad g(\mathrm{SLJ}) = 1 + \frac{\mathrm{J(J+1)} - \mathrm{L(L+1)} + \mathrm{S(S+1)}}{2\mathrm{J(J+1)}} \tag{1.9}$$

where μ_B is the electronic Bohr magneton and g(LSJ) is the Landé factor. By neglecting the Stark splitting, the intermediate coupling defined in Eq. 1.5 is usually

applied and the electronic Zeeman spitting is given at the first order by:

$$\begin{aligned}
&\langle\gamma[\mathrm{LS}]\mathrm{JM}|\, H_{\mathrm{mag}}\,|\gamma[\mathrm{LS}]\mathrm{JM}\rangle = \\
&= \mu_B \mathrm{B} \sum_{\gamma\mathrm{LS}} g(\mathrm{LSJ})|\,\langle\gamma[\mathrm{LS}]\mathrm{JM}|\gamma\mathrm{LSJM}\rangle\,|^2\,\langle\gamma\mathrm{LSJM}|\,\mathbf{M}\,|\gamma\mathrm{LSJM}\rangle = \\
&= \mu_B \mathrm{BM} \sum_{\gamma\mathrm{LS}} g(\mathrm{LSJ}) a^2_{\gamma\mathrm{LS}} = \bar{g}\mu_B \mathrm{B}
\end{aligned}$$

in which we have introduced the g-factor $\bar{g} = \sum a^2_{\gamma\mathrm{LS}} g(\mathrm{LSJ})$ that is the quantum number M multiplied by the weighted sum of g over all the levels with the same J quantum number. The singlet states of the non-Kramers ions in low symmetric crystals are shifted by applying the magnetic field whereas the twofold degeneracy of the Kramers ion characterized by the same absolute value |M| is removed by splitting the two levels symmetrically about the energy level at zero field.

The Zeeman interaction is not isotropic and when the magnetic field is not oriented along the c-axis it is expressed by

$$H_{\mathrm{mag}} = \mu_B \sum_{i=X,Y,Z} g_i B_i \mathrm{J}_i \tag{1.10}$$

where g_i, B_i and J_i are the Landé factors along the principal axes and the magnetic field and the total angular momentum operator components.

For high magnetic field intensity or when the separation energy between Stark levels is small, H_{mag} implies a non negligible mixing of the states that results in a nonlinear dependence of the Zeeman splitting on the magnetic field strength. This is not the case in the present experiments.

The degeneracy of the hyperfine levels with quantum number |I| is also removed by applying a magnetic field. However, as the nuclear Bohr magneton is 3 orders of magnitude smaller than the electronic one, the nuclear Zeeman splitting is of the order of 1 to 10 MHz/T, compared to (10-100) GHz/T range of the electronic splitting.

1.2 Relaxation processes

We have seen that RE-doped crystals have a complex energy level structure and several $4f \rightarrow 4f$ transitions of different energies could be employed for our studies. In this section, we want to discuss the relaxation processes that rule the levels lifetime and the photon emission quantum efficiency. Provided the re-absorption of the ion emission inside the crystals can be neglected, the measured lifetime τ

of a excited manifold is mainly determined by:

$$\frac{1}{\tau} = \frac{1}{\tau_0} + W^{\mathrm{MP}} + W^{\mathrm{AD}} \tag{1.11}$$

where τ_0 is the radiative lifetime and W^{MP} and W^{AD} are the multiphonon relaxation and the energy transfer rate, respectively. The effect of the last two term is to reduce the effective lifetime and altough they are undesired processes which quench the spontaneous emission, they could be exploited to indirectly populate lower energetic levels via non radiative steps.

1.2.1 Radiative transitions

The $4f \rightarrow 4f$ radiative transitions should be forbidden as they involve states with the same parity. However, the crystal field term induces coupling with the other configurations and the $4f$ states have also a small $5d$ wavefunction component that enables the transition. As a result, the characteristic radiative lifetime of $4f$ levels ranges between a few microseconds to several tens of milliseconds.

The calculation of the eigenfunctions described in the previous section not only gives the energy levels but allows also the calculation of the radiative transition rate between two $4f$ J-multiplets. A good estimation of the latter is provided by taking into account also the magnetic dipole, as the electric one is weak. According to the theory developed by Judd and Ofelt [17], the electric and magnetic dipole line strength for isotropic crystals is expressed as follows:

$$S^{\mathrm{ED}} = \sum_t \Omega_t |\left\langle [\mathrm{SLJ}] \right| \mathbf{U}^t \left| [\mathrm{S'L'J'}] \right\rangle|^2 \qquad (t = 2, 4, 6) \tag{1.12}$$

$$S^{\mathrm{MD}} = \left(\frac{\hbar}{2mc}\right)^2 \left|\left\langle [\mathrm{SLJ}] \right| \mathbf{L} + 2\mathbf{S} \left| [\mathrm{S'L'J'}] \right\rangle\right|^2 \tag{1.13}$$

where $\mathbf{U}^t$ is a tensor operator of rank t related to the dipole moment operator. The corresponding factors Ω_t are usually determined empirically. In case of birefringent crystals, a summation over light polarization must be performed and different optical properties are obtained along different crystal axes.

The integrated absorption cross section is given by:

$$\int \sigma_{\mathrm{abs}} \frac{d\lambda}{\lambda} = \frac{4\pi^2 e^2}{3\hbar c} \frac{1}{(2\mathrm{J}+1)} \left[\frac{(n^2+2)^2}{9n} S^{\mathrm{ED}} + n S^{\mathrm{MD}}\right] \tag{1.14}$$

and the transition rate for spontaneous emission is:

$$A^{\mathrm{LSJ}}_{(\mathrm{LSJ})'} = \frac{32\pi^3 e^2}{3\hbar} \cdot \frac{n^2 c}{\lambda^3 (2\mathrm{J}+1)} \left[\frac{(n^2+2)^2}{9n} S^{\mathrm{ED}} + n S^{\mathrm{MD}}\right] \tag{1.15}$$

where n is the crystal refractive index. The radiative lifetime of the initial manifold can be therefore obtained by considering all possible transition rates towards the lower manifold:

$$\frac{1}{\tau^{rad}_{\mathrm{LSJ}}} = \sum_{(\mathrm{LSJ})'} A^{\mathrm{LSJ}}_{(\mathrm{LSJ})'} \tag{1.16}$$

and the branching ratios are readily calculated as:

$$\beta^{\mathrm{LSJ}}_{(\mathrm{LSJ})'} = \frac{A^{\mathrm{LSJ}}_{(\mathrm{LSJ})'}}{\sum_{(\mathrm{LSJ})''} A^{\mathrm{LSJ}}_{(\mathrm{LSJ})''}} \tag{1.17}$$

Generally, the lowest energetic manifolds possesses the longer lifetimes due to the restriction to fewer manifolds in the summation in Eq. 1.16 and due to the λ^{-3} dependence on the transition rate in Eq. 1.15. In addition, also the $5d$ component is smaller, thereby reducing the dipole strength.

1.2.2 Multiphonon relaxation

Although the shielding of the $4f$ electrons reduces the coupling with the environment, ion - lattice interactions mediated by phonons strongly affect the emission spectrum. Actually, multiphonon relaxation is a process that competes with radiative decay and its rate is expressed as the well known "energy gap law" [18]:

$$W^{\mathrm{MP}}(T, \Delta E) = C_{\mathrm{MP}} \exp(-\alpha_{\mathrm{nr}} \Delta E) \left[\frac{1}{\exp(\hbar\omega_{\mathrm{eff}}/kT) - 1} + 1 \right]^{\Delta E/\hbar\omega_{\mathrm{eff}}} \tag{1.18}$$

where ΔE is the energy gap between the initial level and the first one below, and the effective phonon energy $\hbar\omega_{\mathrm{eff}}$ is the averaged energy of the emitted phonons. C_{MP} and α_{nr} are host-crystal related parameters estimated empirically. As α_{nr} is proportional to $(\hbar\omega_{\mathrm{eff}})^{-1}$, the multiphonon relaxation rate for a specific crystal exponentially depends on ΔE and in particulr on the number of phonons $p = \Delta E/\hbar\omega_{\mathrm{eff}}$ needed to bridge the energy gap as shown in Fig 1.2. The multiphonon relaxation can spontaneously occur or can be triggered by phonons in the thermal bath and its rate suppression by a factor of order unity is accomplished by cooling the material.

In this thesis we use single crystals, which have a well defined phonon energy spectrum corresponding to several vibrational modes. For a given ΔE, the host matrix sets the number p, which in turn determines the multiphonon rate. For example, the lifetime of the Nd^{3+} $^4I_{11/2}$ manifold, as long as 56 ms [20] in bromide matrix, is reduced by multiphonon relaxation down to $\sim$ 20 ns in YLF [21] and $\sim$ 200 ps in YAG [22] as a consequence of the different crystal phonon energies. In

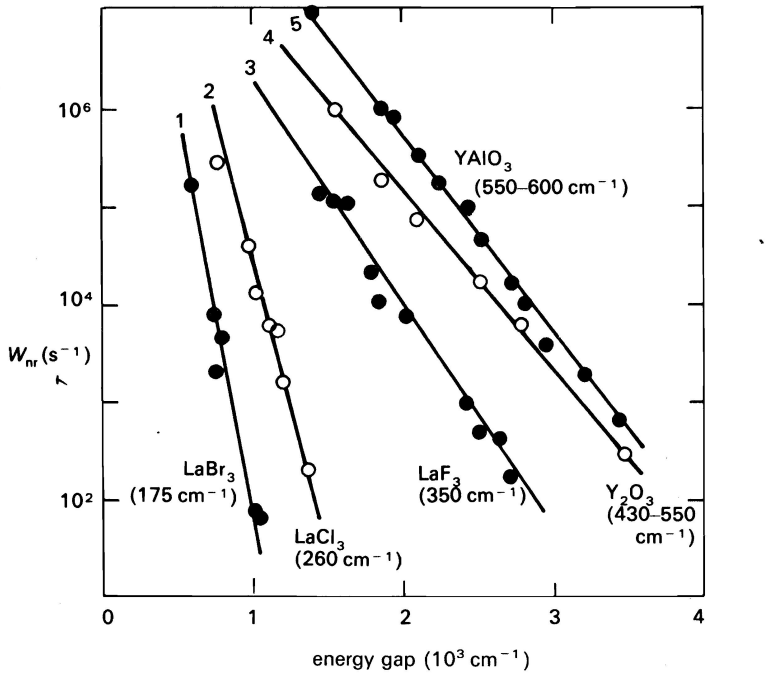

FIGURE 1.2: Multiphonon relaxation rate at low temperature as function of the energy gap between the one manifold and the next lower one for five different crystals. The figure is taken from Ref. 19.

case $p > (5-7)$ phonons are required to bridge the gap, the multiphonon rate is negligible compared the radiative one.

When the energy gap is bridged by 1-2 phonons, as is the case of the energy separation due to the Stark splitting, the process occurs in a few tens of picoseconds. As a consequence, the population of each manifold is distributed among its levels according to the Boltzmann distribution in less than a few nanoseconds. For $\Delta E < 1\,\text{meV}$, the number of available vibrational modes is small and this phonon bottleneck causes the suppression of multiphonon relaxation. This is the case for the Zeeman splitting energy and the spin lattice relaxation between Zeeman levels is well approximated by the formula [23]:

$$R(B,T) = \alpha_D g^3 B^5 \coth\left(\frac{\bar{g}\mu_B B}{2kT}\right) + \alpha_R T^9 + \alpha_O \left(\frac{1}{e^{\Delta/kT}-1}\right) \tag{1.19}$$

The first term accounts for direct relaxation. The strong dependence on the $\bar{g}$-factor and the magnetic field is due to the phonon bottleneck at low energy. The second term is relative to the inelastic scattering Raman process in which the excited ion energy is transferred to two interacting phonons. The third term represents the Orbach process, whereby the excited ion absorbs a phonon of energy

Δ that is resonant with a Stark level. Subsequently the ion relaxes to the ground state by emitting a more energetic phonon. The constants α_D, α_R, and α_O account for the strength of the respective processes. As the Orbach and the Raman process rely on the phonons of the thermal bath, their rate has a strong dependence on the temperature. At liquid helium temperature, the last two terms are in general negligible compared to the first and lifetimes of several milliseconds are observed.

For smaller energy gaps, as those between hyperfine levels of the ground state, lifetimes as long as several days have been reported [24].

1.2.3 Energy transfer processes

The last process we consider is the energy transfer. One excited ion can transfer its energy or a fraction of it to a nearby ion that typically lies in the ground state. This process can be very efficient in RE-doped materials due to the high number of ions levels and to their long lifetimes. According to the Fermi Golden Rule, the energy transfer rate can be written as [18, 25]:

$$W^{\mathrm{AD}} = \frac{2\pi}{\hbar} |\left\langle \Psi_f^{\mathrm{A}} \Psi_f^{\mathrm{D}} \right| H_{\mathrm{int}} \left| \Psi_i^{\mathrm{A}} \Psi_i^{\mathrm{D}} \right\rangle|^2 \int S_a^{\mathrm{A}} S_e^{\mathrm{D}} \, \mathrm{d}E.$$

The squared modulus of the matrix element represents the electromagnetic interaction between the initial (i) and the final (f) states of the donor (D) and acceptor (A) ions. The integral accounts for the overlap of the emission spectrum of the donor and the absorption spectrum of the acceptor. As the electric dipole-dipole (d-d) transition is forbidden, the quadrupole-dipole (q-d) and quadrupole-quadrupole (q-q) must be included in the Hamiltonian H_{int} as well. The energy transfer rate is therefore expected to depend on the average distance R of the randomly distributed ions as:

$$W^{AD}(R) \approx \frac{a^{\mathrm{d-d}}}{R^6} + \frac{a^{\mathrm{d-q}}}{R^8} + \frac{a^{\mathrm{q-q}}}{R^{10}} \tag{1.20}$$

A good estimation of the coefficients $a^{\mathrm{d-d}}$, $a^{\mathrm{d-q}}$, $a^{\mathrm{q-q}}$ can be experimentally obtained by measuring the corresponding level lifetime for different dopant concentration in a given host crystal. Note that the radiative lifetime and the multiphonon relaxation are independent on the doping level.

If the transitions of the two ions are resonant, the energy transfer is very efficient. However, it can take place even in the presence of a slight energy mismatch owing the absorption or emission of phonons. Likewise to the multiphonon relaxation rate, a temperature and energy mismatch ΔE_m dependence can be obtained for

the energy transfer process [18, 25]:

$$W^{\mathrm{AD}}(T,\Delta E) = C^{\mathrm{AD}} e^{-\beta_{\mathrm{AD}}\Delta E_m}\left[\frac{1}{\exp(\hbar\omega_{\mathrm{eff}}/kT)-1}+1\right]^{\Delta E/\hbar\omega_{\mathrm{eff}}} \tag{1.21}$$

where the β_{AD} parameter depends on the effective phonon energy of the crystal.

This energy transfer process is exploited to populate a specific Tm:$LiLuF_4$ level that cannot be directly excited by our tunable lasers. The details are reported in Appendix.

1.3 Transition linewidths

We have described the energy level structure and the main relaxation processes of the RE-doped crystals. Here we focus on one of their properties whose exploitation is the basis of this work: the narrow optical transition linewidths.

The transition linewidths of a system of atoms (or molecules) are in general determined by two classes of broadening mechanisms. The "homogeneous broadening" affects the spectral width of all single atoms, i.e. the homogeneous linewidth. On the contrary, the "inhomogeneous broadening" alters the energy levels of each atoms in a different way and the spread of transition frequencies is denoted as inhomogeneous linewidths.

1.3.1 Homogeneous broadening

As for any quantum systems, the Heisenberg uncertainty principle relates conjugate variables such as time and energy. In particular, the uncertainty of the atomic transition energy, i.e. the homogeneous linewidth Γ_{hom}, is connected to the coherence time T_2 defined as the time during which a single atom keeps its state unperturbed both in terms of energy level and transition dipole phase:

$$\Gamma_h = \frac{1}{\pi T_2} = \frac{1}{2\pi T_1} + \frac{1}{\pi T_\phi} \tag{1.22}$$

Here, the two contributions to the coherence time are expressed through the level lifetime T_1 and the pure dipole dephasing time T_ϕ. It must be noted that T_1 is generally shorter than the manifold lifetime τ (Eq. 1.11) as it accounts also for the processes that lead to a change of the ion energy level of the manifold. By the way, T_1 represents the upper limit for the coherence time and the long level lifetime of RE ions potentially gives homogeneous linewidths of the order of some kHz or Hz. However, the homogeneous linewidth are usually much broader. For example,

the two phonons Raman process at high temperature determines linewidths as large as a few THz. Its rate scales with the seventh power of the temperature and its contribution to the homogeneous linewidth is negligible at temperatures lower than few kelvin degrees. By so doing, also the contribution due to resonant absorption of phonons is suppressed.

Another decoherence process that we take into account is the electronic spin flip in Kramers ions which includes both the spin lattice relaxation and the spin flip-flop, namely the spin exchange between two ions. The Kramers levels are at least doubly degenerate and the spin flip rate is generally high due to the resonant nature of the process. However, when an external magnetic field is applied, the degeneracy is removed and the spin flip rate dependence on the magnetic field intensity and temperature is given by [23]:

$$R_{sp} = R(B,T) + \alpha_{ff}\frac{n_p^2\bar{g}^4}{\Gamma_{ihn}}\mathrm{sech}^2\left(\frac{\bar{g}\mu_B B}{2kT}\right) \tag{1.23}$$

$R(B,T)$ and the second term are the spin lattice relaxation (Eq. 1.19) and the spin flip-flop rate respectively. α_{ff} is a constant, n_p the concentration of ions with factor $\bar{g}$ and Γ_{ihn} is the inhomogeneously broadened paramagnetic resonance absorption linewidth. The electronic spin flip-flop involves only resonant anti-parallel spin and it is inhibited by intense magnetic field and low temperature which promotes the spin alignment. We must also consider that the higher the term $(\bar{g}\mu_B B)/(2kT)$, the more depleted is the population of the upper Zeeman level so that also the overall electronic spin flip is suppressed.

We draw the conclution that concentrations in a level of few tens of parts per million, temperature lower than 2 K and magnetic field of several Tesla are the best conditions to obtain longer coherence time. The ultimate limit is set by the interaction between the RE ion electronic magnetic moment and the nuclear magnetic moment of nearby atoms. Hence, the narrowest homogeneous linewidth is obtain in a host matrix composed by elements with zero or low nuclear magnetic moment.

1.3.2 Inhomogeneous broadening

In homogenenous broadening processes the atoms are still identical to each other and all mechanisms which, by contrast, destroy the atoms equality are included into inhomogenenous broading processes. In gases, the collisions broaden the spectral width of each atom but it is the different atomic velocity that change the transition frequency. In a solid, this frequency spread is much larger because identical environments for each atom are impossible to accomplish due to the unavoidable presence of defects. Actually, disordered crystalline and amorphous

materials are characterized by large transition linewidths ($\sim$ THz) whereas the narrowest inhomogeneous linewidths are achieved in single crystals that can be grown with very high optical quality, such as $YLiF_4$ crystals.

The doping level is another broadening factor as the dopant has never the same size of the substituted ion. Crystal strains due to their markedly different atomic radius cause inhomogeneous line broadening and in some cases, limit the maximum affordable concentration to a few percents. In addition, the higher is the concentration, the higher is the chance for two or more dopant ions to be sufficiently close to alter the crystal field hamiltonian term and, hence, their energy levels. If the distance is small enough, RE ions can also form pairs which produce satellite lines in the absorption spectrum. A similar feature arises in crystals with high density point defect, such as vacancies or impurities. The RE ions in equivalent positions with respect to the defect experience the identical perturbation and collectively contribute to the emission or absorption intensity at a specific frequency.

For very low doped- excellent grade crystals, other broadening mechanisms can be appreciated. In particular, the natural abundance of different isotope are responsible for dopant inhomogeneous linewidths of the order of 1 GHz, which are reduced down to 100-10 MHz in isotopically pure crystals. In this case the remaining broadening is set by inevitable crystal strains/impurities and by the magnetic interaction between the dopant and the nuclear spin distribution of the neighboring atoms.

1.3.3 The effective linewidth

The effective linewidth is a term introduced in photon echo experiments to take into account the spectral diffusion effect, namely the random variation of the ion transition frequency resulting from the interaction with the dynamic environment.

The transition frequency of each ion is related to the respective magnetic moment orientation of the surrounding atoms through the magnetic dipole-dipole interaction. Electronic spin flips randomly shift the initial common transition frequency of each ion. As a consequence, the initial linewidth Γ_0 of a RE ions system excited by a narrow laser is broadened by the spin flips occurrence. This effective linewidth is well described at low temperature by the expression [23]:

$$\Gamma_{\mathit{eff}}(t) = \Gamma_0 + 0.5 \left[\Gamma_{max}\,\mathrm{sech}^2\left(\frac{\bar{g}_p \mu_B B}{2kT}\right)\right] [1 - e^{-\bar{R}t}] \tag{1.24}$$

Its time evolution is then set by the perturbing spin flip rate (upward and downward) $\bar{R}$ of the ions characterized by the effective g-factor $\bar{g}_p$ and density n_p. Γ_{max} is the maximum frequency dispersion determined by the randomly distribution of

the dipoles. It can be expressed as [23, 26]:

$$\Gamma_{max} = \frac{\pi}{9\sqrt{3}} \frac{\mu_0 \mu_B^2 |\bar{g}_g - \bar{g}_e| \bar{g}_p n_p}{h} \tag{1.25}$$

The variation on the optical center frequency depends on the fluctuation of the local magnetic field amplitude, proportional to the strength $\bar{g}_p$ of the perturbing atom, through the difference between the effective g-factor of the initial (e) and final (g) levels. The effect is more pronounced if the density of the perturbing dipole is high. Accordingly to Eq. 1.24, the long time limit of the effective linewidth is smaller than Γ_{max}. Actually, the stronger the magnetic field and the lower the temperature, the larger the fraction of the dipole moments that are aligned and does not participate to the perturbation.

To some extent, even the excitation and the de-excitation of ions affect the local field of the nearby optical center [27], especially for heavy RE ions concentrations. Also nuclear spin orientation participate to define the optical center transition frequency. However, the nuclear spin flip rate is reduced near the RE ion because the presence of its magnetic moment alters the hyperfine energy levels of the neighboring atoms. The lack of resonance inhibits the spin flip-flop rate generating the so-called "frozen-core" around the RE ions and so reduces the perturbation on the optical center. Thus, the main contribution to the effective linewidth of the RE ions is usually due to the spin flip of the same RE ions even at very low concentration [23].

1.3.4 Other broadening mechanisms

Lanthanides with the exception of Pr, Tb, Ho and Tm, possess more than one isotope with relevant natural abundance. Due to the different atomic mass, isotopes of the same chemical species have energy levels that differ in the (100 MHz-1 GHz) range.

In many cases, the transitions of different isotopes as well as those that involves different hyperfine and super-hyperfine levels are not resolved in the optical spectrum giving rise to a single broad line. Such effects cannot be considered either homogeneous or inhomogeneous.

1.4 The Er^{3+} doped YLF and YSO samples

The experimental investigations of this thesis are based on trivalent Erbium doped $YLiF_4$ (YLF) and Y_2SiO_5 (YSO) crystals. After the previous general discussion,

TABLE 1.1: Naturally abundance and nuclear properties of some isotopes.

Element	**Atomic number** [A]	**Abundance** [%]	**Nuclear spin** [I]	**Magnetic moment** [μ_I/μ_N]
Lithium	6	7.6	1	0.822
	7	92.4	3/2	3.25
Oxygen	16	99.8	0	0
	17	0.04	5/2	-1.89
	18	0.21	0	0
Fluorine	19	100	1/2	2.63
Aluminum	27	100	5/2	3.64
Silicon	28	92.2	0	0
	29	4.68	1/2	-0.555
	30	3.09	0	0
Yttrium	89	100	1/2	-0.137
Erbium	162	0.14	0	0
	164	1.61	0	0
	166	33.6	0	0
	167	22.9	7/2	-0.567
	168	26.8	0	0
	170	14.9	0	0
Thulium	169	100	1/2	-0.232

we are able to deepen the Er^{3+} ions properties in terms of energy levels, relaxation processes and characteristic linewidths.

1.4.1 Crystals structure

As shown in Tab. 1.1, Er has 6 stable isotope, 4 of which have an abundance larger than 10% and the only isotope with non-zero nuclear spin is ^{167}Er with $I = 7/2$. In its trivalent form, Er^{3+} is a Kramers ion that has 11 electrons in the $4f$ shell, 3 of them unpaired. When it is embedded in YLF and YSO crystals, whose structure are described in Tab. 1.2 and shown in Fig. 1.3 and 1.4, Er^{3+} ion substitute Y^{3+} host ion. The strain is quite moderate due to the small difference in atomic radius. Y^{3+} in YSO occupy two crystallographic inequivalent sites that bestow to the dopant Er^{3+} ions slightly different characteristics in terms of energy levels position, levels lifetime, transition linewidth and coherence time. For the purposes of this thesis we will focus only on the site 1 and on the spectroscopic properties of the first excited manifolds.

TABLE 1.2: Crystal structure properties of YSO and YLF crystals.

Formula	**Lattice parameter** Å	**Structure**	**Space Group**	**Density** [g/cm^3]
$YLiF_4$	$a = b = 5.16,\ c = 10.85$	Tetragonal	I41/a	3.99
Y_2SiO_5	$a = 10.41, b = 6.72, c = 12.49$	Monoclinic	$C_{6,2h}$	4.44

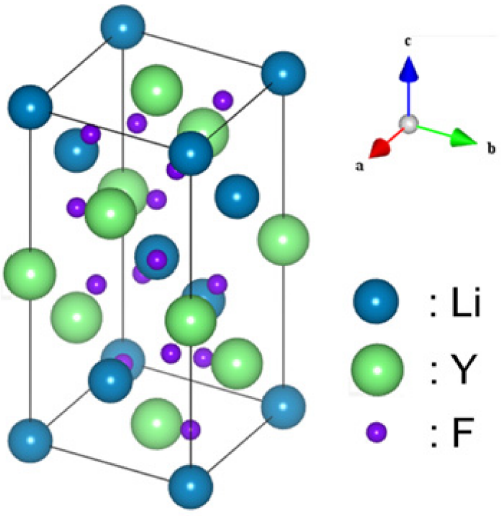

FIGURE 1.3: Schematic representation of the YLF_4 crystal structure. The figure is taken from Ref. 28.

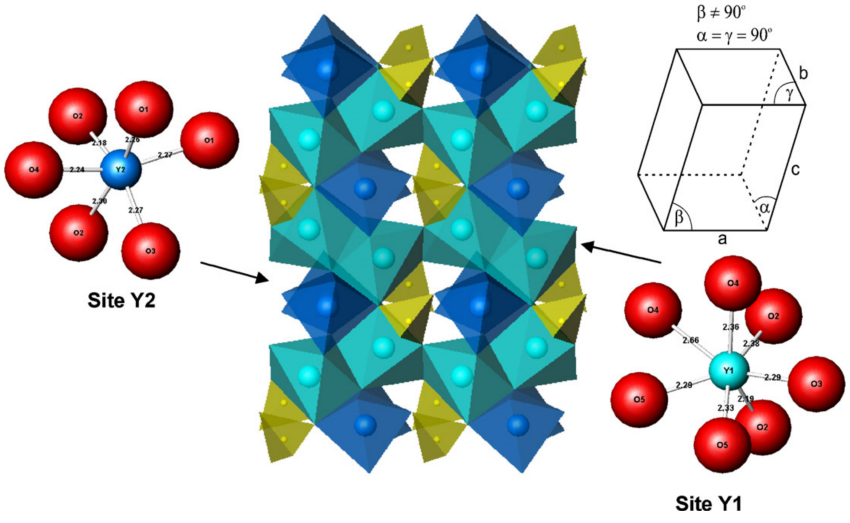

FIGURE 1.4: Schematic representation of the Y_2SiO_5 crystal structure. The silicon atoms are yellow, the yttrium atoms in site 1 are light blue and those in site 2 are blue. The oxygen atoms are at each node. The figure is taken from Ref. 29.

1.4.2 Crystals growth

The main experimental results of this work regards the spectroscopic features of three Er^{3+} doped single crystals.

The Er:YSO at 0.1% sample ($4 \times 5 \times 6.2\,mm^3$) was provided by Scientific Materials Corp (Bozeman, Montana). The axis orientation with respect of the sample surfaces is unknown.

The Er:YLF doped at 0.01% ($5\times5\times5\,mm^3$) and 1% ($5\times5\times5.1\,mm^3$) single crystals were grown with the Czochralski method by the group of University of Pisa. High purity 5N (99.999%) starting raw materials (LiF, YF_3 and ErF_3 powders) were used and the growth was carried out at the temperature of 880 °C, in an inert atmosphere of pure (5N) argon, with a pulling rate of 0.5 mm/h. A seed of an undoped YLF monocrystal oriented along the c axis was used for the growth.

1.4.3 Crystals properties

A partial energy level scheme of Er:YLF is shown in Fig. 1.5 as a reference. The contribution of the main hamiltonian term to the level splittings are also displayed. In particular, the Stark splitting of ground manifold $^4I_{15/2}$ which consist of 8 energy levels and the $^{167}Er^{3+}$ hyperfine splitting of the lowest level are shown.

Er:YLF and Er:YSO have maximum phonon energy of $440\,cm^{-1}$ and $1000\,cm^{-1}$, respectively [32, 33]. The multiphonon relaxation is therefore much more favoured in the latter crystal than in the former. For example, the effective lifetime at cryogenic temperature of the $^4I_{11/2}$ manifold is several milliseconds for Er:YLF [34] but it is reduced down to 18 μs for Er:YSO [35] due to multiphonon relaxation. The energy gap between $^4I_{13/2}$ and $^4I_{15/2}$ manifold is large enough for both crystals to show radiative lifetime longer than 10 ms which can provide long coherence time. Actually, Er-doped crystal are the most studied materials in the framework of the quantum information studies and several works regarding its coherence time have been published (Tab. 1.3). In this regard, YSO crystal is of interest for the low nuclear magnetic moment of its elements. With reference to the Tab. 1.1, most of Oxygen and Silicon atoms have nuclear spin 0 thereby reducing the overall rate of nuclear spin flips. The longest optical coherence time among solid-state systems with the impressive values of 4.4 ms [36] was indeed observed in Er:YSO for the $^4I_{13/2} \rightarrow {}^4I_{15/2}$ transition. This result was accomplished by polarizing the electronic spin bath with a magnetic field of 7 T and cooling the crystal down to 1.6 K.

Similar studies were performed for "almost undoped" YLF crystals at 0.2 K and under 250 mT, dephasing time as long as 300 μs was measured. However, when

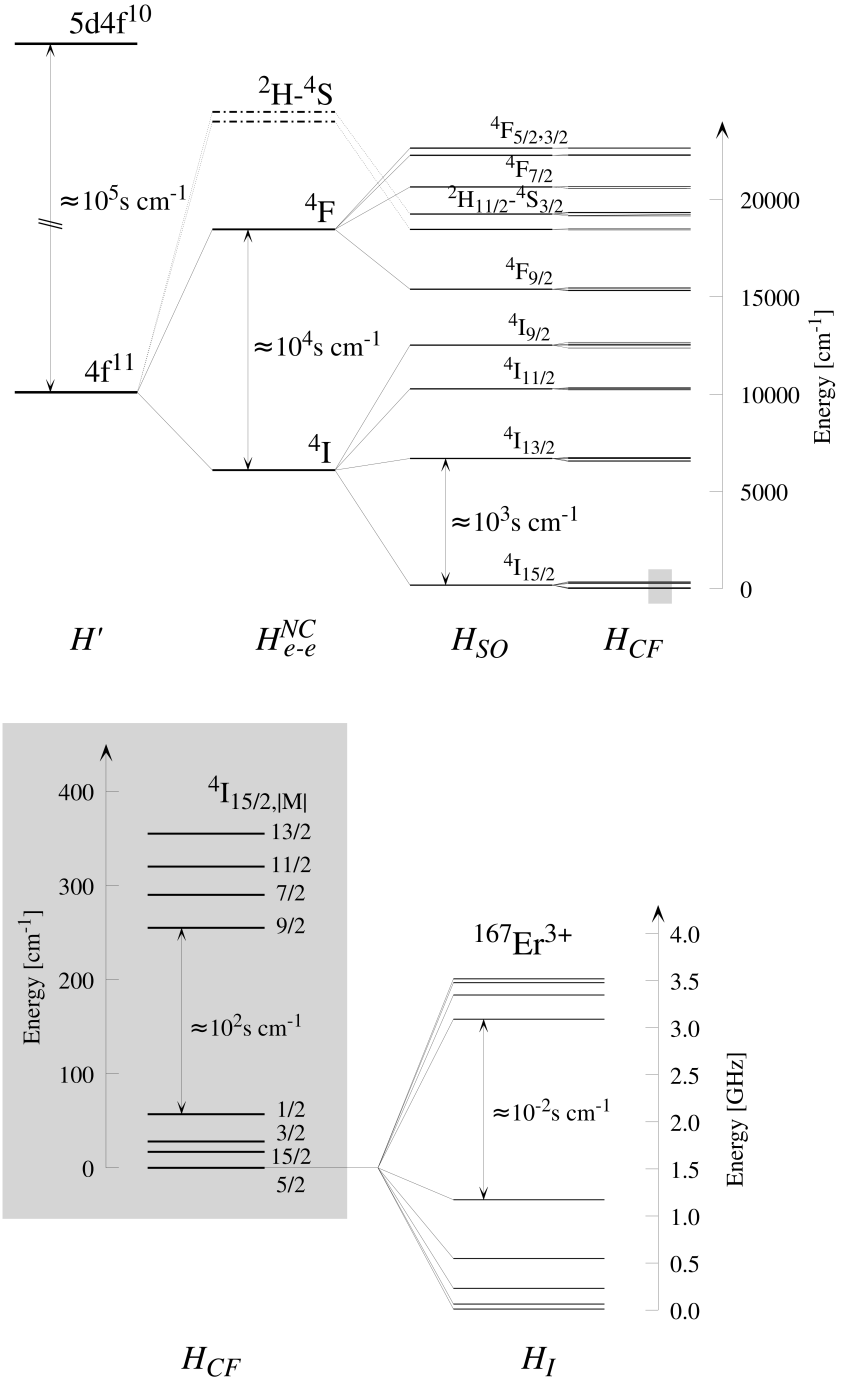

FIGURE 1.5: Energy level structure of Er:YLF as calculated and experimentally measured [30, 31]. The order of the energy splitting caused by the main interactions are also represented.

TABLE 1.3: Spectroscopic parameters of the $^4I_{13/2}(1) \rightarrow {}^4I_{15/2}(1)$ transition of trivalent Erbium ions for different matrices, concentrations, temperature and applied magnetic field strength. For the YSO crystal, the values are referred to the site 1.

Dopant	**Host**	Γ_{ihn} [GHz]	Γ_{hom} [kHz]	**B**, **T**	T_2 [μs]	Ref
^{167}Er 0.005%	Y ^{7}LiF$_4$	0.024	177	0 T, 4 K	1.8	[40]
^{166}Er 0.001%	Y ^{7}LiF$_4$	0.016	>320	0.25 T, 1.5 K	<1	[37]
			11	0.04 T, 0.2 K	30	[37]
			1	0.25 T, 0.2 K	300	[37]
^{166}Er 0.005%	Y ^{7}LiF$_4$	0.016	6.4	0.25 T, 0.2 K	50	[37]
^{167}Er 0.005%	Y_2SiO_5	0.2	11	0.3 T,1 K	28	[41]
^{167}Er 0.005%	Y_2SiO_5	0.2	1.5	0.3 T,12 mK	217	[41]
Er 0.2%	$YLiF_4$	0.45		0T,5 K		[42]
Er 0.02%	$(Eu_{0.02}Y_{0.98})_2SiO_5$	22	3.7	3 T,5 K	86	[43]
Er 0.02%	Y_2SiO_5	0.51	3.2	3 T,1.6 K	100	[23]
Er 0.005%	Y_2SiO_5	0.34	1.9	3 T,1.6 K	167	[38]
Er 0.001%	Y_2SiO_5	0.18	0.8	3 T,1.6 K	400	[38]
Er 0.0015%	Y_2SiO_5	0.18	0.073	7 T	4380	[36]
Er 0.005%	$LiNbO_3$	180	3.7	0.5 T	86	[44]
Er 0.1%	$Y_3Al_5O_{12}$	30	5.5	4 T	58	[44]

the temperature was increased to 1.5 K, the electronic spin flip rate reduced the coherence time down to less than 1 μs [37].

Even when the Er concentration is as low as few parts per 10^5, it plays a significant role due to the Er-Er magnetic dipole interaction. Homogeneous linewidths of 0.8 kHz, 1.9 kHz and 3.2 kHz has been observed at the same experimental condition in Er:YSO doped at 0.001%, 0.005%, 0.02%, respectively. Also the inhomogeneous component increased from 180 MHz to 510 MHz as results of the mutual environment disturbance [23, 36, 38]. The narrowest inhomogeneous linewidth have been found for YLF crystals decreasing from 120 MHz to 16 MHz when the Li atoms was isotopically purified. The superhyperfine interaction with nuclear spin of fluorine atoms was responsible of this limit [37].

The above discussion concerns the transition between the lowest Stark level of the involved manifold. That between another combination of manifold levels are of low interest. Actually, the lifetime of the other levels is much shorter due to the multiphonon relaxation rate and this results in a homogeneous linewidth much broader than that inhomogeneous one. For example, the absorption transitions linewidth at 5 K from the ground state of Er:YLF 0.2% ranges from 450 MHz for the lowest level to 200 GHz for the highest one of the $^4I_{13/2}$ manifold [39].

Chapter 2

Axion Dark Matter detection using Rare earth doped crystals

The indications from cosmological observation that the μeV domain is a favored energy range for the mass of QCD axion gives rise to an increasing interest in designs of weakly interacting, low energy particle detector. To this purpose, Prof. P. Sikivie proposed a novel detection scheme in his paper "Axion Dark Matter detection using atomic transition" published on *Physic Review Letter* in 2014 [1]. The RE-doped crystals could be a suitable axion target for the Sikivie's scheme under several aspects, and in this chapter we present our preliminary studies to investigate the experimental implementation of a such detector using Er:YSO and Er:YLF crystals.

After a brief introduction about Axion properties and the Sikivie scheme for axion detection, we address the basic requirements for such detector using RE-doped crystals as target deepening its feasibility and its efficiency. The working condition such as temperature and the required crystal volume and concentration in order to obtain a good signal-to-noise ratio, are also estimated. A special section is devoted to deal with the possible noise sources that the use of lasers implies. In the last section we draw the conclusion on the detector realization.

2.1 Main axion properties

Here we propose a brief summary of the axion properties and the prospects in its detection that have strongly motivated the scientific community in its research. A detailed review can be found here [45].

QCD Axion is a hypothetical elementary particle which arises from a simple extension of the Standard Model. It was introduced by Peccei and Quinn [46] in

order to explain the strong CP problem, namely the preservation of the Charge-conjugation Parity symmetry in the strong interaction observed in all experiment performed so far. Actually, there is no reason for quantum chromodynamics to prevent the occurrence of CP violation.

The nature of Dark Matter is another long standing problem in particle physics and the axion truly represents one of the most attractive solution, especially after that the lack of detection has excluded heavy mass particle [47, 48]. Several models have been developed to predict the axion physical properties and can be grouped in KSVZ [49] or DFSZ [50, 51] classes on the basis of zero or full coupling with leptons, respectively. A common statement anyway holds for the axion mass m_a, that has been firmly expressed by two independent calculations [52, 53] as:

$$m_a \simeq 57 \left(\frac{10^{11}\, GeV}{f_a} \right) \mu eV$$

The axion mass is inversely proportional to the axion decay constant f_a parameter, which reflects the weakness of the couplings between the axion field a and the standard model particles.

The existence of QCD axion and its relative couplings with fermions and photons lead to additional processes that should influence astrophysical observations. For example, the production of axions during the supernova SN1987A burst should have reduced its duration. The comparison of the measured electron antineutrinos flux generated during the event with the theoretical expectation, allows the particle physicists to exclude QDC axion mass heavier than $\mathcal{O}(1\,\mathrm{meV})$. The $1\,\mu\mathrm{eV} < m_a < 10\,\mathrm{meV}$ is the commonly accepted and favored mass range by cosmological and astrophysical bounds [54], as it is also showed by Fig. 2.1.

Besides the axion low energy mass, its density as dominant component of Dark Matter should be large. The presence of the Dark Matter is confirmed by its gravitational effect on the light propagation and on the normal visible matter. In particular, it has been estimated from kinetic data of the galaxy rotational curves that Dark Matter density is equal to $\rho_a \sim 0.42\,\mathrm{GeV/cm^3}$ [56]. If we assume that Dark Matter is entirely composed of axion with mass $m_a = 100\,\mu\mathrm{eV}$, the axion particle density is $\rho_a/m_a = (0.4\,\mathrm{GeVcm^{-3}})/(100\,\mu\mathrm{eV}) = 4 \cdot 10^{12}\,\mathrm{axion/cm^3}$. These particles should behave as cold matter, i.e. they are not relativistic particles and have almost no velocity dispersion. Earth is moving with respect to the galaxy centre at the velocity of v_e =300 km/h and then it should be passing through the cold Dark Matter density with the same velocity, experiencing a large fluence of axions, the so called *axion wind*. In the earth rest frame, the relative De-Broglie wavelength for an axion of mass $m_a = 100\,\mu\mathrm{eV}$ and velocity $v_a = v_e$ is $\lambda_{dB} = 2\pi/(m_a v_a) = 12.4\,\mathrm{m}$. Axion can thus be approximated to a monochromatic classical oscillating field whose coherence achieves length in the order of meters and coherence time $t_a = hc^2/m_a\bar{v}^2 = 28\,\mu\mathrm{s}(100\,\mu\mathrm{eV}/m_a)$ [45].

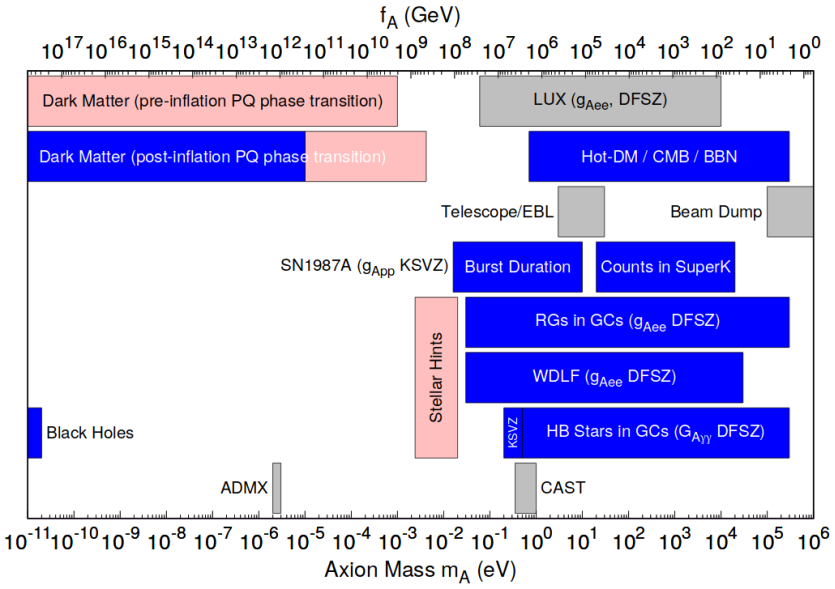

FIGURE 2.1: The allowed axion mass range, bounded by existing experimental exclusion bands (gray area) and by cosmological and astrophysical consideration (blue area). Pink area indicates the favoured energy range. See Ref. 45, 55 for further details. The figure is taken from Ref. 55.

The low energy and the weak interaction of this axion galaxy halo requires unconventional detectors which also must cover a large range of energy. The most interesting experiment concerns the axion to photon conversion through inverse Primakoff effect in a microwave cavity and under a strong magnetic field. The ongoing ADMX is the first experiment of its kind with sufficient sensitivity to probe the axion predicted by models. At this moment, the experiment has excluded the energy range $1.9\,\mu\text{eV} < m_a < 3.69\,\mu\text{eV}$ to some degree [57] and energy up to $100\,\mu\text{eV}$ can be potentially investigated. However, for higher energy the sensitivity of this approach drops.

To overcome this problem, a new detector scheme was again proposed by Sikivie [1].

2.2 The Sikivie's scheme

The interaction between axions and a general fermion can be approximated by the Lagrangian:

$$\mathcal{L}_{af} = -\frac{g_f}{2f_a}\partial_\mu a \bar{f}(x)\gamma^\mu\gamma_5 f(x)$$

where a and f are the axion and the fermion fields respectively. The constant g_f accounts for the their coupling strength. Assuming the non-relativistic nature of the axion particle, the interaction energy can be expressed as function of the

fermion mass m_f, momentum p_f and spin $\vec{S_f}$ as:

$$H_{af} = \frac{g_f}{2f_a}\left(\vec{\nabla}a \cdot 2\mathbf{S}_f + \partial_t a \frac{\mathbf{p}\cdot 2\mathbf{S}_f}{m_f}\right) \tag{2.1}$$

The first terms in the parenthesis can induce transition of M1 type whereas the second is not useful for the detection because it should require axion energy higher than eV. For an atom target, axions can interact with both nucleus and electrons and Eq. 2.1 becomes:

$$H_{ae} = \frac{g_e}{f_a}\vec{\nabla}a \cdot \mathbf{S} \qquad H_{aN} = \frac{g_N}{f_a}\vec{\nabla}a \cdot \mathbf{I} \tag{2.2}$$

Due to the different fermions mass, the coupling with the electron g_e is 3 magnitude order weaker than the coupling with the nucleus g_N which should be ~ 1. If the energy separation between the atom level $|0\rangle$ and $|1\rangle$ is resonant with the axion mass, then the atom transition can be driven by the absorption of the axion and the process rate considering the axion fluence of the axion wind is given by:

$$R_i = \frac{2}{m_a f_a^2} \cdot min(t, T_2, t_a) \cdot \int d^3\mathrm{p_a} \frac{d^3 n_a}{d\mathrm{p_a}^3} |\, \langle 0|(g_e\mathbf{S} + g_N\mathbf{I}) \cdot \mathbf{p_a}|1\rangle\, |^2 \tag{2.3}$$

The minimum among the measurement integration time t, the lifetime of the excited state of the atom T_2 and the characteristic time of the axion t_a is introduced to take in account the overlap between the target bandwidth $B_t = [min(t, T_2)]^{-1}$ and the frequency spread of the axion $B_a = t_a^{-1}$. We can define an "effective" axion-electron coupling $\widetilde{g}$ in the following way:

$$\widetilde{g}^2 \overline{v^2} m_a \rho_a \equiv \int d^3\mathrm{p_a} \frac{d^3 n_a}{d\mathrm{p_a}^3} |\, \langle 0|g_e\mathbf{S} \cdot \mathbf{p_a}|1\rangle\, |^2 \tag{2.4}$$

$\widetilde{g}$ can be taken as unitary but it depends on the atom polarization and the axion momentum distribution. The number of events per mole of interacting atoms N_A is given by:

$$\frac{\#events}{mole} = tN_A R_i \frac{min(t, T_2)}{min(t, T_2, t_a)} \tag{2.5}$$

In this way, if the bandwidth of the axion signal is narrower then the atom bandwidth ($B_a < B_t$), then the number of events is simply $N_a R_i$. If $B_a > B_t$, the atoms can only interact with the fraction of the axions that matches the atom transition frequency. In this thesis the condition $B_a < B_t$ is satisfied and by substituting Eq. 2.4 in Eq. 2.3 the event rate for a mole of atoms is given by:

$$N_a R_i = 9.3 \cdot 10^{-2} \cdot \widetilde{g}^2 \cdot \left(\frac{\overline{v^2}}{10^{-6}\, c}\right) \cdot \left(\frac{min(t, T_2, t_a)}{10^{-6}\, s}\right) \cdot \left(\frac{100\, \mu eV}{m_a}\right)^2 \cdot \left(\frac{\rho_a}{0.4\, GeV/cm^3}\right) \tag{2.6}$$

If we arbitrarily choose $m_a = 100\,\mu$eV, one event every 10 second per mole is estimated.

By choosing atoms with a degenerate ground state, it is possible to split the levels via Zeeman effect, and by taking a Landé factor $g = 1$ an energy range up to $2\Delta E = 2g\mu_B B = 280\,\text{GHz}= 1.1\,\text{meV}$ can be probed with the haloscopes axion mass using a variable static magnetic field with a reasonable maximum intensity of 10 T. With this method we should be able to obtain also a fine estimation of the axion mass, the relative constant f_a and the coupling factor.

Unfortunately, there are not detectors that can clearly identify a single spin flip in a macroscopic active material. The solution proposed by Sikivie is to use a continuous narrow laser tuned between the upper Zeeman level of the ground state and a higher energetic level. By so doing, when the axion is absorbed by the atom, the latter can be further excited by laser photons absorption and the subsequent fluorescence in the visible/near infrared range can be efficiently detected using photomultiplier tubes or Silicon photomultipliers. A simple representation of the detector scheme is displayed in Fig. 2.2. Note that the laser intensity can be filter out from the fluorescence by using bandpass filters.

A first requirement is that the upper Zeeman level is not thermally populated otherwise a background of spurious fluorescence would strongly affect the axion detection. This constrain implies a working temperature of tens of mK while a strong laser field is applied to the cooled active material. Assessments of the heating effects due to the laser radiation are also mandatory for the realization of the detector.

The laser upconversion idea could be eventually applied successfully to the hyperfine levels as well. However, due to the smaller energy level separation, the required working temperature is in the μK range, which cannot be experimentally obtained with macroscopic target. For this reason, electronic levels are the only suitable ones.

2.2.1 The RE as target

Rare earth ions are promising target atoms for several reasons. The Sikivie's scheme requires that the Zeeman splitting is well resolved for optical transitions. If this is not the case, the laser tuned between the upper Zeeman level and the higher energy level would be absorbed also by the ions lying in the lower one resulting in a strong background noise. Thanks to their feeble coupling with the environment, RE ions-doped crystals offer the narrowest transition linewidths in solid-state systems and their rich level scheme provides several possible upconversion-emission

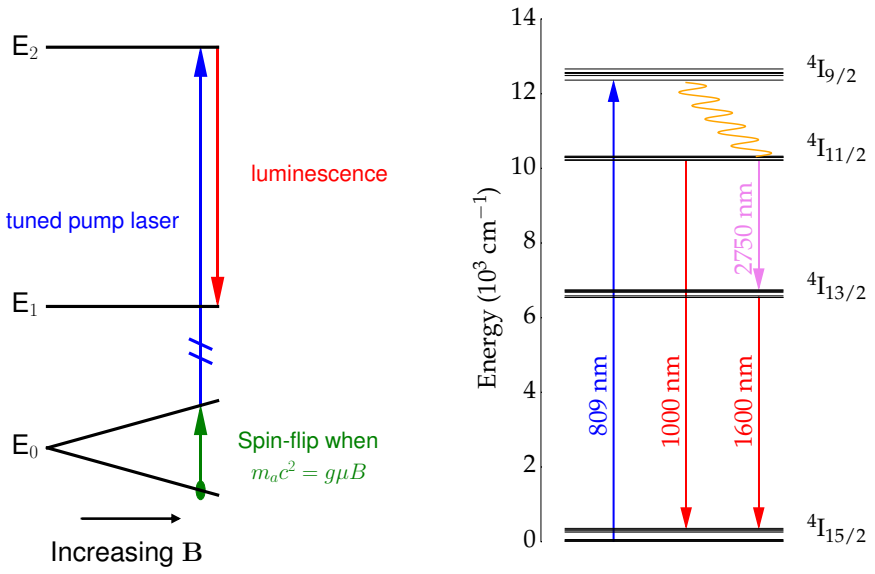

FIGURE 2.2: (Left) Axion detection scheme as proposed by Sikivie. (Right) Implementation of the scheme to the Erbium ions doped fluoride crystals. The transition driven by axion interaction is drawn in green and by laser fluence in blue. The red arrow indicates the spontaneous fluorescence that could be used as signal and the wavy orange line represents the non radiative transition.

scheme. Furthermore, RE elements possess up to seven unpaired electrons allowing large total electronic spin momenta. Nuclear spins are also high. Hence an higher transition rate per atom is attained.

In particular, we have chosen trivalent Er ions crystals which have three unpaired electrons in the ground state and 23% of the atom has $I = 7/2$. Erbium is the most promising ion among RE for quantum information and therefore it is subject of several work at cryogenic temperature which we may compare with.

2.3 Experimental apparatus

The optical measurements on the RE ions presented in this thesis are carried out between 1.6 and 4.2 K by employing tunable lasers as excitation sources. The experimental setup allows us to measure the crystal spectral absorption and to investigate at the same time different properties of the luminescence such as spectral intensity, temporal profile and spatial propagation.

2.3.1 Liquid Helium cryostat

A picture of the cryostat used to cool sample is shown in Fig. 2.3. We pump the helium gas out the 20 l chamber to reduce the pressure down to few mBar. In this way, the liquid Helium can be cooled from 4.2 K to 1.6 K, becoming a superfluid below the lambda point at 2.18 K.

A multisensor is set inside the chamber and allows for the absolute pressure, the temperature and the Helium flow measurements. Two ongoing days of measurements at 1.6 K are guaranteed in a run by a single Helium filling.

The sample cell has three optical quartz windows sealed with indium to isolate the liquid Helium from the vacuum shroud. As many quartz windows aligned to the others and mounted on the outer container allow the transmission of light from UV to mid-infrared. A simplified scheme of the apparatus is drawn in Fig. 2.4.

The crystal sample is put in a plastic or aluminum holder which is mounted on a long rod. Once the latter is inserted inside the helium chamber, the sample is brought down to the windows level and the upper rod edge can be used to seal the cryostat entrance.

A magnetic field of 370 mT can be applied to the cooled crystal by two parallel permanent NdFeB magnets.

2.3.2 Laser sources

The most investigated transition in Er^{3+} ion is the one at ∼1550 nm ($^4I_{13/2} \rightarrow {}^4I_{15/2}$) and in most of the high resolution investigations the $^4I_{13/2}$ manifold is directly excited. Here, we are interested to a condition where the excitation source is widely separated in energy from the luminescence. In this way, we are able to select the luminescence by using bandpass filters. In particular, we choose to excite the ions through the $^4I_{15/2}(1) \rightarrow {}^4I_{9/2}(1)$ transition (Fig. 2.2) by employing the following lasers:

- **Avesta Titanium Saffire [Ti:Sapphire (I)]** laser: it is pumped by a continuous wave 6 W Verdi G6 laser. Its several hundreds of mW power can be tuned between 700 nm and 990 nm and has a linewidth of 1-2 GHz.
- **Coherent 899 Titanium Saffire [Ti:Sapphire (II)]** laser: a power output of 400 mW is reached when it is pumped by a continuous wave (cw) 12 W Millennia laser at 532 nm. An external-cavity Fabry-Prot system is used for the frequency stabilization. It is tunable in the (760-820) nm range and has a linewidth of 10 MHz.

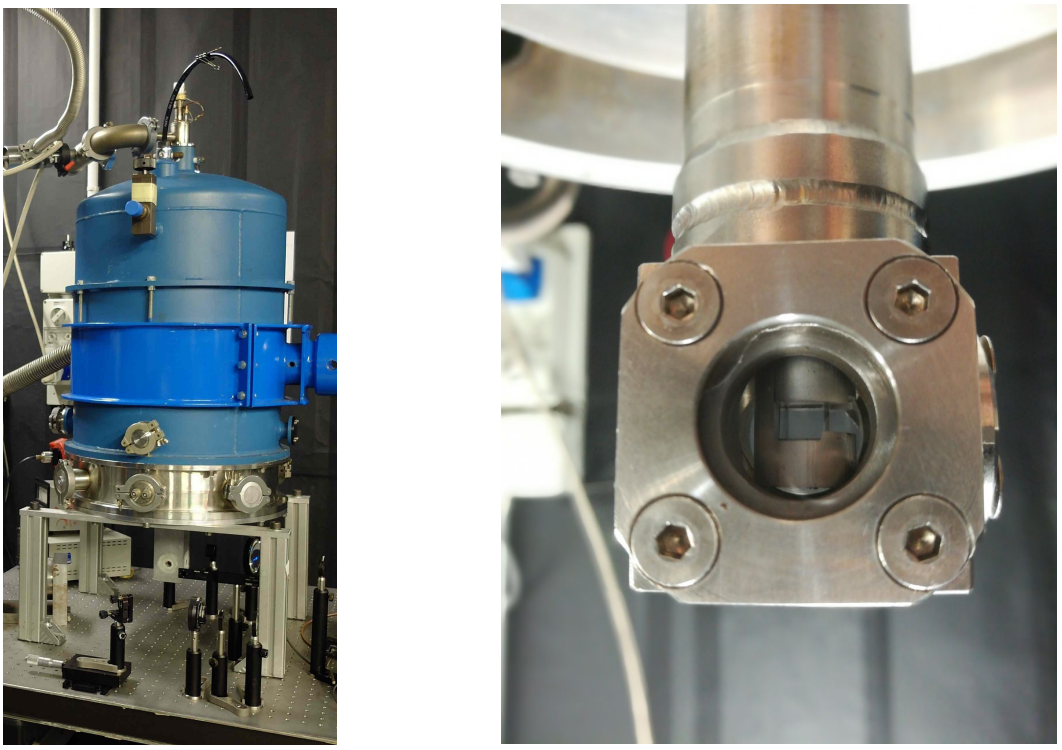

FIGURE 2.3: Photos (left) of the liquid Helium cryostat and (right) of the sample cell with the aluminum crystal holder and Er:YLF 0.01% sample.

The wavelength measurement with 0.1 pm accuracy is provided by a Burleygh WA-1500 wavemeter.

2.3.3 Detectors

Laser absorption and the crystal luminescence are analyzed through different devices:

- **Photodiodes** (PD). The used InGaAs based photodiodes (Thorlabs DET10C and DET20C) have a rise time of 10 and 25 ns and an active area of 0.8 and 3.1 mm^2. The photodiodes signal can be amplified by a transimpedance amplifier (Femto, mod. DPLCA200) with adjustable gain.
- **Bolometers.** Light beam power is readily measured by a calibrated Silicon and Germanium-based power meters.
- **Spectrometer:** Ocean Optics, mod. NIRQuest512. This InGaAs CCD-based spectrometer is thermoelectrically cooled down to -20 °C and is able to acquire the spectrum in the range (900-1700) nm with an optical resolution of 3-5 nm.

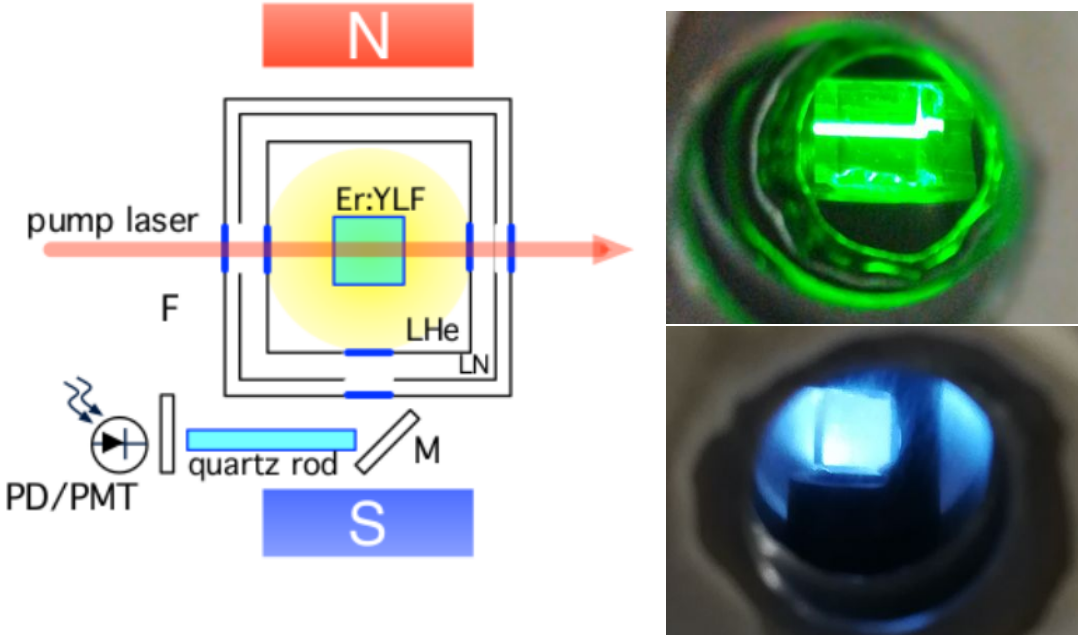

FIGURE 2.4: (Left) Laser-induced fluorescence experimental setup. During the tests the crystal is immersed in LHe or superfluid He. Fluorescence is collected orthogonally to the laser propagation direction by means of a mirror (M) that couples light to a 10 cm-long quartz guide. Optical filters (F) are set in front of the InGaAs photodiode (PD) to remove stray light. (Right) Photos taken at two viewpoints. (up) Ti:Sapphire (I) excites the crystals at 1.6 K at the frequency to accomplish two subsequent photon absorption and green light emission. (down) A LED is used to illuminate the crystals at 4.2 K.

2.4 Optical transitions

As summarized in Tab. 1.3, inhomogeneous linewidths narrower than 1 GHz have been reported for optical transitions in Er:YLF and Er:YSO at cryogenic temperatures, and Zeeman splittings of tens of GHz could be well resolved. However, in the reported experiments the sample concentration was much smaller than 0.1% to avoid homogeneous broadening due to mutual RE ions interactions. It must be noted that 1 mole of Er^{3+} ions doped YLF at 0.01% occupies $\sim 0.5\,m^3$. This volume is experimentally difficult to cool down to mK temperatures, whereas 1 mole of Er^{3+} ions is obtained in the reasonable volume of $5\,dm^3$ for a higher concentration crystal (Er:YLF 1%). It is thus necessary to study the spectroscopic properties of crystal with concentration higher than 0.1% to assess if the inhomogeneous broadening affects the isolation of the optical transitions.

We study and compare the spectral features of two Er:YLF single crystals doped at 0.01% and 1%. The experimental and the upconversion scheme are depicted in Fig. 2.4 and in Fig. 2.2, respectively. The Zeeman splitting energy of the ground state under a magnetic field of 370 mT and the relative transitions linewidth are

investigated through laser induced fluorescence measurements. The wavelength of the Ti:Sapphire laser (I) output is tuned around the resonance between the two lowest Stark levels of $^4I_{15/2}$ and $^4I_{9/2}$ manifold at ∼809 nm. The intensity of the emission component in the (1500-1650) nm range stemming from $^4I_{13/2}$ manifold is collected parallel to the laser propagation direction by a InGaAs PD coupled with the transimpedance amplifier.

2.4.1 Er:YLF 0.01% spectroscopy

The InGaAs PD is used to obtain the excitation spectrum for the Er:YLF 0.01% at 4.2 K shown in Fig. 2.5a. A sharp absorption line is recorded whose linewidth is limited by that of the laser. Two satellite lines at few GHz distance are observed, compatible with the presence of $^{167}Er^{3+}$ ions and its nuclear spin. When the magnetic field of 370 mT is applied along the c-axis, 4 well resolved transitions appear due to the removed degeneration. We show the two excitation spectra for the incident laser field polarization E∥c in Fig. 2.5b and E⊥c in Fig. 2.5c.

The insert in Fig. 2.5c display the selection rules for allowed electric dipole in Er^{3+} according to the spin level representation Γ_i. As calculated in [30] the two states composing the $^4I_{15/2,5/2}$ and $^4I_{9/2,9/2}$ levels can be labeled with spin representation $\Gamma_{5,6}$ and $\Gamma_{7,8}$, respectively. According to the selection rules, we observe two transitions with dominant σ polarization and two with π polarization. The small discrepancy of the peak intensity for the coupled transition is due to different population of the ground state Zeeman sublevels at 4.2 K for the obtained splitting energy. This discrepancy allows us to identify the initial and final levels of each transition.

The two external absorption lines can always be unequivocally associated to the transitions 1 and 4 (Fig 2.5a) in contrast with the inner ones. However, the higher intensity of the transition at 808.996 nm indicates that it arises from the lower Zeeman level of ground state and thus it is labeled with number 2 with reference to the scheme in insert of Fig. 2.5a.

The splitting energy and the $\bar{g}$-factor along the c-axis for the ground state (g) and the excited level (e) can indeed be calculated starting from the measured resonance energy E_i as follows:

$$\Delta E_g = E_2 - E_1 = E_4 - E_3 \qquad \bar{g}_g = \Delta E_g/(\mu_B B) \tag{2.7}$$

$$\Delta E_e = E_2 - E_1 = E_4 - E_3 \qquad \bar{g}_e = \Delta E_e/(\mu_B B) \tag{2.8}$$

In particular, we obtain $\Delta E_g = 64.5 \pm 1.4\,\mu$eV, $\Delta E_e = 75.8 \pm 1.4\,\mu$eV and $\bar{g}_g = 3.0 \pm 0.1$, $\bar{g}_g = 3.5 \pm 0.1$. The obtained $\bar{g}$-factors are in good agreement with that estimated using EPR and high resolution spectroscopy $\bar{g}_g = 3.137$ and $\bar{g}_g =$

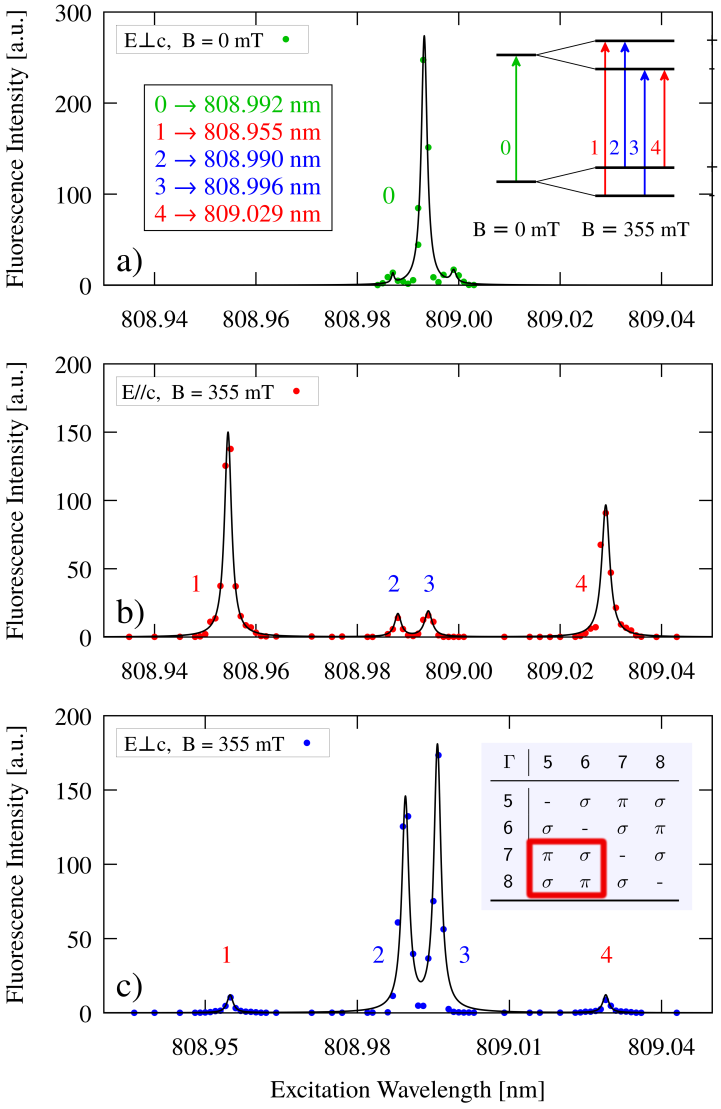

FIGURE 2.5: Excitation specta of Er:YLF 0.01% $^4I_{15/2,5/2} \rightarrow {}^4I_{9/2,9/2}$ transitions a) without and b), c) with the applied magnetic field for different polarization. The fluorescence intensity in the infrared band is measured with the InGaAs PD (II). The black lines are the Lorentzian functions that fit the data. The laser power is set at 100 mW and the laser beam diameter at 1.7 mm. The inset in a) indicate the origin of each absorption lines. The inset in c) shows the selection rules that govern the absorption intensity according to the laser polarization.

3.72 [31]. If we consider the ratio of the $\bar{g}$-factor a discrepancy less than 1% is found indicating that a shielding effect due to the cryostat could slightly reduce the static magnetic field experienced by the crystal. A value of 355 mT fits better the data instead of 370 mT.

2.4.2 Er:YLF 1% spectroscopy

The results obtained for Er:YLF crystal doped at 1% are shown in Fig. 2.6. The four transitions are separated likewise for the Er:YLF 0.01% but are also much inhomogeneously broadened and with several laser polarization-dependent satellite lines. Crystal defects and impurities cannot be responsible for these behavior because the low concentration should not affect the crystal structure and the growth condition was the same for the Er:YLF 0.01%. These additional lines could be due (1) Er^{3+} ions perturbed by the other dopant ion through crystal field perturbation, (2) to Er^{3+} pair ions in unperturbed sites interacting through magnetic or electric dipole force or (3) a combination of these mechanisms. In order to assess the dominant mechanism we also investigate the absorption linewidths that involves the doublet $^4I_{9/2,9/2}$ and the first Stark doublet of the ground state manifold $^4I_{15/2,15/2}$ which lies at $17\,cm^{-1}$ from the ground state level (Fig. 2.6c). In this case, there are no satellite lines in the excitation spectrum. It must be also considered that the Stark lifetime is reduced to ∼ns by multiphonon relaxation and the observed linewidths can be partially due to homogeneous broadening. This is confirmed by the fact that at lower temperature a narrower linewidth is recorded.

Perturbations of the crystal field should affect all transitions thus we can infer that (2) is the dominant factor that gives rise to the inhomogeneous broadening of the ground state absorption lines and that the ions in the excited Stark level is weakly coupled with that in the $^4I_{15/2,5/2}$ levels. At 4.2 K only the 0.3% of the Er^{3+} ions populate the excited Stark level and the couplings between the excited ions is negligible due to the large separation.

Basically, Er^{3+} ions can occupy the $^4I_{15/2,5/2}$ levels in the Zeeman state with M = 5/2 or with M = −5/2 and then can be described as system with an effective spin S_0=1/2. The interaction between two identical spin S_0^A and S_0^B is described by several contributions whose the most relevant in our case are the Heisenberg exchange and the pure magnetic dipole interactions. The hamiltonian term that takes into account the coupling behavior can be written as [58]:

$$H_{int}^{ss} = -2K\,\mathbf{S_0^A}\cdot\mathbf{S_0^B} + \mathbf{S_0^A}\cdot\overline{\overline{\mathbf{D}}}\cdot\mathbf{S_0^B} \qquad with \qquad D^{\alpha\beta} = \frac{\mu_B^2\bar{g}^\alpha\bar{g}^\beta}{r_{12}^3}\left(\delta_{\alpha\beta} - \frac{3r_{12}^\alpha r_{12}^\beta}{r_{12}^2}\right) \tag{2.9}$$

where the constant K represents the strength of the exchange process, r_{12} is the spin relative distance and α, β the component along the crystallographic axis. The first term induces an energy shift of the order of $K(r_{12})$, the second term of $D = 0.325\bar{g}^2(\theta)|1-\cos^2(\theta)|/r_{12}^3$, with θ the angle between the magnetic field direction and the pair ab axis [59]. With the introduction of these interaction, coupled ions at different distance are characterized by different levels also with respect of the uncoupled ones giving rise to the several satellite lines. As natural

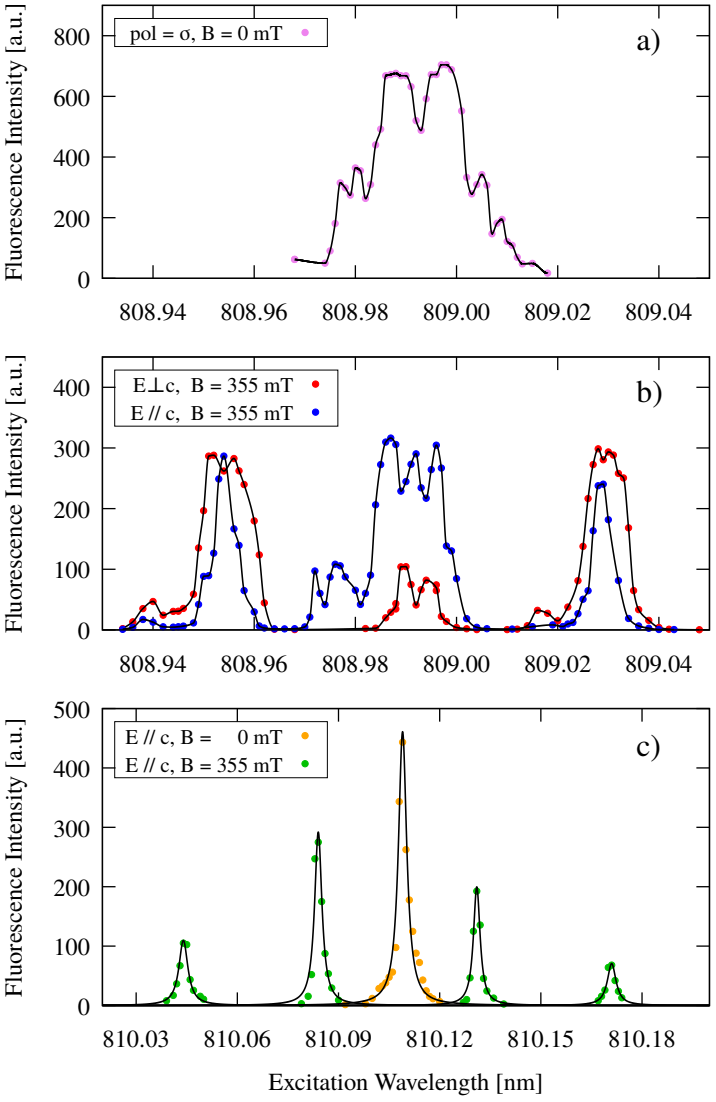

FIGURE 2.6: Excitation spectra of Er:YLF 1% for the $^4I_{15/2,5/2} \rightarrow {}^4I_{9/2,9/2}$ transitions a) without and b) with the applied magnetic field for different laser polarizations. Panel c) shows the features and the Zeeman splitting effect on the $^4I_{15/2,15/2} \rightarrow {}^4I_{9/2,9/2}$ transitions. The black lines in a) and b) are splines whereas in c) are the Lorentzian functions that fit the data. The crystal temperature is 4.2 K.

Erbium appears with 6 isotopes, one of them has a hyperfine splitting of several GHz, the possible pair combination can actually induce several satellite line in the optical domain. However, there are two values for θ whereby the magnetic field interaction is zero and the inhomogeneous broadening can be minimized even for heavier concentrations.

EPR experiments demonstrated that magnetic interaction is the leading mechanism for Er^{3+} coupling in $LiErF_4$ crystal. In particular, along with a main resonance, a transition at almost twice the energy was observed indicating simultaneous spin flips of a pair of coupled ions [60]. Even at low concentration couplings can be detected. For instance YSO crystal codoped with Er 0.02%, Eu 1% shows a feeble absorption line shifted of 51 GHz with respect of that of the independent Er^{3+} ion, ascribable to the Er-Eu pair [38].

It was also observed [61] that in highly symmetric elpasolite $Cs_2NaErCl_6$ crystals the superexchange Er^{3+}-Er^{3+} interaction splits the electronic ground state into 4 well resolved levels equally separated by an energy gap of $3\,cm^{-1}$. However, due to the spectral resolution limited to $2\,cm^{-1}$, the only conclusion we can draw is that inhomogeneous linewidth of each $^4I_{15/2} \rightarrow {}^4I_{13/2}$ transition is narrower than 60 GHz. To the best of our knowledge, there is no piece of information either about optical linewidth at low temperature for $LiErF_4$. However, for the Er:YLF doped at 1% sample the transition 4 does not overlap by far any other transition starting from the ground state. Thus it can be used for the Sikivie's scheme to accomplish the upconversion.

2.4.3 Er:YSO 0.1% spectroscopy

For comparison we repeat the measurements also for the Er:YSO 0.1% crystal. In this case, the laser absorption is much stronger and saturation effects characterize the emission intensity, absorption coefficient vs laser wavelength is reported (Fig. 2.7). Only sharp lines are present in the excitation spectrum and there is no indication of Er^{3+} pair formation. A larger splitting is obtained with $\Delta E_{gs} = 192.30 \pm 0.07\,\mu eV$ under the magnetic field and by taking $B = 355\,mT$ we estimate $\bar{g}_{gs} = 9.36$. Unfortunately, the crystal is not oriented and this result cannot be compared with values reported in the literature. Actually, the g-factor for the ground state of site 1 vary between 0.56 and 14.6 according to the crystal-magnetic field orientation [62].

The Stark levels in YSO are generally more separated than in YLF and the increasing mutual mixing in their wavefunction with the magnetic field should be smaller. This could arise a more linearity of the magnetic field dependent splitting and a lower uncertainty for the ΔE_{gs} value determination.

2.5 Upconversion efficiency

A crucial parameter to determine the ultimate performance of the proposed axion detector is the upconversion efficiency ϵ_{up}, defined as the fraction of the ions excited

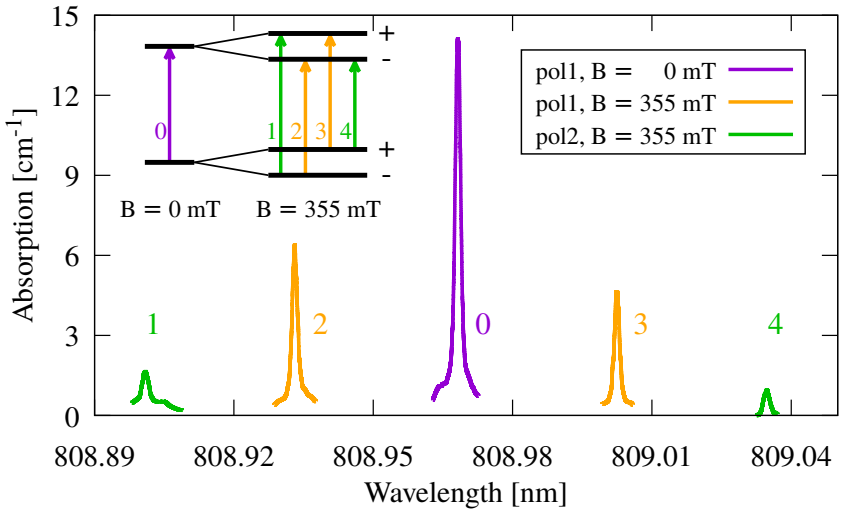

FIGURE 2.7: Absorption spectrum of Er:YSO 0.1% recorded at 1.6 K using the Ti:Sapphire laser (II) with a waist diameter of 320 μm. The incident laser power is 12 mW. The spectrum is acquired with a laser wavelength step of 0.1 pm and for clarity we show only the splines. The polarizations "pol1" and "pol2" are orthogonal and maximize the absorption.

via axion-ion interaction which are converted into a visible/near-infrared photon:

$$\epsilon_{\text{up}} = \frac{\sigma \dfrac{I}{h\nu}}{\dfrac{1}{\tau_z} + \sigma \dfrac{I}{h\nu}} = \frac{1}{1 + \dfrac{h\nu}{\sigma I \tau_z}} \tag{2.10}$$

I is the laser intensity, $h\nu$ the laser photon energy, σ the ion absorption cross section for the laser photon and τ_z the upper Zeeman level lifetime. ϵ_{up} is unitary when the relaxation rate of upper Zeeman to the lower one is negligible.

2.5.1 Upper Zeeman level lifetime

Relaxation times of 7 ms and 1.1 ms have been reported for Er^{3+} upper Zeeman level in YSO crystal doped at 0.005% and 0.02% respectively. These results have been obtained in photon echo experiments performed at 1.6 K and under a magnetic field of 0.5 T that corresponds to 42 GHz Zeeman splitting energy [23]. It is worth noticing that the mentioned relaxation time values are considered a lower limit to our purposes as the ϵ_{up} is independent of the spin flip-flop process. Actually, the only process that is accounted for the τ_z is the spin-lattice relaxation and its rate is well described by Eq. 1.19 as verified the data acquired with the pulse saturation technique in ^{170}Er:$LaCl_3$ 1% [63]. The spin relaxation rate strongly decreases with temperature and a relaxation time of 160 ms is reported at 0.2 K for a Zeeman level lying at 16.6 GHz (= 68.7 μeV). At this temperature the Orbach

and Raman process are negligible and shorter lifetimes are expected for larger splitting energy owing the B^5 dependence of the direct process rate (see Eq. 1.19). In Er:YLF a $\sim 2\,\text{ms}$ lifetime is reported for the upper Zeeman level at 36.2 GHz ($= 150\,\mu\text{eV}$) [64, 65].

As the magnetic field is increased and the spin flip-flop rate becomes negligible, the coherence time of the excited Zeeman level tend to the spin relaxation time. For Er:YSO 0.02% a value of $\alpha_D = 1.1\,\text{Hz/T}^5$ (see Eq. 1.19) at 1.6 K has been reported, that corresponds to a lifetime $\tau_z = m \cdot \Delta E^{-5}$ with $m = 2.2 \cdot 10^{10}\,\text{s}/\mu\text{eV}^5$. In particular, $\sim$100 μs are observed for an energy splitting of 170 GHz ($\sim$700 μeV). From the data of Er:$LaCl_3$ and Er:YLF a much shorter time ($\sim 1\,\mu\text{s}$) can be inferred for the same splitting energy, using the measured parameter $m = 2.4 \cdot 10^8\,\text{Hz}/\mu\text{eV}^5$. We will use the latter value for preliminary estimates for ϵ_{up}, keeping in mind that much longer lifetimes might be attained.

2.5.2 Effective absorption cross section

Besides a longer level lifetime, the other crucial crystal parameter to achieve a high upconversion efficiency is the absorption cross section σ. If $n(\omega)$ is the density of atoms/ions that are resonant at the laser frequency ω, the absorption coefficient α is defined as $\alpha(\nu) = \sigma n(\nu)$ and it can be estimated in spectroscopic measurements by using the well-known Lambert-Beer law:

$$I(\nu, L) = I(\omega, 0)e^{-\alpha(\nu)L}$$

which expresses the attenuation of the intensity of a monochromatic beam of light at frequency ω along an optical path length L. In the case of RE ions at low temperature, it is not easy to estimate the absorption cross section. The homogeneous linewidth is in fact narrower than the inhomogeneous one, and only a small fraction of available ions participate to the absorption process. In Fig. 2.8 are shown the absorption coefficients acquired for $^4I_{15/2}(1) \rightarrow {}^4I_{9/2}(1)$ transition in Er:YLF 0.01% and in Er:YSO 0.1% crystal at 1.6 K. The absorption parameters are reported in Tab. 2.8 together with those reported for ^{170}Er:^{7}LiYF$_4$ [66].

One might expect the absorption coefficient to linearly scale with the concentration, but we obtain comparable values for Er:YLF 0.01% and 1% due to the inhomogeneously broadened linewidths, much larger for the 1% concentration sample. The homogeneous linewidth of each ion transition is expected to be in kHz-MHz domain, that is much narrower than the observed inhomogeneous linewidth. The absorption cross section can be estimated by multiplying α/n for the ratio Γ_{ihn}/Γ_h, obtaing values at cryogenic temperature that are much larger than those measured at room temperature ($10^{-21} - 10^{-19}\,\text{cm}^2$). This is the result of the oscillator dipole

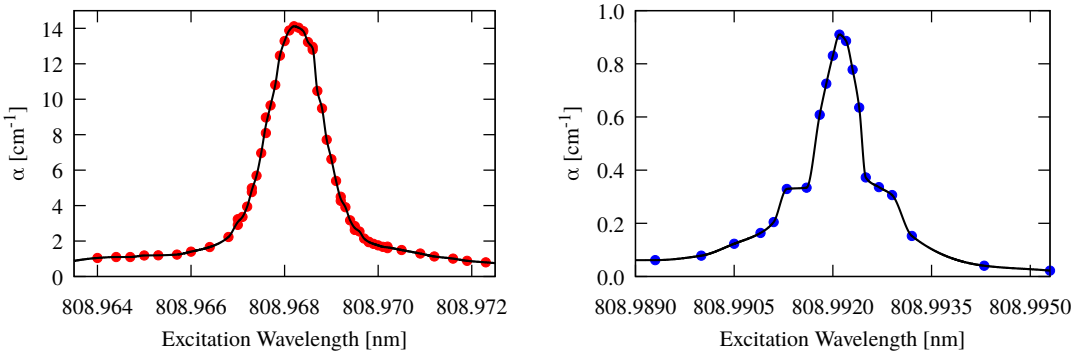

FIGURE 2.8: Absorption coefficient as a function of the excitation wavelength for Er:YSO 0.1% (red dot) and Er:YLF 0.01%(blue dot), both measured with input Ti:Sapphire (II) laser intensity of $\leq$36 W/cm^2. The black splines are drawn as a guideline. Note the structure in the absorption profile of Er:YLF, ascribable to the different isotopes of Erbium.

TABLE 2.1: Properties and obtained features of the $^4I_{15/2}(1) \rightarrow {}^4I_{9/2}(1)$ transition of the crystal investigated in this work. The values of a isotopically purified sample reported in the literature [66] for the $^4I_{13/2}(1) \rightarrow {}^4I_{15/2}(1)$ transition at 1532 nm are also included for comparison.

Crystal	**Concentration**	**Er^{3+} Density** [atom/cm^3]	**FWHM** @809 *nm*	**Absorption** [cm^{-1}]
Er:$LiYF_4$	1%	$1.4 \cdot 10^{20}$	$\sim$ 12 GHz	≈ 2
Er:$LiYF_4$	0.01%	$1.4 \cdot 10^{18}$	$\sim$ 400 MHz	0.8
Er:Y_2SiO_5	0.1%	$9.4 \cdot 10^{18}$ [a]	$\sim$ 600 MHz	14.1
^{170}Er:$^7LiYF_4$	0.005%	$0.7 \cdot 10^{18}$	16 MHz	41 [b]

[a] This includes the ions in the site 1.
[b] A magnetic field of 0.02 T is applied and the ion population is .

strength when very narrow homogeneous linewidths are achieved. In this way, according to the Eq. 2.10, high upconversion efficiency can be accomplished with small intensity by a narrow laser, but only for a fraction of the ions given by $\sim \Gamma_h/\Gamma_{ihn}$.

Because the axion-ion interaction is extremely weak, it is necessary to probe all the target ions using a pump laser with linewidth δ_l comparable with the inhomogeneous linewidth of the detector medium. Under this condition we can define the effective cross section of each ion as :

$$\sigma_{eff} = \frac{\int_{\delta_l} \alpha d\nu}{n\delta_l} \tag{2.11}$$

For the absorption parameters relative to the isotopically purified crystal ^{170}Er-doped $^7LiYF_4$, we estimate $\sigma_{eff} \approx 10^{-16}$ cm^2 and an upconversion efficiency $\epsilon_{up} = 84\%$ for $\tau_z = 10$ ms and $I = 1$ W/cm^2. To get the same upconversion efficiency in

Er:$LiYF_4$ 1%, a three order of magnitude more intense pump laser ($\sim$1 kW/cm^2) is required, as a result of the much smaller effective absorption cross section σ_{eff}.

2.5.3 Upconversion efficiency of the axion detector

The dependence of the upconversion efficiency on axion energy is finally reported in Fig. 2.9 for three laser intensities assuming a reasonable cross section of 10^{-18} cm^2 and the m parameter of the Er-doped $LaCl_3$ [1]. If the m parameter estimated for the Er:YSO crystal is confirmed, the same efficiency calculated for Er:$LaCl_3$ will be obtained with a hundred times smaller laser intensity and the axion energy range (20-150) μs could be explored with an upconversion efficiency higher than 50% for a laser intensity of 1 W/cm^2.

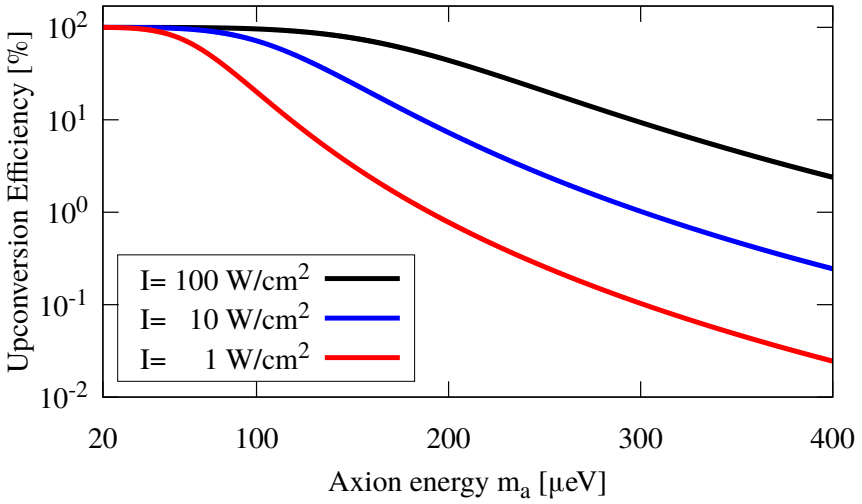

FIGURE 2.9: Upconversion efficiency dependence on the axion mass. The plotted curves are obtained by Eq. 2.10 with the explicit dependence on the splitting energy introduced by the equation $\tau_z = m \cdot \Delta E^{-5}$, with $m = 2.4 \cdot 10^8$ Hz/μeV^5.

2.5.4 Working temperature

A axion signal can be detected if the thermal population N^+ of the upper Zeeman level is negligible. According to the Boltzmann distribution, the latter exponentially decreases with the temperature:

$$N^+ = N\frac{e^{-\bar{g}\mu_B B/k_b T}}{e^{-\bar{g}\mu_B B/k_b T}+1} \approx Ne^{-\bar{g}\mu_B B/k_b T}, \tag{2.12}$$

where N is the total number of the Er^{3+} ions and the approximation holds when $\bar{g}\mu_B B/k_b T \gg 1$. The total number of upward and downward spin flip per unit

[1] Similar efficiency are expected if the YLF matrix is considered.

time for the N ions must be balanced at thermal equilibrium, therefore we can express the upward spin flip rate for the N ions as:

$$R_s = \frac{N^+}{\tau_z} = \frac{N}{\tau_z} e^{-\bar{g}\mu_B B/k_b T}. \tag{2.13}$$

If we aim for a signal to noise ratio SNR>3 for 10^4 s integration time, then $\sqrt{R_s} < \sqrt{10^4\, s} \cdot N_a R_i$. By substituting Eq. 1.19 and Eq. 2.6 in Eq. 2.13, we obtain for the working temperature for the axion resonance:

$$T_w < -\frac{m_a}{2k_b}\left[ln\left(3\left(\frac{100\,\mu eV}{m_a}\right)^2\sqrt{\frac{\tau_z}{N_a}}\right)\right]^{-1} = -\frac{m_a}{2k_b}\left[ln\left(\frac{3\cdot 10^4}{m_a^{9/2}[\mu eV^{9/2}]}\sqrt{\frac{m}{N_a}}\right)\right]^{-1} \tag{2.14}$$

where in the last equality the dependence of τ_z on the splitting energy has been made explicit through the constant m. In Fig. 2.10 the working temperature vs axion masses is plotted. For 100 μeV axion detection, we need to cool a mole of target atoms down to 53 mK.

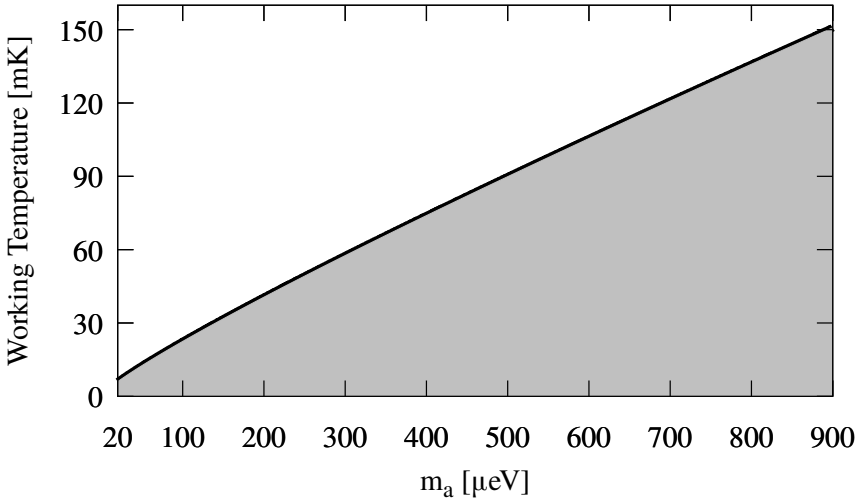

FIGURE 2.10: Plot of the minimum detector working temperature (black line) as function of the energy investigated for axion resonance. The acceptable temperature-energy area is colored in grey.

2.6 Spurious laser induced fluorescence

As discussed in previous section, the upconversion efficiency of the axion detector drops for increasing axion mass m_a. On the other hand, large splittings allow for higher working temperature but highest laser intensities are required to compensate the efficiency loss. At required working temperature it is thus mandatory to

assess the laser-related thermal heating effect or, equivalently, the degree of transparency to laser radiation of the cooled RE-doped material. Spurious LIF might be caused by crystal impurities and phonon-related processes.

2.6.1 Laser heating effect

As preliminary study of possible laser-related heating effect, we measure the LIF intensity when the pump laser is tuned to the transition ${}^4\mathrm{I}_{15/2}(2) \rightarrow {}^4\mathrm{I}_{9/2}(1)$ level, where ${}^4\mathrm{I}_{15/2}(2)$ is thermally excited at the temperature of the experiment. This first Stark level lies ΔE =17 cm^{-1} above the ground state. In this context we introduce a procedure to estimate temperature variations that depend on the pump laser intensity.

During the measurement the Er:YLF 1% crystal temperature is kept at 1.9 K. Under this condition, only a fraction as high as $2 \cdot 10^{-6}$ of the total ion density thermally populates the mentioned level. Any slight change of the temperature induces a large variation of the population and thus of the LIF. At the first order we can assume that the temperature increases linearly with I, i.e. $\Delta T = \alpha_h I$. As the absorption cross section is independent of the temperature, the related LIF is given by:

$$F(I) \propto N\, I\, e^{\frac{\Delta E}{k_b(T_w+\Delta T)}} = N\, I\, e^{\frac{\Delta E}{k_b(T_w+\alpha_h I)}} \approx N\, I \left(1 + \frac{\Delta E}{2T_w^2}\alpha_h I\right) e^{\frac{\Delta E}{k_b T_w}} \qquad (2.15)$$

A laser heating effect would then seed a spurious LIF that depends on I^2. The purely linear trend we observe (see Fig. 2.11) rules out heating effects related to $\alpha_h > 4.5\,\mathrm{mK/(W/cm^2)}$ with 95% confidence level.

The laser heating must however investigated at ~ 100 mK temperatures. This can be accomplished by applying the described procedure to the upper Zeeman split level of the ground state.

2.6.2 Multiphonon assisted laser absorption

A laser photon can be absorbed by RE ions embedded in crystals even if it is not resonant with any of their levels thanks to the involvement of one or more phonons. This process is called multiphonon-assisted absorption.

Let us consider two manifolds E_1 and E_2 and a non resonant laser photon with energy E (Fig. 2.12a). The absorbed laser intensity is given by :

$$I_a(E) = I_a(E_1)e^{-\alpha_S(E-E_1)} + I_a(E_2)e^{-(\alpha_S+1/k_bT)(E_2-E)}, \qquad (2.16)$$

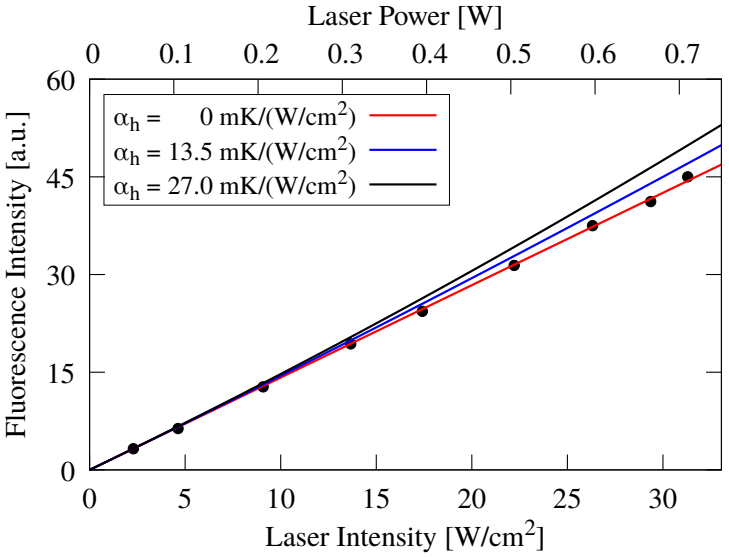

FIGURE 2.11: Laser power dependence of the LIF with the laser (I) tuned on the first Stark level of Er:YLF 1% (black dot). The crystal temperature is 4.2 K and the laser waist diameter is set to 1.7 mm. The function defined by Eq. 2.15 is plotted for different values of α_h. The slope coefficient are set by performing a linear regression in low excitation regime.

where $I_a(E_i)$ represents the absorbed intensity for photons of energy E_i. The two term in Eq. 2.16 arise from the Stokes and Antistokes processes. The α_S is Stokes parameter and accounts for the coupling strength of the process. In the Stokes process, a laser photon excites the RE ion to the level E_1 and the excess energy is released by phonons emission as depicted in Fig. 2.12a,b. In the Antistokes process, the level E_2 is excited and the missing energy is bridged by phonons absorption. As its occurrence relies on the energy of the thermal bath, it is suppressed at low temperature. The Stokes process is instead temperature independent and its rate exponentially depends on the number of phonons required to bridge the energy gap as α_S is proportional to the inverse of the host phonon energies.

We choose to study the Stokes process on the Er:YLF 1% crystal because a higher sensitivity to the process rate is ensured by the higher number of Er^{3+} ions. In particular, we vary the laser excitation wavelength between the $^4I_{9/2}$ and $^4I_{11/2}$ manifold and we indirectly probe the $^4I_{11/2}$ population induced by Stokes process by registering the LIF intensity in (1500-1650) nm range (Fig. 2.12b). To further enhance the sensitivity, we amplify the InGaAs PD (DET20C, Thorlabs) signal through the lock-in technique. The modulation of the continuous wave laser pump is given by a mechanical chopper with variable frequency up to 1 KHz.

As shown in Fig. 2.12c, when the laser is tuned at resonance with the $^4I_{9/2}(1)$ level we observe the maximum of the emission intensity, that is reduced by factor 10^6 as soon as the laser is slightly detuned. The LIF exponentially grows with the increasing laser wavelength and the decreasing of the difference $E - E_1$. We

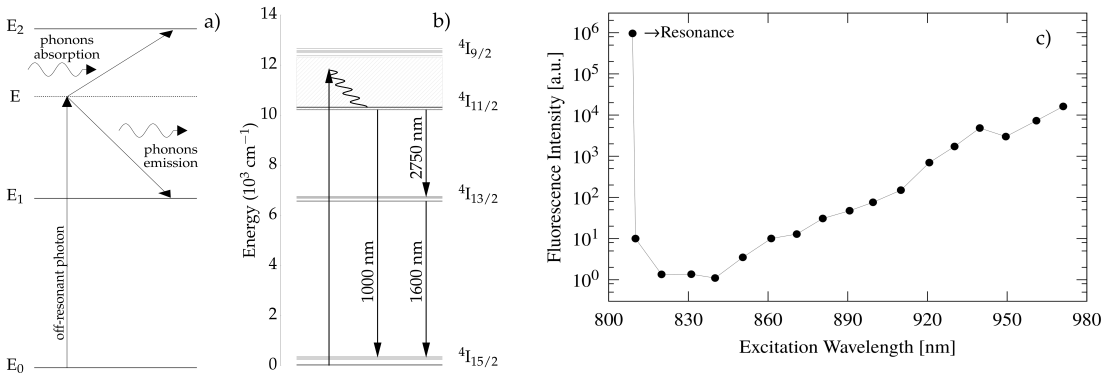

FIGURE 2.12: Scheme of the multiphonon assisted absorption (a). The multiphonon assisted absorption in the case of Er:YLF and for the transition investigated in this thesis (b). Laser induced fluorescence as function of the excitation wavelength at 4.2 K. Similar results are obtained by applying the magnetic field, by varying the laser polarization and changing the temperature.

believe that the costant values observed in (820-840) nm are due to instrumental limit. Our results support the model described by Eq. 2.16 and by fitting tha data in the range (840-970) nm, we find $\alpha_S = 9.2 \cdot 10^{-3}\,\mathrm{cm}^{-1}$ that is in agreement with the value reported in [18] for YLF crystal. Note that the unintended population of $^4I_{11/2}$ and the subsequent multiphonon relaxation relaxation between Stark levels and manifolds, provoke the release of phonon that may induce spin flips in other Er^{3+} ions and an increase of spurious LIF.

Mitigating the multiphonon relaxation

Two different solution can be adopted to minimized the multiphonon relaxation. The first is to use host materials with smaller phonon energies. For instance, fluoride crystals are more suitable than oxides. Chlorides, Bromides and Iodide compounds are even better than fluorides as their maximum phonon energy is lower than $300\,\mathrm{cm}^{-1}$, but they are not practical due to their high hygroscopic nature.

The second possibility is to choose a different upconversion scheme where the difference $E - E_1$ is as high as possible. For instance, if the pump laser is tuned between the $^4I_{15/2}(1)$ and $^4I_{13/2}(1)$, a three times greater gap $E - E_1$ is gained with respect the previous upconversion scheme and the suppression factor of 10^{-18} is achieved with respect to the resonance[2]. In this way, however, the fluorescence and the pumping laser are characterized by similar wavelength and the latter is difficult to filter out. Fortunately, there are other RE ions which provide more interesting transitions in terms of $E - E_1$ difference and also absorption cross section.

[2]This is derived assuming the validity of Eq. 2.16 even where more than 10 phonons are involved.

2.6.3 Crystal impurities

The presence of impurities is another possible source of spurious laser induced fluorescence that must be considered in the proposed detection scheme. For example, transition metal can be found in the host crystal in concentration not less than part per million and have large absorption cross section and wide excitation band in YLF [67]. Impurities can absorb the laser photon and yield their energy to the RE ions, inducing fluorescence and spin flip as well. Unfortunately, our apparatus has not enough sensitivity to assess this noise source.

2.7 Discussion

We have discussed the Sikivie's upconversion scheme for the axion detection. Inhomogeneous linewidth are narrow enough to resolve the Zeeman splitting for the tens to the hundreds GHz range in optical transition. However, the main obstacle for the axion detector is to achieve sufficient sensitivity which may be strongly affected by the laser excitation. The required laser intensity is determined by the desired upconversion efficiency value through two fundamental experimental parameters, the effective absorption cross section and the lifetime of the upper Zeeman level. Furthermore, a high RE ions density is needed due to the weak axion interaction to obtain a relevant event rate. As a result, the choice of the target crystal must combine the condition on the heavy concentration, on the low spin lattice relaxation rate and on the linewidth that have to be as narrow as possible. Unfortunately, the proximity of RE ions induces pair coupling that in turn causes inhomogeneous broadening.

It is worth mentioning that the Stark excited level of Er:YLF 1% exhibits much narrow linewidth than the ground state indicating a low pair formation. If such behavior would also transferred to the upper Zeeman level under very low temperature and strong magnetic field condition, then it should be possible even to exploit heavy concentrated crystal. Actually narrower linewidth is recorded when a magnetic field is applied and hence this aspect deserves further studies.

An interested case is provided by the spectroscopic feature of Tb:$LiYF_4$ 1% and $LiTbF_4$ reported in [68, 69]. Both crystals presents a Lorentzian-shaped absorption line, with a width equal to $\sim 13\,\mathrm{GHz}$ for the $^7F_6(1) \rightarrow {}^5D_4(1)$ Terbium transition and EPR measurements did not show any coupling effects. It was indeed suggested that the magnetic dipole interaction is inhibited as $\bar{g} = 0$ along the a,b axis for Tb in $LiYF_4/LiTbF_4$ [60]. In addition, Terbium is characterized by a single stable isotope with $I = 3/2$ and narrower linewidth can be readily achieved by purifying the Lithium atoms. The first excited Stark level lies at 30 GHz above the ground state and the dependence of this energy gap on the magnetic field strength is

described by a value of the g-factor as high as $\bar{g} = 17.85 \pm 0.10$ [60]. This means that a resonance with the axion mass could be probed with low magnetic field amplitude.

As regards the crystal that we have studied, the Er:YSO 0.1% is the most suitable with a recorded linewidth of 600 MHz. It has also large g-factor that with the optimization of the magnetic field alignment $\bar{g}_{gs} = 14.65$ is attainable [62]. The transition at 1536 nm in Er:YSO 0.02% is characterized by $\alpha = 50\,\mathrm{cm}^{-1}$ and $\Gamma_{ihn} = 0.34\,\mathrm{GHz}$ along the **D2** optical axis for site 1 [43]. Hence, we could excite almost all Er^{3+} ions occupying the site 1 of our crystal with a $\sim$1 GHz-linewidth laser, achieving an effective absorption cross section $\sigma_{eff} \approx 10^{-17}\,\mathrm{cm}^2$. The study of lifetimes of Zeeman level lying at 10s GHz range is highly recommended since the data for larger splitting seem to indicate a much smaller relaxation rate compared to that measured in YLF and $LaCl_3$ crystal. A lifetime longer than 100s milliseconds could therefore be assumed in YSO for that energy range and an upconversion efficiency higher than 50% can be obtained with a laser intensity less than $1\,\mathrm{W/cm}^2$. As this intensity is expected to be able to pass through the crystal almost entirely, the working temperature at tens of mK should be accomplished in a dilution refrigerator.

When one ion is excited by the pump laser and subsequently emits a photon, it can return into the initial upper Zeeman level with a certain probability. The ion can therefore absorb a photon again accomplishing a recycle process. In addition, several phonons could be released into the crystal during the multiphonon relaxation between Stark levels or manifolds. For instance, more than 90% of Er^{3+} ions in $^4I_{13/2}$ levels relax to the excited Stark levels of the ground state manifold before relaxing in the lowest one. The phonons emitted in the process can induce spin flips in the surrounding RE ions thereby amplifying the initial excitation. Hence, for each ions excited by axion interaction several photons could be emitted and detected. This aspect is useful to discriminate a real signal from the photon detector noise.

The energy gap between $^4I_{13/2}$ and $^4I_{15/2}$ is around $6500\,\mathrm{cm}^{-1}$ that could be bridged by seven phonons in YSO. The population of the Stark levels of $^4I_{15/2}$ via multiphonon assisted absorption might be not sufficiently suppressed. Actually, the spin flip rate caused by this process might be orders of magnitude higher than that induced by the axion wind. In this respect, the Terbium scheme offers a much interesting prospective with an energy gap of around $15000\,\mathrm{cm}^{-1}$. Furthermore, its emission in visible range rather than in infrared range can be detected with Silicon photomultiplier or photomultiplier tube which offer high quantum efficiency and lower noise rate.

The ultimate noise source related to laser excitation may arise from the undesirable impurities. The limit of different RE ions and several other atoms density is

nowadays set at least 10-100 part per billion. We believe that this factor may compromise by far the requested sensitivity for the axion detection.

However, the Sikivie's scheme shows features that could be useful in other field. This idea that is basically designed to acquired a spectrum in the μeV can be also found application as a bolometer. Any particle, radiation, photon from soft X ray to far infrared range can release energy into the crystal inducing spin-flips, that can be converted into near infrared/visible photons. In this case, the ground state energy splitting with the best parameters can be chosen. Furthermore, if larger energy deposition or higher event rate are considered, working temperatures of hundred of mK are acceptable and the laser induced noise might not suppress the signal.

Chapter 3

Superfluorescence: the theoretical background

The "ordinary fluorescence" is the incoherent, isotropic emission by an excited ensemble of atoms/molecules that decay independently via spontaneous emission. A coherent, directional emission is obtained in a laser, where the stimulated emission process establishes a phase relation among the photons. In superradiance processes the concept of coherence is even more profound as it is regards both the emitted photons and the involved atoms. In this case, the excited atoms/molecules are phase-locked and the ensemble behaves as a macroscopic dipole (MD), whose strength is N times that of the single emitters. The transition rate is then enhanced by a factor N and the radiated intensity scales with N^2 and its duration with $1/N$. We will refer to this emission as cooperative emission or superradiant decay.

In this work we adopt the definition of superfluorescence (SF) given by Bonifacio and Lugiato [70] as a cooperative process where a MD spontaneously arises from initially uncorrelated excited atoms/molecules. Superradiance (SR) is generally used as a synonym of cooperative emission, but here we refer to SR when the MD is prepared by an external coherent source.

The most comprehensive reviews about SR/SF are those by M. Gross and S. Haroche in 1982 [71], by J.H Eberly and by L. Allen[72] and the book by Benedict and co-authors in 1996 [73]. A more recent review of SR/SF in solid state systems, including quantum wells, is presented here [74].

The profound concept of superradiance was firstly introduced by R. H. Dicke in 1954 [3] for N coherently excited indistinguishable atoms that are enclosed within a small volume ($V \ll \lambda_0^3$ with λ_0 the emission wavelength). Later on, the condition regarding the initial dipole coherence was relaxed, showing that it could arise from

a spontaneous appearance of correlations between the single dipoles. Such theory is referred to as "Dicke model".

A more realistic description of SF was proposed by N. E. Reheler and J. H. Eberly [75] by removing the restriction on the ensemble volume. They considered a pencil-shaped dipole distribution and by starting from a quantum electrodynamics approach, they derived the SF/SR equations that also takes into account a radial dependence of the radiated intensity.

Two SF regimes were defined by Bonifacio and Lugiato who developed a fully quantum-mechanical model for SF. However, they pointed out that a semi-classical treatment of the obtained quantum atom-field equations provides a useful, consistent description of the phenomenon [76, 77]. SF dynamics can actually be obtained by the Maxwell-Bloch equations provided that the "quantum fluctuations" are included by setting an initial non zero MD.

However, we emphasize that complete master equations for SF propagating in three spatial dimension are lacking owing to the complexity to handle the nonlinear light propagation and diffraction, the dephasing processes, the non identical perturbation of the atoms, their possible degeneracy, and quantum fluctuations. As a consequence, only in few particular systems the approximated models are fully validated.

The goal of this chapter is to gain an understanding of the SF mechanisms, especially in terms of MD self organization. After the concept of superposition of states is simply given in the case of two correlated atoms, we describe the Dicke model, which shows the basic properties of SF. A more complex model, as that developed by Eberly and Bonifacio, requires experience in QED calculations and in profound knowledge of quantum optics theory. Therefore, we present here the main results obtained in those frameworks, and discuss their physical meanings. In the last part, we summarize the conditions for SF occurrence and describe the emission pattern. These aspects will be useful to discuss the experimental findings.

3.1 A simple example: two indistinguishable atoms

In order to gain an intuitive and qualitative picture of SR/SF, it is instructive to analyze the decay of two correlated identical atoms. The atoms can occupy the ground $|g\rangle$ or the excited $|e\rangle$ state, which are separated by an energy $\hbar\omega_0$. The spontaneous decay rate from $|e\rangle$ to $|g\rangle$ for each independent atom is determined by:

$$A_{e\to g} = \tau_0^{-1} = \frac{1}{3\pi\epsilon_0}\frac{|\langle e|\mathbf{d}|g\rangle|^2\omega_0^3}{\hbar c^3} \tag{3.1}$$

in which the bracket denotes the transition matrix element of the dipole moment operator $\mathbf{d}$ [78]. The following treatment is based on a simple statement. If the relative distance of the two atoms is shorter than the radiation wavelength $\lambda_0 = 2\pi c/\omega_0$ and a photon emitted from the system is collected, then it is not possible to know which atom has relaxed. The indistinguishable atoms must, therefore, be handled as a single quantum mechanical system. The 4 possible states can be normalized and symmetrized as:

$$|gg\rangle\,, \qquad |s\rangle = \frac{1}{\sqrt{2}}(|ge\rangle + |eg\rangle), \qquad |ee\rangle\,, \qquad |a\rangle = \frac{1}{\sqrt{2}}(|ge\rangle - |eg\rangle) \tag{3.2}$$

In analogy to a two-spin 1/2 systems, there are 3 symmetric triplet states and one antisymmetric single state, with $|a\rangle$ and $|s\rangle$ degenerate states as shown in Fig. 3.1. Eq. 3.1 can be applied to any arbitrary quantum systems, provided that their size is smaller than the emission wavelength. By taking into account that $\langle g|\mathbf{d}|g\rangle = \langle e|\mathbf{d}|e\rangle = 0$, the decay rate of the excited two-atoms levels induced by the total dipole moment $\mathbf{d_1} + \mathbf{d_2}$ can be readily calculated using Eq. 3.1:

$$\begin{aligned}
A_{ee\to s} &= \frac{1}{3\pi\epsilon_0}\frac{\omega_0^3}{\hbar c^3}|\,\langle ee|\mathbf{d_1}+\mathbf{d_2}|s\rangle\,|^2 = \\
&= \frac{1}{3\pi\epsilon_0}\frac{\omega_0^3}{\hbar c^3}\frac{1}{2}|\,\langle ee|\mathbf{d_1}|ge\rangle + \langle ee|\mathbf{d_1}|eg\rangle + \langle ee|\mathbf{d_2}|ge\rangle + \langle ee|\mathbf{d_2}|eg\rangle\,|^2 = \\
&= \frac{1}{3\pi\epsilon_0}\frac{\omega_0^3}{\hbar c^3}\frac{1}{2}|\,\langle e|\mathbf{d_1}|g\rangle\langle e|e\rangle + \langle e|\mathbf{d_1}|e\rangle\langle e|g\rangle + \langle e|g\rangle\langle e|\mathbf{d_2}|e\rangle + \langle e|e\rangle\langle e|\mathbf{d_2}|g\rangle\,|^2 = \\
&= \frac{1}{3\pi\epsilon_0}\frac{\omega_0^3}{\hbar c^3}2|\,\langle e|\mathbf{d}|g\rangle\,|^2 = 2A_{e\to g} \\
A_{s\to gg} &= \frac{1}{3\pi\epsilon_0}\frac{\omega_0^3}{\hbar c^3}|\,\langle s|\mathbf{d_1}+\mathbf{d_2}|gg\rangle\,|^2 = 2A_{e\to g} \\
A_{ee\to a} &= \frac{1}{3\pi\epsilon_0}\frac{\omega_0^3}{\hbar c^3}|\,\langle ee|\mathbf{d_1}+\mathbf{d_2}|a\rangle\,|^2 = 0 \\
A_{a\to gg} &= \frac{1}{3\pi\epsilon_0}\frac{\omega_0^3}{\hbar c^3}|\,\langle a|\mathbf{d_1}+\mathbf{d_2}|gg\rangle\,|^2 = 0 \\
A_{ee\to gg} &= \frac{1}{3\pi\epsilon_0}\frac{\omega_0^3}{\hbar c^3}|\,\langle ee|\mathbf{d_1}+\mathbf{d_2}|gg\rangle\,|^2 = 0
\end{aligned}$$

The results, displayed in Fig 3.1 show that the transition to and from the antisymmetric state $|a\rangle$ are forbidden. When this phosphorescence takes place it is called subradiance. The simultaneous de-excitation of the two atoms by the emission of a photon with energy $2\hbar\omega_0$ is inhibited as well. The cascading between symmetric states is accelerated, an effect that is even more marked for a larger atomic ensemble.

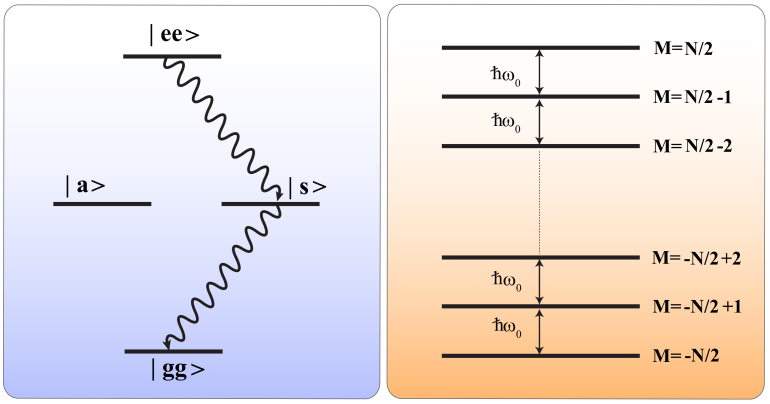

FIGURE 3.1: Diagram of the energy levels and allowed transitions for (left) two and (right) N coherent atoms.

3.2 The Superradiance in the Dicke model

We now extend our analysis of cooperative emission to N identical two-level atoms in a volume $V < \lambda_0^3$. The wavefunction of each atom state $|\psi\rangle$ can be expressed as a superposition $|\psi\rangle = c_e |e\rangle + c_g |g\rangle$ with the condition $c_e^2 + c_g^2 = 1$.

We define the usual operators over the two-dimensional Hilbert space for the i-th atom:

$$\mathbf{J}_{x,i} = \frac{1}{2}\sigma_1 \qquad \mathbf{J}_{y,i} = \frac{1}{2}\sigma_2 \qquad \mathbf{J}_{z,i} = \frac{1}{2}\sigma_3 \tag{3.3}$$

with σ_k the 2×2 Pauli matrices. These operators obey the angular momentum algebra:

$$[\mathbf{J}_{x,i}, \mathbf{J}_{y,j}] = i\mathbf{J}_{z,j}\delta_{i,j} \qquad [\mathbf{J}_{y,i}, \mathbf{J}_{z,j}] = i\mathbf{J}_{x,j}\delta_{i,j} \qquad [\mathbf{J}_{z,i}, \mathbf{J}_{x,j}] = i\mathbf{J}_{y,j}\delta_{i,j} \tag{3.4}$$

If we choose the zero energy level at the mid point of the two level energies so that $E(|g\rangle) = -\frac{1}{2}\hbar\omega$ and $E(|e\rangle) = \frac{1}{2}\hbar\omega$, the free Hamiltonian for the system of N independent atoms can be written as:

$$H_0 = \frac{1}{2}\hbar\omega_0 \sum_{i=1}^{N} (|e_i\rangle \langle e_i| - |g_i\rangle \langle g_i|) = \hbar\omega_0 \sum_{i=1}^{N} \mathbf{J}_{z,i} = \hbar\omega_0 \mathbf{J}_z \tag{3.5}$$

Here and henceforth, $\mathbf{J}_x = \sum_{i=1}^{N} \mathbf{J}_{x,i}$, $\mathbf{J}_y = \sum_{i=1}^{N} \mathbf{J}_{y,i}$, $\mathbf{J}_z = \sum_{i=1}^{N} \mathbf{J}_{z,i}$ represent the spin operators of the total system. For simplicity, we assume N to be even. H_0 has $N + 1$ eigenvalues:

$$E_M = M\hbar\omega_0 \qquad \text{with} \qquad M = N/2, N/2 - 1, ..., -N/2 + 1, -N/2 \tag{3.6}$$

where $M = (N_e - N_g)/2$ is defined as half difference between the atoms occupying the levels $|e\rangle$ (N_e) and $|g\rangle$ (N_g). $M = N/2$ ($M = -N/2$) corresponds to the situation whereby all the atom are in the excited (ground state) level. The degeneracy

of the total system energy level labeled by the number M is:

$$D_M = \binom{N}{N/2+M} = \frac{N!}{(N/2-M)!(N/2+M)!} \tag{3.7}$$

Let us define the raising and the lowering operators of the atoms and of the total system operators as:

$$\mathbf{J}_{+,i} = |e_i\rangle\langle g_i| = \mathbf{J}_{x,i} + i\mathbf{J}_{y,i} \qquad \mathbf{J}_{-,i} = |g_i\rangle\langle e_i| = \mathbf{J}_{x,i} - i\mathbf{J}_{y,i} \tag{3.8}$$

$$\mathbf{J}_{+} = \sum_{i=1}^{N} \mathbf{J}_{+,i} \qquad \mathbf{J}_{-} = \sum_{i=1}^{N} \mathbf{J}_{-,i} \tag{3.9}$$

The commutation relations are:

$$[\mathbf{J}_{z,i}, \mathbf{J}_{\pm,j}] = \delta_{ij}\mathbf{J}_{\pm,i}, \qquad [\mathbf{J}_{+,i}, \mathbf{J}_{-,j}] = 2\delta_{ij}\mathbf{J}_{z,i} \tag{3.10}$$

As one can easily calculate, the eigenvalues of the main operators are:

$$\mathbf{J}_z |N/2, M\rangle = M |N/2, M\rangle \tag{3.11}$$

$$\mathbf{J}_{\pm} |N/2, M\rangle = \sqrt{(N/2 \mp M)(N/2 \pm M + 1)}\, |N/2, M \pm 1\rangle \tag{3.12}$$

The interaction between the atoms is described by the electric field operator $\mathbf{E}$ and the atomic dipole moment $\mathbf{d}$. By assuming that all atomic dipoles are identical and by summing to a point-like dipole in $V \ll \lambda_0^3$, the Hamiltonian of the interaction is given by:

$$H_{int} = \mathbf{d} \cdot \mathbf{E} \sum_{i=1}^{N} (\mathbf{J}_{+,i} + \mathbf{J}_{-,i}) = \mathbf{d} \cdot \mathbf{E}(\mathbf{J}_{+} + \mathbf{J}_{-}) \tag{3.13}$$

According to Eq. 3.12 the transitions between states with neighbouring M values ($\Delta M = \pm 1$) are the only ones allowed. In addition, it is possible to show that the total spin operator of the total system $\mathbf{J}^2 = \mathbf{J}_x^2 + \mathbf{J}_y^2 + \mathbf{J}_z^2 = \frac{1}{2}(\mathbf{J}_{+}\mathbf{J}_{-} + \mathbf{J}_{-}\mathbf{J}_{+}) + \mathbf{J}_z^2$ commute with both H_0 and H_{int}. As a consequence, the eigenvalues of $\mathbf{J}^2$ must be conserved during the process. If we suppose that all atoms are initially in the excited state, then the radiative decay is a cascading transition between states characterized by the J^2-eigenvalue equal to $\frac{N}{2}\left(\frac{N}{2}+1\right)$, as illustrated in Fig. 3.1. These states $|N/2, M\rangle$ are totally symmetric and, once normalized, they

are expressed in the following way:

$$\begin{aligned} & |\underbrace{ee...e}_{N}\rangle && M = N/2 \\ \binom{N}{k}^{-\frac{1}{2}} & \left(\sum_{SYM} |\underbrace{ggg}_{k}..\underbrace{eee}_{N-k}\rangle\right) && M = N/2-k \\ & |\underbrace{gg..g}_{N}\rangle && M = -N/2. \end{aligned}$$

The matrix element that characterizes the allowed decay between states can be expressed as:

$$\begin{aligned} \langle N/2, M-1|\mathbf{d}(\mathbf{J}_{+}+\mathbf{J}_{-})|N/2,M\rangle &= \langle N/2, M-1|\mathbf{d}\mathbf{J}_{-}|N/2,M\rangle = \\ &= \langle g|\mathbf{d}|e\rangle \sqrt{\left(\frac{N}{2}+M\right)\left(\frac{N}{2}-M+1\right)}. \end{aligned}$$

The transition rate can be derived as

$$\begin{aligned} A_{M\to M-1} &= \frac{1}{3\pi\epsilon_0}\frac{|\langle N/2, M-1|\mathbf{d}\mathbf{J}_{-}|N/2,M\rangle|^2\omega_0^3}{\hbar c^3} = \\ &= \frac{1}{3\pi\epsilon_0}\frac{|\langle e|\mathbf{d}|g\rangle|^2\omega_0^3}{\hbar c^3}\left(\frac{N}{2}+M\right)\left(\frac{N}{2}-M+1\right) = \\ &= A_{e\to g}\left(\frac{N}{2}+M\right)\left(\frac{N}{2}-M+1\right) = \\ &= \frac{1}{\gamma_0}\left(\frac{N}{2}+M\right)\left(\frac{N}{2}-M+1\right) \end{aligned} \tag{3.14}$$

Starting from $|N/2, N/2\rangle$ state at $t = 0$ the rate equations that describe the probability of finding the system in the state $|N/2, M\rangle$ during the cascading transition are:

$$\begin{aligned} \frac{dP_M(t)}{dt} &= A_{M+1\to M}P_{M+1} - A_{M\to M-1}P_M = \\ &= \frac{1}{\gamma_0}\left[\left(\frac{N}{2}+M+1\right)\left(\frac{N}{2}-M\right)P_{M+1} - \left(\frac{N}{2}+M\right)\left(\frac{N}{2}-M+1\right)P_M\right] \end{aligned}$$

with the initial condition $P_M(0) = 1$ for $(M = N/2)$ and $P_M(0) = 0$ for $(M < N/2)$. The mean emission intensity is given by:

$$I(t) = -\frac{d\langle \mathbf{H_0}\rangle}{dt} = -\hbar\omega_0\frac{d\langle \mathbf{J_z}\rangle}{dt} = -\hbar\omega_0\sum_{M=-N/2+1}^{N/2} M\frac{dP_M(t)}{dt} \tag{3.15}$$

Here, $\langle\rangle$ indicates the expectation values. An exact numerical solution for $I(t)$ can be performed by integrating Eq. 3.15 step by step as long as the number of

atoms N is not large. However, the following analytic solution can be found under certain approximations [73]:

$$I(t) = \frac{N^2}{4\tau_0}\mathrm{sech}^2\left(\frac{N(t-\tau_d)}{2\tau_0}\right) \qquad \text{with} \qquad \tau_d \approx \frac{\ln N}{N}\tau_0 \tag{3.16}$$

The time evolution of the cooperative emission has the following properties. (i) For $t = 0$ Eq. 3.16 assumes the value N/τ_0, which coincides with the radiated intensity of N indipendent atoms. This result can also be deduced by Eq. 3.14 for $M = N/2$: $A_{N/2\to N/2-1} = N/\tau_0$. (ii) The intensity increases up till the system occupies the state $|N/2, 0\rangle$ and then decreases. (iii) The peak intensity peaks at $t = t_d$ and is proportional to N^2. (iv) The FWHM of the photon pulse duration scales as N^{-1}. These properties provide a means to unambiguously identify SF.

We want to remark that SR/SF arise from a correlation between dipole moments. The transition rate for the i-th atom is proportional to $\langle \mathbf{J}_{+,i}, \mathbf{J}_{-,i}\rangle$, that for the macro-states is:

$$\langle \mathbf{J}_+, \mathbf{J}_-\rangle = \langle \sum_i \mathbf{J}_{+,i} \sum_j \mathbf{J}_{-,j}\rangle = N\,\langle \mathbf{J}_{+,i}\mathbf{J}_{-,i}\rangle + N(N-1)\,\langle \mathbf{J}_{+,i}\mathbf{J}_{-,j\neq\, i}\rangle\,, \tag{3.17}$$

where the permutation symmetry has been used. The first term in Eq. 3.17 is the spontaneous emission from uncorrelated atoms, and the second one is superradiance. It is straightforward to demonstrate that:

$$\langle N/2, M|\mathbf{J}_{+,i}\mathbf{J}_{-,j}|N/2, M\rangle = \frac{\frac{1}{4}N^2 - M^2}{N(N-1)}. \tag{3.18}$$

This expectation value accounts for the coupling between the i-th and the j-th atoms. It is zero at the initial and the final states ($M = \pm N/2$). Otherwise, a non-zero correlation between the dipoles indicates that each single dipole accelerates the transition rate of the other emitters.

3.3 Superradiance in an extended medium

In the previous discussion we have omitted the near-field dipole-dipole interaction between the atoms. Unless improbable symmetric atom distribution and excitation, this interaction strongly affects the stringent condition of the identical quantum emitters. However, the validity of the above model is granted if we consider an extended, pencil-shaped active medium, namely a cylinder with a length L much larger than the radius w. The coupling of the atoms can be established only by photon modes that develop along the cylinder axis, and the atoms interact through their radiated field that satisfies the plane wave approximation. The

direct dipole-dipole interaction can be ignored if the relative distance between the atoms is large. The condition on the identical emitters is in this way preserved.

This selection of propagation modes along the cylinder axis implies that SR/SF occur in a preferred direction (forward and backward) and with a rate suppressed by a factor μ proportional to the diffraction lobe of the end surface of area S. The SF characteristic time is thus replaced by

$$\tau_R = \tau_0/(\mu N) \tag{3.19}$$

From the experimental point of view, the pencil-shaped geometry is naturally acquired by the atomic ensemble when laser beam seeds the population inversion.

We briefly discuss the results obtained with two different theoretical approaches, that model the SF in an extended medium. The first is useful to gain a simple and intuitive representation of the MD dynamics in analogy to a damped pendulum. The second approach allows us to predict the SF propagation pattern and provide the superradiant decay equation by including the geometrical correction factor μ.

3.3.1 A Semi-classical model

In the case of the pencil-shape geometry, the transverse components of the radiated field wavevector can be neglected. This is a key approximation to obtain a practical description of SF. This case has been analyzed by Bonifacio and Lugiato [76, 77] in a development of a model for SF based on the Maxwell-Bloch equations, first derived by Arecchi and Bonifacio in 1965 [79].

The Maxwell-Bloch equations determine the dynamics of a two-level quantum system interacting with the electromagnetic mode of an optical resonator. These equations involve macroscopic quantities such as the electromagnetic field amplitude, the medium polarization and the inverted medium polarization. Their evolution can be represented in the Bloch sphere, that is introduced in quantum optics as follows.

3.3.2 The Bloch sphere

Let us write the atom state as superposition of $|e\rangle$ and $|g\rangle$ pure states:

$$|\psi\rangle = \cos\theta\,|e\rangle + e^{i\phi}\sin\theta\,|g\rangle \tag{3.20}$$

where all possible states of the system are determined by (θ, ϕ) values which are modulo 2π periodic. Hence, each state can be associated to a point of a sphere with

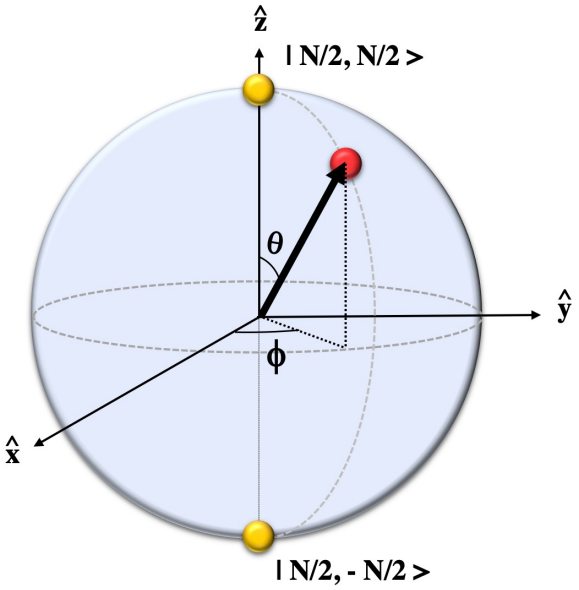

FIGURE 3.2: Bloch sphere representation. The red sphere and the black arrow represent the Bloch point and the vector, respectively. The pure states (where the population is fully excited or in ground state) are indicated by yellow sphere.

radius 1, called Bloch sphere and then to a vector starting from the center of the sphere called Bloch vector $\mathbf{r}$. The θ parameter is called tipping angle. Typically the $|e\rangle$ and $|g\rangle$ state correspond to the north ($\theta = 0$) and south pole ($\theta = \pi$), respectively. Thus, the component r_3 of the Bloch vector along the vertical axis z is relative to the probability of finding the atom in the excited state. In this analogy, the projection $\mathbf{r}_T$ on the plane xy represents the atomic polarization. In particular, the Bloch vector components r_1 and r_2 along the y and x axis are the quadrature components in phase and in amplitude, respectively, of the dipole moment. Under this representation, an electromagnetic plane wave with electric field amplitude E_0 is propagating along the x axis and determines the evolution of the Bloch vector.

The same representation can be applied to a system of N identical two-level atoms by considering a related Bloch sphere of radius $N/2$ shown in Fig. 3.2. $R_3 = (N/2)\cos\theta$ acquires the meaning of the inverted population and $R_T = N/2\sin\theta$ corresponds to the system polarization (i.e. the MD). For $\theta = 0$ ($\theta = \pi$) all the atoms are in the excited (ground) state and the Dicke macro-state $|N/2, N/2\rangle$ ($|N/2, -N/2\rangle$) is occupied.

3.3.3 The Maxwell-Bloch equations in superfluorescence

It has been shown [76, 77] that the evolution of N incoherently excited atoms is well described by a specific case of the Maxwell-Bloch equations,namely:

$$\begin{cases} \dfrac{d}{dt}\left(R_T^2 + R_3^2\right) = 0 \\ \dfrac{d}{dt}\left(A_T^2 + R_3\right) = -2kA_T^2 \\ \ddot{R}_3 + \left(k + \dfrac{1}{2T_2^*}\right)\dot{R}_3 = -\dfrac{1}{\tau_c^2}e^{-t/T_2^*}\left(2R_T^2 + 4A_T^2 R_3\right) \end{cases} \tag{3.21}$$

where $k = c/L$ has been introduced to approximate the radiation leakage rate out of the active volume V, T_2^* is the dipole dephasing time due to the inhomogeneous broadening of the emitters and $A_T \propto \dot{\theta}$ represent the emitted electromagnetic field intensity. The Arecchi-Courtens cooperation time τ_c [80] is defined through the expression:

$$\tau_c^2 = \frac{2\hbar\epsilon_0 V}{|\langle g|\mathbf{d}|e\rangle|^2 N\omega_0} \tag{3.22}$$

and it is the characteristic time of the energy exchange between the atoms and the electric field. The first equation implies that $R_T^2 + R_3^2$ is a constant of the motion and equals to $N^2/4$. Note that the two driving terms in the right hand side of the third equation accounts for SR/SF effects and for stimulated emission, respectively.

By recalling the definition of k, R_T and R_3, the dynamics of the systems represented by the Bloch vector and the radiated intensity is given by:

$$\ddot{\theta} + \left(k + \frac{1}{2T_2^*}\right)\dot{\theta} - \frac{1}{\tau_c^2}e^{-t/T_2^*}\sin\theta = 0, \tag{3.23}$$

$$I(t) = \frac{kN}{2\tau_c^2}e^{-t/T_2^*}\dot{\theta}. \tag{3.24}$$

According to Eq. 3.23, the Bloch vector acts as a damped pendulum with friction $(k + 1/2T_2^*)$ and oscillation frequency that decreases exponentially in time. If we assume that $T_2^* \gg \tau_R$, Eq. 3.23 is replaced by:

$$\ddot{\theta} + k\dot{\theta} - \frac{1}{\tau_c^2}\sin\theta = 0 \tag{3.25}$$

For $t = 0$ the radiated intensity is zero and thus $\dot{\theta}(0) = 0$. The initial condition $\theta(0)$ are set by the experimental condition. For superradiance, the state is prepared

in the superposition state relative to the tipping angle $\theta(0) = \pi/2$. For superfluorescence the atoms are fully inverted and $\theta(0) = 0$. This semi-classical description does not allow any evolution of the tipping angle according to Eq. 3.25, predicting a stationary solution in the unstable state $\theta(t) = 0$. Actually, MD formation is triggered by the spontaneous emission which cannot be explained in semi-classical framework. The quantum flutuations which initiate the Bloch vector inversion can be simulated in the model by taking $\theta(0) = 2/\sqrt{N}$ [81]. This trick however removes the stochastic nature of the dynamics associated to a quantum pendulum starting in its unstable position.

We can analyze the solution of Eq. 3.25 for different values of the product $k\tau_c$, whose physical meaning can be understood by recalling that k is related to the photons escape rate from the edge of the pencil-shape volume and that τ_c expresses the coupling between the atoms and the radiation field.

- **Case 1** : $k\tau_c \gg 1$. Pure SF.

  The emitted photons are weakly interacting with the atoms and are not trapped inside the active volume by reabsorption. Stimulated emission is also negligible so that a superradiant pulse proportional to N^2 completely drives the atoms to the groundstate where they will remain as absorption is negligible. If we recall the Bloch sphere representation, in this case the Bloch vector is forced to swing down to the south pole without exhibiting any oscillation. The term $\ddot{\theta}$ is thus dropped and the solution of Eq. 3.25 and Eq. 3.24 are given by:

  $$\theta = -\tanh\left(\frac{t-\tau_d}{\tau_R}\right) \qquad I(t) \propto \operatorname{sech}^2\left(\frac{t-\tau_d}{2\tau_R}\right) \tag{3.26}$$

  where τ_d indicates the delay time of the SF/SR pulse peak with respect to the initial instant $t = 0$. It depends on the initial conditions. For the superradiance ($\theta = \pi/2$) the delay time is zero. As soon as the system is prepared into the superposition of the excited and ground states $|N/2, 0\rangle$, it immediately starts to irradiate at the maximum intensity as plotted in Fig. 3.3. For SF we have $\theta(0) = 2/\sqrt{N}$ and the delay time assumes the value $\tau_d \approx (\tau_R/2)\ln(2N)$, necessary to the randomly oriented dipole to align and synchronize. During this time interval the number of cooperative atoms increases exponentially, but it is only in the part that the number is so large to fully deplete the inverted population via SF. The time-dependent inverted population and emitted intensity for pure SF and SR are plotted in Fig. 3.3.

- **Case 2** : $k\tau_c \approx 1$. Oscillatory SF.

  Stimulated and cooperative emission are comparable. The photon pulses are partially absorbed and then re-emitted. The Bloch vector approaches the stable south pole by performing several oscillations before stopping. Eq. 3.23

must be fully considered and the numerical solution of the time-intensity profile is a pulse train with decreasing amplitude, that is proportional to N^2. The pulses that follow one another display increasing width and delay. In Fig. 3.3 $\cos(\theta)$ and $I(t)$ for $k\tau_c = 0.1$ are plotted.

- **Case 3** : $k\tau_c \ll 1$. No damping.

  Stimulated emission and the re-absorption are the dominant processes. Superfluorescence has disappeared and the energy of the system is trapped inside the active volume for a long time because it is being exchanged in a reversible way between the atoms and radiation field. The atoms behave as if they were in a cavity. The emission intensity is composed of a pulse train whose amplitude is linear with the number of involved atoms. The pulses width equals τ_c, as well as their separation.

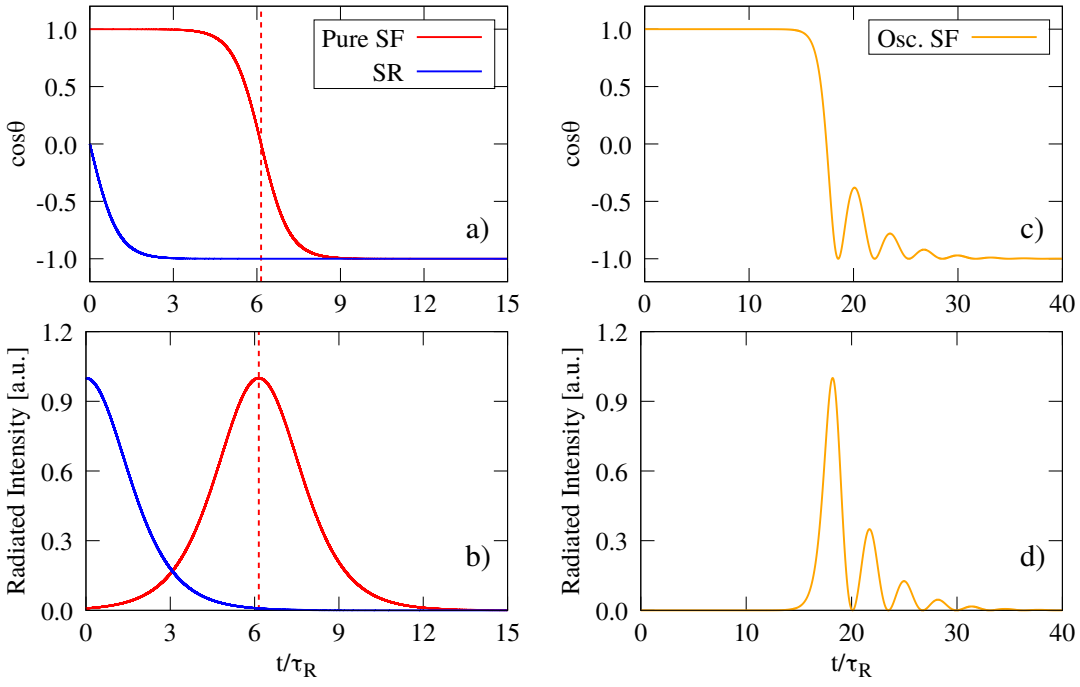

FIGURE 3.3: a) Tipping angle vs time expressed in SF time units for pure SF/SR, and b) oscillatory SF. c) Radiated intensity vs SF time units for pure SF and SR, and d) oscillatory SF. The curves for the Oscillatory SF are obtained by numerically solving Eq. 3.25 for $k\tau_c = 0.1$ and $\theta = 2 \cdot 10^{-6}$. The dotted line indicates the peak intensity.

For simplicity in this analysis the dephasing processes have been neglected. The authors have pointed out [76] that if T_2^* is considered in the model, the SF pulses are broader and their intensity is smaller. If the phase is not conserved during the MD formation, the atoms emit independently. This result can be inferred by the third equation of 3.21, in which the term of collective emission is suppressed for large T_2^*.

3.3.4 The Eberly and Rehler model

Eberly and Rehler [75] introduced a consistent model for SF in which the condition $V \ll \lambda^3$ is removed. Their results are important as they provide the correction factor in the τ_R and τ_d expressions, which is due to the finite size of the medium.

In response to an excitation with a quasi-monochromatic pumping pulse, the dipoles have different time origins due to the retarded time. Each dipole is thus characterized by phase $e^{-\mathrm{k_0 \cdot r_i}}$, where $\mathrm{k_0}$ is the wave vector of the excitation field and $\mathrm{r_i}$ is the dipole position. The dipole interference of terms with different phases affects the MD amplitude and the radiated intensity in Eq. 3.17 must be corrected as follows:

$$I(\mathbf{k},t) = I(\mathbf{k},0)\left(N\left\langle \mathbf{J}_{+,i}\mathbf{J}_{-,i}\right\rangle + N^2\left|\frac{1}{N}\sum e^{i(\mathbf{k}-\mathbf{k_0})\cdot r_i} - \frac{1}{N}\right|\left\langle \mathbf{J}_{+,i}\mathbf{J}_{-,j\neq\ i}\right\rangle\right) \tag{3.27}$$

Note that this approach includes the description of the SF radiation pattern. Furthermore, a time-dependent dipole dephasing due to the inhomogeneous broadening can be included provided the atomic frequency distribution is known. Here, μ is defined as the parameter that embodies interference effects arising from the finite size and shape of the collection of emitters

$$\mu = \frac{\int I(\mathbf{k},0)\left|\frac{1}{N}\sum e^{i(\mathbf{k}-\mathbf{k_0})\cdot r_i} - \frac{1}{N}\right| d\Omega}{\int I(\mathbf{k},0) d\Omega} \tag{3.28}$$

where $d\Omega$ is the solid angle element and the integral is performed over 4π. Now, the integrated cooperative emission intensity can be calculated with the same method used in the Dicke model, and we obtain the expression:

$$I(t) = \frac{\hbar\omega_0}{4\mu\tau_0}(N\mu+1)^2 \mathrm{sech}^2\left(\frac{t-\tau_d}{2\tau_R}\right) \approx \frac{\hbar\omega_0}{4\tau_0}\mu N^2 \mathrm{sech}^2\left(\frac{t-\tau_d}{2\tau_R}\right). \tag{3.29}$$

The validity of the approximation in the last step relies on the fact that $N\mu \gg 1$. For the time evolution expressed by Eq. 3.29, we have FWHM $\approx 3.52\,\tau_R$. This model gives the same expression for τ_R previously reported (see Eq. 3.19), but also provides a way to calculate the μ parameter. The expression in Eq. 3.16 for the delay time is replaced by:

$$\tau_d = \tau_0 \frac{\ln(N\mu)}{N\mu} = \tau_R \ln(N\mu) \tag{3.30}$$

For a pencil-shaped sample, the factor μ has been calculated [82] to be

$$\mu = 8\pi S/3\lambda_0^2 \tag{3.31}$$

and the SR/SF times assume the form:

$$\tau_R = \frac{\tau_0}{\mu N} = \frac{8\pi S}{3N\lambda_0^2}\tau_0 \tag{3.32}$$

Superradiance pattern

Eq. 3.28 accurately describes the superradiant radial intensity and its calculation for an arbitrary atom distribution is complex. For a long cylindrical medium the superradiant emission is highly directional with different possible emission patterns that can be classified according to a geometrical factor called Fresnel number:

$$F = \frac{S}{L\lambda_0}. \tag{3.33}$$

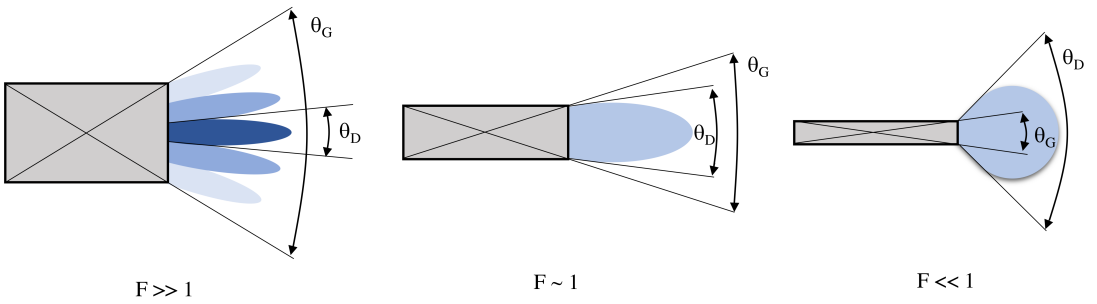

FIGURE 3.4: SF emission pattern for different F values.

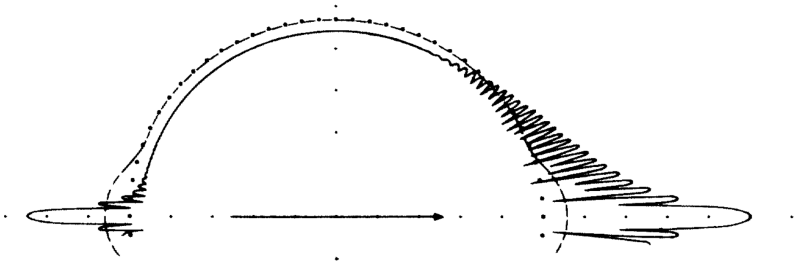

FIGURE 3.5: Superradiance radiation pattern radiated by two pencil shape medium with Fresnel number 500 and excited atom density of 61. The intensity is normalized to the incoherent emission intensity and to the number of atoms. The scale is radially logarithmic and each dot along the coordinate axes indicates an order of magnitude. The broken line is referred to a volume $V = 10\lambda^3/(8\pi^2)$ and the solid line to $V = 10^5\lambda^3/(8\pi^2)$. The arrow indicates the direction of the laser direction propagation, that is parallel to the cylinder axis. The figure is taken from Ref. 75.

For $F \gg 1$ the emission is contained within the geometrical angle $\theta_G = 2w/L$, with w the radius of the cylinder. However, several modes ($\sim F^2$) with a diffraction angle $\theta_D = \lambda/2w$ are sustained, each of them supporting a independent SR/SF process. For $F \ll 1$ there is only one diffraction mode with $\theta_D \gg \theta_G$. The condition $F \sim 1$ ensures a pattern emission characterized by one diffraction mode with $\theta_D \approx \theta_G$. The different patterns are depicted in Fig. 3.4 whereas in Fig. 3.5 we show the emission pattern for $F = 500$ as reported by Eberly and Rehler [75].

3.4 Conditions for SF observation

In the previous section, it has been discussed how a crucial condition for MD formation is $\tau_r, \tau_d \ll T_2, T_2^*$. From this relation and Eq. 3.32, we derive the minimum number of cooperative atoms that are needed for the SF occurrence:

$$N_t = \frac{8\pi S}{3T_2\lambda_0^2}\tau_0 \tag{3.34}$$

It is thus clear that a high inverted population is required. However, it is necessary to take into account that the spatial estention of the cooperative ensemble cannot be arbitrarily large. The limit is set by photon escape time $\tau_E = L/c = k^{-1}$, which must be shorter than the characteristic SR/SF decay time. When all the inverted atoms of the pencil-shaped volume emit cooperatively, τ_R is minimum and its value coincides with the cooperation time τ_c defined by Eq. 3.22. The following chain of inequalities must thus be fulfilled:

$$\tau_E < \tau_c < \tau_R < \tau_d < T_2,\, T_2^* \tag{3.35}$$

It is worth noticing that the condition $k\tau_c \leq 1$ reported in section Sec. 3.3.1 is equivalent to $\tau_E < \tau_c$, and for the limit case $k\tau_c \approx 1$ of oscillatory SF we have $\tau_R \to \tau_c$.

In long active media it may be that the condition $\tau_E > \tau_R$ is satisfied only in fractions of the excited volume, and the emitted light pulses are thus the envelope of several uncorrelated SF pulses generated in different regions of the sample.

Chapter 4

A review of Superfluorescence experiments

In this chapter we present the experimental SF achievements in several physical systems in the attempt to give a practical understanding of the SF phenomenon. The cooperative emission can be mistaken for with simple lasing effects and it is thus of importance to devise useful criteria for an unambiguous identification of SF. We list them in Sec. 4.1 and describe experiments in which coherent pulses can be rigorously attributed to SF in Sec. 4.2. We analyze a few works that stand as a reference in the field, whereby we learn that stringent conditions are set to realize a single coherent MD. In the last part we treat the case of RE-doped crystals, where we analyze two experiments in which SF is claimed, discussing in detail the evidences given by the authors.

4.1 Superfluorescence signatures

SF is fairly hard to obtain due to the presence of dephasing processes that hinder the MD formation. The models introduced in Chapter 3 predict the following SF signatures:

1. directionality of emitted radiation in pencil-shaped samples;
2. coherent photon bunches emission whose time evolution is well described by a squared hyperbolic function (Eq. 3.29). This implies that the pulses peak intensity depends quadratically on the pulses area ($\propto N$) and that their duration is inversely proportional to N;
3. retarded emission $\tau_d \propto N^{-1}$.

SR and SF share the same decay time evolution but the former immediately starts after excitation. In addition, SR can only be obtained through a superposition of states prepared by external coherent sources, such as one o more finely tuned laser pulses. It is important to remark here that SR, SF and lasing effect are sometimes improperly use in the literature. In other cases, it just a question of terminology, for instance, when authors use SR to mean SF and others even refer to lasing effect as Superfluorescence.

4.1.1 Amplified spontaneous emission

A phenomenon that takes place in media with high inverted population is the amplified spontaneous emission (ASE). ASE gives rise to coherent photon bunches that can be erroneously attributed to SF due to their temporal profile and directionality.

The luminescence from spontaneous emission is amplified by the stimulated emission process as it propagates through the active medium, and the pencil-shaped geometry determines a strongly directional emission as the highest gain occurs along the cylinder axis. ASE can be thus regarded as a lasing effect without the feedback mechanism provided by mirrors. Even though it might be regarded as a collective process, whereby a large number of atoms contribute to photon bunches formation, ASE is not a cooperative emission as no macroscopic dipole is built.

The first theoretical description including both ASE and SF processes was proposed by Polder and Schuurmans [81, 83] in 1979. According to their model the following condition for SF observation is set:

$$T_2 \gg \sqrt{\tau_R \tau_d}. \tag{4.1}$$

For $\tau_R < T_2 < \sqrt{\tau_R \tau_d}$ the leading process is instead ASE.

Due to the N^2 dependence of the cooperative emission, the SF time averaged intensity above threshold N_t has a quadratic dependence on the squared inverted population (to the 4 power for two photon excitation), whereas a linear relation is usually obtained for the ASE intensity. However also a quadratic dependence has been reported [84]. In these cases, a measure or estimation of T_2 compared to the SF pulse duration is thus a good way to identify the process since generally $\tau_d \sim (5 - 30)\, \tau_R$.

In conclusion, the stronger demonstration of SF occurrence are the manifestation of a delay time which should scale as $\sim N^{-1}$, the dependence of the peak intensity on N^2 or equivalently the relation $\tau_R \propto N^{-1}$.

4.2 Superfluorescence in different physical systems

A selection of experiments concerning cooperative emissions is given in Ref. [74], mostly devoted to nanostructured materials. An updated, comprehensive review of SF experiments is lacking in the literature. To understand the relevance of the findings presented in this thesis, it is important to make a critical review of reported SF observations according to the criteria listed in the previous section. In Tab. 4.1 we resume the results from experiments conducted in different physical systems including gases, atomic beams, solid-state systems and optically trapped atoms.

To accomplish population inversion a pulsed laser is mostly used. In these cases the SF pulse delay can be measured. The laser pulse duration must be shorter than τ_d, which in turn is shorter than the dephasing time T_2. The choice of laser system is thus done accordingly to the specific physical system. For instance, femtosecond Ti:Sapphire and free electron lasers (FEL) allow for investigating solid-state materials and high pressure gases, where the coherence time is short (ps). Such short intense pump radiation can be also used to produce a large inverted population through two photon absorption process, which ensures an incoherent excitation.

As one can deduce by inspecting Tab. 4.1, in gases there are higher chances to experimentally accomplish SF.

4.2.1 Gaseous system

Gases have narrow linewidths as the inhomogeneous broadening is mainly due to the Doppler effect. The homogeneous broadening is directly related to the collision time and thus T_2 and T_2^* can be estimated if the gas pressure and the temperature are known. At few mBar pressure and at room temperature, a coherence time in the order of nanoseconds is expected and nanoseconds-long duration SF is reported in many gases under these experimental conditions. Another advantage of gases is that the N^2-dependence of the SF pulse intensity can be investigated by increasing both the laser excitation and the gas density.

TABLE 4.1: Superfluorescence observation in physical systems.

System	λ_p [nm] [a]	λ_0 [nm]	τ_0 [ns]	τ_R [ns]	τ_d [ns]	Ref
Gases: vibrational level						
NH_3	10.9 μm	291 μm	-	<30	200	[85]
CH_3F	9.55 μm	496 μm	230 s	5 - 50	15 - 400	[86]
HF	2.5 μm	50 - 250 μm	∼1 s	50 - 300	0.6 - 1.5 μs	[87]
Gases and Atomic beam: electronic level						
He	52.2, 53.7	501.6	1.7	0.01 - 0.08	0.01 - 0.40	[88]
	52.2, 53.7	668	15.6	0.04 - 0.15	0.15 - 0.60	[89]
He^+	24.3	164, 469	-	∼ ps	<0.1	[90]
Xe^{2+}	17, 13.5	109, 68, 65	-	14 - 57 ps	0.16 - 0.36	[91]
Eu	346 - 348	633 - 736	26, 66	∼10	<8	[92]
	459 + 653	545, 557	50	2 - 10	5 - 13	[93]
	459 + 640	605.7	-	∼1	0 - 4	[94]
Tl	379.1	1301	-	∼1 - 2	12	[95]
Te_2	587 - 588	589.4, 590.0	50	3 - 17	58 - 63	[96, 97]
S_2	337.1	370 - 490	36	3 - 12	-	[98]
Na	589+616	3.41 μm	-	< 2	2 - 7	[99]
	330.2	2.21 μm	-	1 - 4	2 - 4	[100]
Bi	465.6	965.7	25	<2.5	7	[101]
Cs	455	2.9 μm	70	0.1 - 1.8	5 - 35	[102, 103]
Rb	420.1 - 421.5	2.3 - 2.8 μm	-	<2	10 - 58	[104, 105]
	780+776	5.2 μm	690	∼1 ps	4.5 ps	[106]
Ga	287, 294	5.75 μm	-	< 2	∼ 5	[107]
Ca	422.7	5.5 μm	4.6	∼1	10 - 50	[108, 109]
	422.7	1.9 μm	2.9 μs	-	30 - 100	[108]
Sr	∼460+655	655	-	0.5 - 3	1 - 4	[110]
Li	734.6	812.6	30	50 ps	-	[111]
Optical traps						
^{87}Sr	689 + 461	698	150 s	10 - 40 ms	0.1 - 0.25 s	[112]
Ca	432 + 429	657	420 μs	3 - 11 μs	60 - 100 μs	[113]
Solid-state system: bulk						
$C_{16}H_{10}$:$C_{12}H_{10}$	355	374	110	5 - 6	9	[114, 115]
BP1T [b]	397	461	-	4 - 28 ps	10 - 50 ps	[116]
O_2^-:KCl	266, 290	593 - 714	92	0.1 - 1.7	0.5 - 10	[117–120]
O_2^-:KBr	266	685, 733	-	<1	0 - 1.2	[121]
In:CdZnTe	600	788	-	20 - 30 ps	43 ps	[122]
ZnTe	390	530 - 540	1.2	0.3 - 1.5 ps	10 - 40 ps	[123]
NV:Diamond	3.2 GHz	3.2 GHz	$> 10^4$ s	35 - 140	275 - 350	[124]
Solid-state system: nano-structure						
CuCl:NaCl	389	391	-	<1 ps	6.3 - 8.7 ps	[125]
$In_{0.2}Ga_{0.8}As$	850 - 930	907	∼2	∼10 ps	80 - 230 ps	[126, 127]
$CsPbBr_3$	UV	539	400 ps	10 - 60 ps	0 - 3 ps	[128]

[a] Excitation wavelength.
[b] 2,5 0 -bis(4-biphenylyl)-thiophene (BP1T) co-oligomer singlecrystal.

SF in CH_3F

The first SF observation was made in HF gas at a pressure of (1-10) mTorr in 1973 [87]. Population inversion between the vibrational state $v = 0$ and a rotational level of the vibrational level $v = 1$ was accomplished by intense 2.5 μm-wavelength, 200-400 ns-duration laser pulses. In these experiments, both the oscillating and the pure SF have been observed for 5 lines in the far infrared range.

Forward and backward SF by vibrational levels at 491 μm was accomplished in CH_3F gases pumping with a CO_2 laser. The recorded time profile of the emitted pulse is shown in Fig 4.1, where some results of the investigation conducted with four different length gas cells (between 168 cm and 1021 cm) are also reported. In this case an impressive enhancement of the radiated intensity has been achieved. In fact, the spontaneous lifetime is reduced from 230 s to tens of nanoseconds thereby accelerating the decay rate by a factor $\sim 10^{10}$. The measured delay times, the dependence on excitation of the pulse width and of SF output intensity follow accurately the theoretical predictions for the 651 cm-long cell (Fig 4.1d). The negative intercept of the delay time to 0 is attributed to the finite laser pulse width.

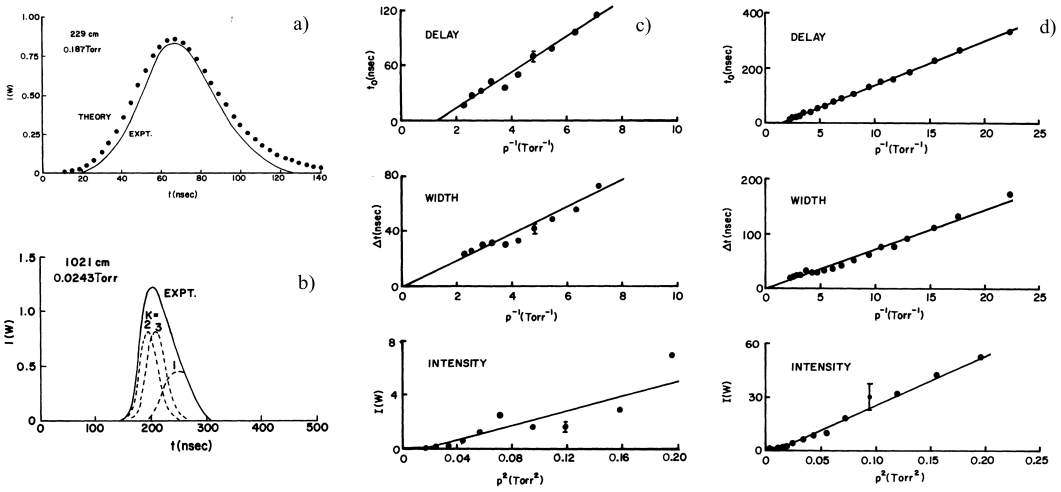

FIGURE 4.1: Comparison of the experimental (line) and calculated (dots) time profile of a SF pulse in CH_3F (a). Semi-classical fit (broken lines) to the observed pulse (solid line). Three independence SF pulses are necessary to generate the observed one (b). Delay times, pulse width and SF intensity as function of the laser intensity for the 229 cm (c) and 651 cm (d) gas cell. The figures are taken from Ref. 86.

For the other gas cells, the results are only roughly consistent with the expectation dependence (Fig. 4.1c) and the authors ascribe this discrepancy to the interaction between the three vibrational modes of the molecule. In some cases the superimposition of two or three independent SF pulses was observed and the resultant signal is smooth and asymmetric as shown in Fig. 4.1b. Actually, the CH_3F molecule has

different emission wavelengths corresponding to different vibrational modes. The three independent SF pulses related to the three modes have comparable delay times τ_d and are thus superimposed. Furthermore, values of the initial tipping angle display a better agreement with $N^{-1/2}$ rather than $(\mu N)^{-1/2}$. The polarization dependence and the ratio between the backward and forward emission have not been fully explained.

In conclusion, the CH_3F experiment shows how difficult it is to embrace all the aspects of SF. Even though the CH_3F molecule spectroscopic properties are well known and the main SF signatures have been obtained, there are several other observables that are beyond our understanding.

SF in Na

The largest number of SF experiments reported in Tab. 4.1 are related to emission from electronic levels of gases. They have much shorter lifetime that of the vibrational levels, therefore a lower number of cooperative atoms/molecules are required to fulfill $\tau_R < \tau_d$. The example we briefly discuss here is that of Na vapors [99]. The energy levels and pumping scheme is shown in Fig. 4.2a. Two counter propa-

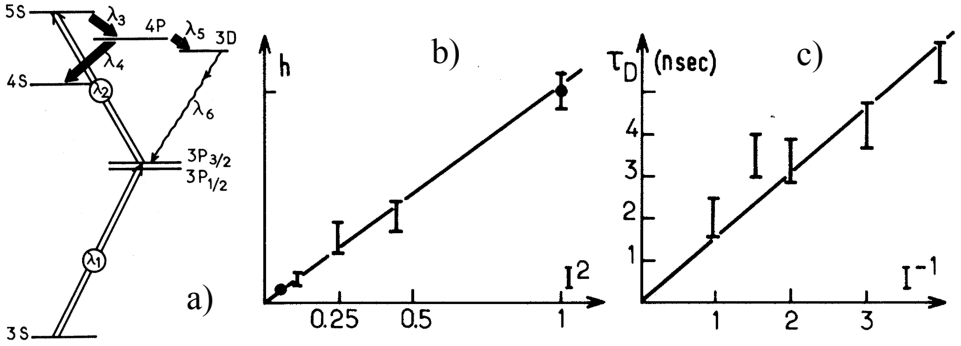

FIGURE 4.2: SF in Na vapors. a) Energy level scheme of Na atoms. Double-line arrows are the pumping transitions at $\lambda_1 = 589\,\text{nm}$ and $\lambda_2 = 616\,\text{nm}$. Solid-line arrows indicate superradiant transitions at $\lambda_3 = 3.41\,\mu\text{m}$ and the cascaded $\lambda_4 = 2.21\,\mu\text{m}$ and $\lambda_5 = 9.10\,\mu\text{m}$. The wavy line is the transition $\lambda_6 = 819\,\text{nm}$ is detected off-axis by a photomultiplier. b) Peak intensity h and c) delay time for $3.41\,\mu\text{m}$ wavelength SF pulses vs laser intensity. The figures are taken from Ref. 99.

gating lasers are used to excite the Na atoms in a 14 cm-long cell. SF along with two subsequent transitions are observed above threshold at $3.41\,\mu\text{m}$, at $2.21\,\mu\text{m}$ and $9.10\,\mu\text{m}$-wavelength, respectively. The delay time and pulse width show the expected dependence on excitation intensity (Fig. 4.2b,c), as long as the inverted population is not too high. In fact, for strongest excitation, the delay time is so short that the emitted pulse overlaps the lasers pulse, thereby preventing the MD

formation and favoring the onset of ASE. Collective process characterizes also the other two cascading transitions at 2.21 μm and 9.10 μm (Fig. 4.2a).

We mention that SF has been recently accomplished from very high energetic level (tens of eV) of noble gases at a pressure of several Bar (up to 30 Bar) using FEL excitation and SF pulse widths in picoseconds range has been obtained.

SF in optically trapped ^{87}Sr

SF has been reported in optically trapped ^{87}Sr atoms cooled at 10 μK [112]. The number of involved atoms is limited to $2.5{\cdot}10^5$ but the confinement in a magic-wavelength optical lattice within a finesse optical cavity endows the atoms of extremely long coherence times, in the order of milliseconds. All fingerprints of a formation of a single MD was identified (Fig. 4.3). This case is of particular interest because the SF level of ^{87}Sr has a lifetime of 150 s which corresponds to a linewidth of few mHz. In the effort to achieve a steady-state SR, namely a situation in which the MD is continuously filled with other atoms and permanently irradiate, a extremely narrow linewidth laser can be accomplished. Actually, the SF/SR linewidth limitation that is determined by the SR/SF pulse width is overcome if the steady-state condition is established.

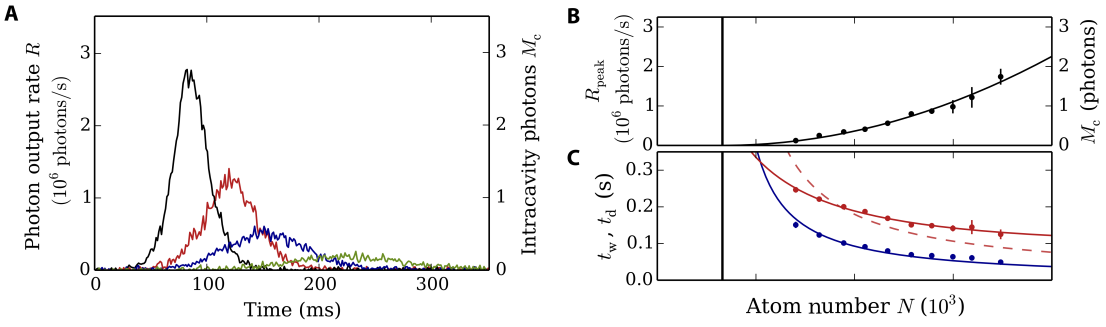

FIGURE 4.3: Superfluorescence from ^{87}Sr atoms trapped within a high-finesse optical cavity. A) Representative single time traces of photon output rate and equivalent average intracavity photon number. B) Peak photon output rate versus initial total atom number. The black line is a quadratic fit to the output power. An horizontal offset in the fit is introduced to take into account the decoherence and atom loss. C) FWHM pulse duration t_w (blue) and delay of peak power t_d (red) versus initial total atom number. The figures are taken from Ref. 112.

4.2.2 Solid-state systems

In solids the interaction between the optical centers are much more strong as compared to gases and the condition of identical emitters is much more difficult to

satisfy. At room temperature the coherence time is as short as tens of picoseconds due to phonon scattering, and SF is observed only in Lead Halide Perovskite ($CsPbBr_3$) quantum dot superlattices excited by a 100-200 fs pulse of a Ti:Sapphire laser via two photon absorption process. The SF pulses and the related parameters dependence on the laser excitation density are shown in Fig. 4.4. The fluctuation that characterize the signal amplitude above threshold is due to the strong atom-light interaction and is known as Burnham-Chiao ringing [129].

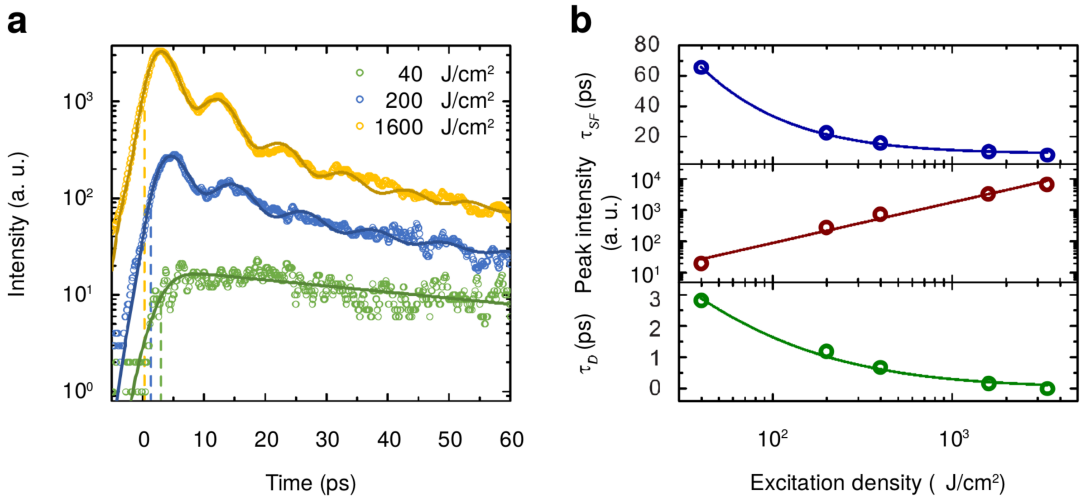

FIGURE 4.4: SF in $CsPbBr_3$ at room temperature. (a) Time-resolved emission intensity traces for three different excitation powers. (b) SF decay (blue circles), peak SF emission intensity (red circles) and extracted delay time (green circles) as a function of the excitation power density fitted according to the SF model. Power-law dependence of the peak intensity with an exponent equal to 1.3 ± 0.1 is attributed by the authors to saturation effects. The figures are taken from Ref. 128.

Even at lower temperatures SF occurs in a limited number of solid-state systems such as CuCl nanocrystals embedded in a NaCl matrix, InGaAs quantum well, and some select semiconductors. Two compounds are of particular importance to the present work: diphenyl crystals containing pyrene and O_2^- center in halides crystals (KCl, NaCl, KBr) since such materials exhibit nanoseconds-long coherence time at 4 K.

SF in O_2^-:KCl

The energy level scheme of O_2^-:KCl and the schematic representation of the experimental apparatus are shown in Fig 4.5a,b. Florian et al pumped the crystal at 4.2 K with a mode-locked Nd:YAG laser (266 nm) and observed the SF line both at 592.8 and 629.1 nm. The SF pulses shape (Fig. 4.5c) is asymmetric and it is probably due to the superposition of independent SF pulses arising from different

O_2^- subensembles where $T_2^* \gg \tau_R$ is satisfied. In fact, the emission linewidth is $2\,\mathrm{cm}^{-1}$ and the associated $T_2^* = 5\,\mathrm{ps}$ is much more shorter than τ_R.

In such physical system much work has also been devoted to the demonstration of the stochastic nature of the SF effect. The fluctuation of the peak intensity and the histograms of delay time of the SF pulses recorded with identical excitation pulses are shown in Fig. 4.5d,e.

The peak intensity and the delay time of the SF pulses were recorded with identical excitation pulses (Fig 4.5d,e). Their relation is qualitatively in agreement with theoretical expectation but it is interesting to note the peak intensity fluctuations and the time delay distribution, which result from the stochastic nature of SF.

The transition from SF to ASE was observed for the first time in O_2^-:KCl [130] and confirmed the previously mentioned Schuurman and Polder model (see Sec 3.4). As the temperature is increased from 10 K to 22 K, the delay time varies from 160 ps to 800 ps as the decreasing coherence time reduces the cooperative atom number. For higher temperature, τ_d decreases until it disappears at 30 K due the dominant occurrence of ASE.

We have here discussed SF observations in optical transitions. Although SR has been deeply investigated also in other energy ranges for the FEL realization [131] and NMR application [73], SF has not been reported to the best of our knowledge in the systems related to these fields, with the exception of the negatively charged nitrogen vacancies in diamond [124] at 25 mK. In such materials, the coherence of the vacancies is longer than 1 μs and the inverted spin has a very long radiative lifetime. The SF is accomplished by placing the sample in a three dimensional resonator with a quality factor $Q = 230$ and by involving in the coupling the impressive number of 10^{16} spins. The decay rate is in this way accelerated by trillion times. In this type of cavity QED experiments, the microwave cavity resonator strongly enhances the spontaneous emission rate and thus the cooperative processes.

4.2.3 Comments

The dephasing time limits the optical SF pulse duration and the large MD lifetimes to the nanoseconds range in most of cases. Longer times are achieved in optically traps atoms but only for mesoscopic ensembles. If we are interested in studying cooperative processes, such as cooperative Raman scattering [73], the number of coupled atoms N is the other important factor as their rate scales with N^2.

This amount is rarely reported although it can be estimated by measuring the number of photon of the relative recorded pulse, provided that it is not composed

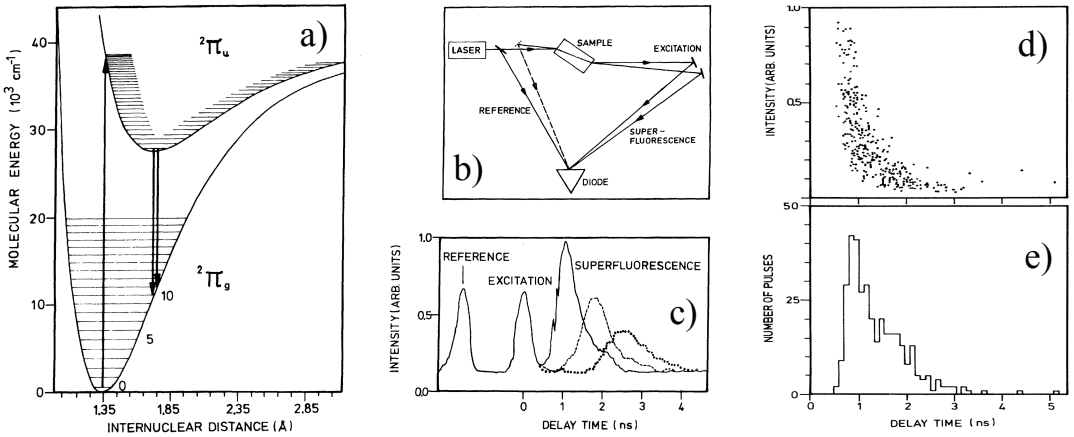

FIGURE 4.5: SF in O_2^-:KCl crystals. a) Energy level and pumping scheme of O_2^- molecules in KCl. b) Experimental setup for measuring intensities and delay times of the SF pulses. c) Example of the forward Superfluorescence in three independent shots at identical excitation conditions. d) Intensity of the Superfluorescence pulse as a function of the delay time. e) Probability density of the observed delay times. The figures are taken from Ref. 120.

by independent SF bunches. Another way is to considering the accelerating parameter τ_0/τ_R which is equal to μN (3.32). We must point out that this relation is not confirmed by any author that has investigated it. The highest τ_0/τ_R values for SF in optical range is as large as $\sim 10^5$ obtained for Rb atoms, where the maximum cooperation number was estimated to be $2 \cdot 10^9$. Much larger values should be obtained by considering vibrational level systems, where the SF lies in far infrared range. In CH_3F we have up to $\tau_0/\tau_R = 5 \cdot 10^{10}$ with an inverted population of $\sim 10^{15}$ and the emission at 491 μm. In [88] it was measured for a helium gas sample bunches of photon in the order of 10^{10}. Note that the cooperative atom number can be increased by considering longer medium only to some extent due to the condition $\tau_E < \tau_R$.

Finally, we stress that discrepancies of the theoretical dependences with the experimental observations are usually found during the experiments. This could have several explanations. For example the overlap of independent photons bunches, which could arise from inhomogeneously broadened ensemble or different regions of the medium, alters the time profile expressed in Eq. 3.32 and the estimation of the effectively N. Another reasons could be the neglecting of dephasing processes, the non homogeneity of the inverted medium and interactions between the atoms/molecules or atom-SF field.

4.3 Coherent emission in RE-doped crystals

Cooperative processes in RE-doped crystals are widely investigated in the field of quantum information [66] in view of their long coherent time. For instance, in the so-called photon echo technique, a retarded superradiant decay of RE ions takes place following two or more coherent excitation pulses as a consequence of spontaneous rephasing. Another example of cooperative process is the free induction decay, in which a laser pulse prepares the RE ions in a superposition of states and the coherent emission by the phased ions is observed as a tail of the coherent excitation pulse.

In such processes the ions coherence is induced by an external source while SF corresponds to the spontaneous formation of macroscopic coherent state. The aim of this section is to show that there are no unambiguous, clear demonstrations of SF in the literature. Here, we carefully analyze two different experiments in which the observed generation of coherent pulses was ascribed to SF.

4.3.1 $NdCl_3$ crystal

An intense, directional emission at 694 nm has been reported in a $NdCl_3$ single crystal following 10 ns pulse excitation at 355 nm wavelength. Experiments are performed in the (12-50) K temperature range. The natural level lifetime is 52 ns, whereas the photon bunches have durations shorter than the rise time of the used detector (∼ns). Examples of the recorded time profiles are shown in Fig. 4.6.

Two evidences are brought to support the SF emission claim:

1. the coherent emission intensity follows a square law versus pumping power;
2. the onset time of the emission becomes shorter as the pump power increases

We believe that (2) is not as strong as a clear, delayed emission signature. In fact, it might be also explained invoking the fact that the laser excites a level near resonance, which in turn exponentially relaxes towards the emitting level. In addition, we do not believe that the fundamental inequality $\tau_R \ll T_2^\star$ is fulfilled in this case, as the high density of Nd^{3+} ions increases the ion-ion interaction rate thereby strongly reducing the coherence time.

4.3.2 Er:YLF crystal

Auzel and co-authors [133, 134] attributed to SF the coherent and directional emission at 2.72 μm from Er^{3+} ions they observed in Er:YLF 1% crystal at (10-60) K

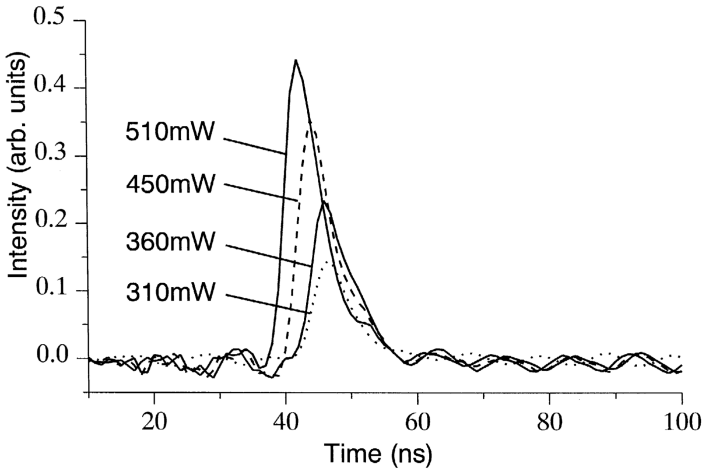

FIGURE 4.6: $NdCl_3$ emitted pulses. The figure is taken from Ref. 132.

(Fig. 4.7a). In this case, the population inversion is accomplished by a off resonant (647.0 nm) continuous wave Krypton ion laser via Stokes process. The arguments that they give are the following:

1. besides the steady-state, spontaneous incoherent emission (with decay time $\tau_0 = 4\,\text{ms}$), photon bunches with duration of about 150 ns are recorded (Fig. 4.7b,c). The $\tau_R < T_2$ is satisfied owing an assumed T_2 as long as $\sim 1\,\mu\text{s}$.

2. the directional emission intensity has a quadratic dependence on the laser excitation and hence on the inverted population (Fig. 4.7d).

3. the laser power threshold for the coherent pulse observation has a strong dependence on the temperature, that is strongly related with T_2.

4. the effect occurs also in samples as short as $100\,\mu\text{m}$ and concentration $\leq 1\%$, whereas ASE is far more likely in opposite condition.

In the reported experiments, the population inversion is accomplished by CW lasers, therefore one of the most important signatures, i.e. the delayed emission, cannot be obtained. In addition, the recorded optical pulses do not correspond to the true emission dynamics due to the finite response time of the HgCdTe photodiode used, comparable with the pulse duration. In addition, due to this instrumental limit, the time profiles cannot be carefully analysed.

Probably the coherence time of the Er^{3+} ions is a much shorter than the authors have assumed. The coherent pulses are recorded up to a temperature of 60 K, where a coherence time in the order of nanoseconds is expected. Such short time

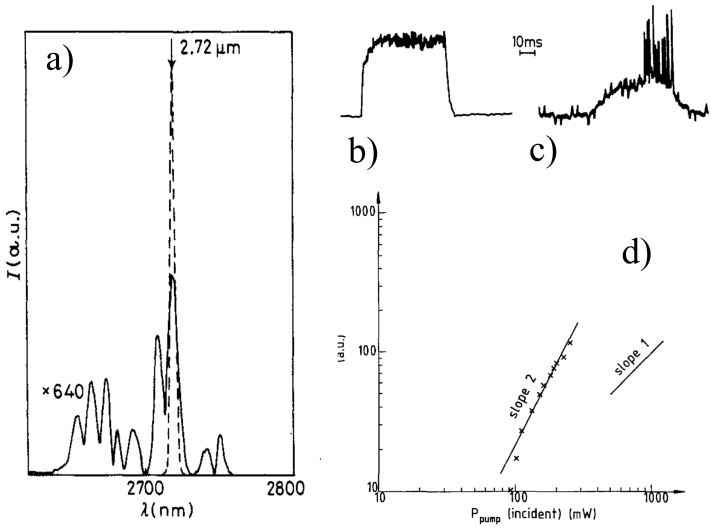

FIGURE 4.7: The solid line represents the ordinary isotropic emission spectrum due to $^4I_{11/2} \rightarrow {}^4I_{13/2}$ Erbium doped YLF transitions. The dotted line represents the coherent emission spectrum a). Temporal behavior of Er:YLF emission well above threshold b), at threshold showing the photon bunches along with the incoherent emission c). The laser beam is pulsed in order to show the threshold nature of the process. Directional coherent emission intensity as function of the laser incident power. The figure are taken from Ref. 133, 135.

reduces the probability of dominant SF, taking also into account that the transition from SF to ASE has been reported in O_2^-:KCl at $\sim 20\,K$.

We can draw the conclusion that Auzel and co-authors observations and considerations point to the occurrence of SF, but they cannot completely rule out ASE. While the occurrence of SF in the discussed experiments cannot be fully excluded, it is evident that to have just one of the required signatures is not sufficient for SF claim. These two experiments are thus not reported in Tab 4.1.

In the next chapter, we will bring clear signatures of pure, predominant SF decay in Er:YLF, taken at liquid helium temperature where Erbium ions have much longer coherence time. Moreover, our claim of cooperative emission process is based on an accurate, complex analysis of properly detected SF pulses.

Chapter 5

Superfluorescence: experimental results

In this chapter we present an experimental study regarding on the spontaneous formation of macroscopically extended coherence state in Erbium-doped YLF (1% and 0.01% concentration) and YSO (0.1% concentration) crystals. As mentioned in the first chapter, these crystals at low dopant concentration and cryogenic temperature exhibit coherence times of several microseconds, which can be extended up to few milliseconds when a strong static magnetic field is applied.

In the crystals investigated in this thesis the dipoles that can participate are Er^{3+} ions, whose level lifetime is in the milliseconds range, more than 10^6 times longer than the typical ones exploited in the other superfluorescent systems. This long lifetime allows us to produce a large inverted population through cw laser pumping. In addition, the narrow inhomogeneous linewidth limits the dephasing among the ion dipoles once the coherence is established.

Clear signatures of the macroscopic dipole formation in Er:YSO and Er:YLF are derived from a careful analysis of the pulsed emission. We have devised the following tests which include:

1. the spectral analysis of the pulsed emission (Sec. 5.1.1);
2. the investigation of the spatial profile and propagation of the forward beam (Sec. 5.1.2);
3. the analysis of the emitted pulses: time evolution and validation of the expected relationship between peak intensity, area, and duration (Sec. 5.1.3);
4. the study of the average intensity of the forward emission vs the population inversion (Sec. 5.1.4).

To rule out accidental lasing actions due to reflections on the crystal or cryostat windows surfaces, we verify that the observed SF emission is independent of the relative orientation of the sample with respect to the laser beam direction.

In Appendix, we show the results obtained with the Tm:LLF 12% crystal, in which the occurrence of ASE allows us to compare its features with that of SF from Er-doped crystal.

5.1 Superfluorescence in Er:YSO 0.1%

The crystal sample is immersed in superfluid Helium at 1.6 K (Fig. 5.1) and the Ti:Sapphire (II) laser beam is focused on the crystal sample to a beam waist $w = 163\,\mu$m, with a Rayleigh range much longer than the crystal length. The transmitted laser power is measured concurrently with the studies of SF properties by means of a dichroic mirror and bandpass filters. The excitation of the $^4I_{13/2}$ manifold is accomplished via multiphonon relaxation steps by tuning the pump laser to the lowest Stark levels of the $^4I_{15/2}$ and $^4I_{9/2}$ manifolds (see Fig. 5.1). The latter processes are very efficient and have a rate much higher than the $^4I_{13/2}$ decay rate, as we measure a lifetime of $\tau_0 = (15.0 \pm 0.1)$ ms. We thus assume that each absorbed laser photon leads to the excitation of one Er^{3+} ion to the lowest level of $^4I_{13/2}$ manifold. It is important to note that the multiphonon relaxation in the transitions $^4I_{9/2} \rightarrow {}^4I_{11/2}$ and $^4I_{11/2} \rightarrow {}^4I_{13/2}$ cancels any coherence degree among atoms induced by the coherent laser light. The $^4I_{13/2}(1)$ radiative de-excitation towards the eight Stark levels of the ground state $^4I_{15/2}$ manifold gives rise to eight emission lines in the range (1530-1670) nm as shown in Fig. 5.1 and Fig. 5.2. The absorption spectrum is shown in Fig. 2.7 of Chapter 2.

By increasing the laser intensity, SF appears above a threshold as a highly directional beam along the laser propagation direction[1]. The Fresnel number in the present configuration is $F = \pi w^2/L\lambda \approx 9$, therefore the observed diffraction pattern is mainly consisting of a single central lobe.

5.1.1 Spectral filtering

The emission spectrum recorded with the near-infrared spectrometer displays spectral filtering (Fig. 5.2), i.e. among the eight ordinary fluorescence lines only the one at 1545 nm-wavelength with the highest branching ratio $\beta = 42\,\%$ and related

[1] The laser and SF beam are in general not overlaid. This probably arises from the dependence of the diffraction on the field wavelength. Actually, the relative divergence angle can be tuned by varying the crystal orientation with respect of the incident laser direction and vice versa.

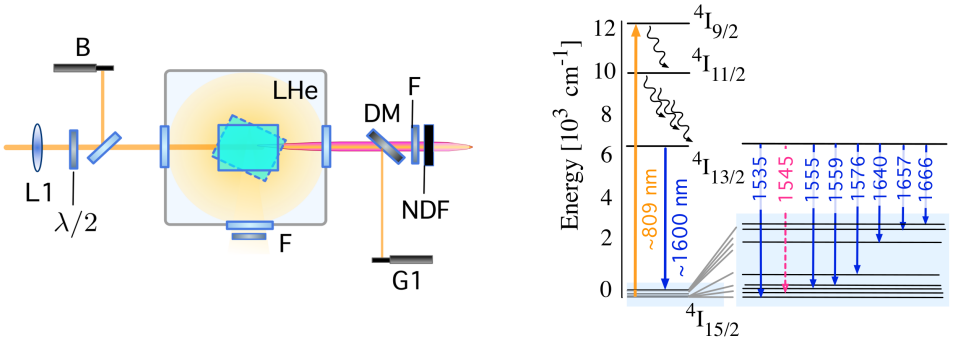

FIGURE 5.1: (Left) Experimental apparatus scheme. The sample is immersed in superfluid Helium. The Ti:Sapphire laser (II) is focused with the lens L1 and its polarization can be adjusted with the half-plate $\lambda/2$. The incident and transmitted laser power is measured by using the bolometers B and G1(left). The superfluorescence beam is filtered by the dichroic mirror DM and the bandpass filter F. Neutral density filters NDF are employed to reduce the SF intensity. (Right) Energy level scheme of Erbium ions. The laser excitation is represented by the orange arrow and the fluorescence transitions by blue arrows. SF transition is indicated by the magenta arrow.

time[2] $\bar{\tau}_0 = 36\,\text{ms}$ characterizes SF. We recall here that SF takes place above a pump threshold that is proportional to the inverse of the transition rate as discussed in Section 3.4. As we are pumping in cw, as soon as the required inverted population is attained, a MD emitting at 1545 nm is built, inhibiting the formation of MD oscillating at different wavelength.

SF at longer wavelengths, as for instance at 2.7 μm ($^4I_{11/2} \rightarrow {}^4I_{13/2}$), has not been observed from this crystal at a InAs detector[3] (Hamamatsu, P7163) combined with bandpass filters.

5.1.2 Propagation

The SF beam radius is measured at different distances from the crystal centre through the knife-edge technique (Fig. 5.3). At a fixed distance, a blade progressively covers the SF beam while its time averaged transmitted power is recorded by a Germanium-based bolometer. The obtained curve of the power as function of the knife position represent the cumulative distribution function of the spatial beam profile. As shown in the inset of Fig. 5.3, the acquired transmitted power

[2]With the term branching ratio we refer to the probability of the $^4I_{13/2}(1)$ of decaying towards a specific level, the $^4I_{15/2}(2)$ in this case. The related time of this transition is the inverse of the transition rate and it is calculated as $\bar{\tau}_0 = \tau_0/\beta$.

[3]The wavelength range is 1.0-3.1 μm.

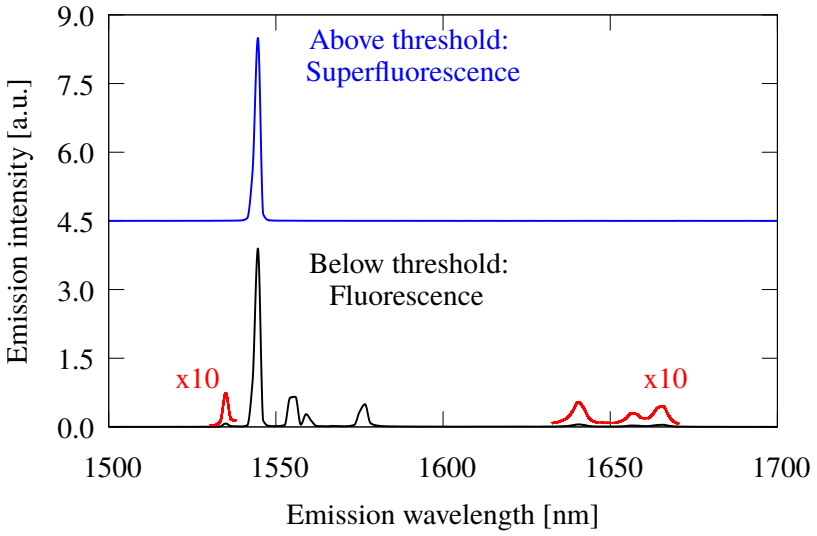

FIGURE 5.2: Ordinary emission spectrum (black line) of Er:YSO acquired by the NIR512 spectrometer. Superfluorescence spectrum (blue line) recorded with high laser intensity (above threshold). For clarity an offset has been added to the SF spectrum.

data follows the cumulative distribution function of a Gaussian beam profile:

$$P(x,z) = \frac{P_0}{2}\left[1 - \mathrm{erf}\left(\frac{x-c}{R(z)}\right)\right] \qquad \text{with} \qquad \mathrm{erf}(y) = \frac{2}{\sqrt{\pi}}\int_0^y e^{-t^2}dt \qquad (5.1)$$

in which P_0 is the time averaged incident power, z is the distance from the crystal edge, c accounts for the initial arbitrary position of the blade and R is the beam radius at the distance z. The measured divergence angle $\theta_d = \arctan(R/z) = (3.6 \pm 0.5)\,\mathrm{mrad}$ is in agreement with the expectation value for the diffraction angle $\theta_D \approx \lambda/2w = 4.7\,\mathrm{mrad}$. SF beam is thus characterized by a Gaussian profile which is inherited by the laser excitation.

It is worth noticing that such well-defined Gaussian propagation is a good condition for the design of a cavity which could improve the SF properties and could be exploited to test new cooperative processes.

5.1.3 Superfluorescent Pulses Analysis

The SF beam is first collimated and then focused to a beam waist of 186 μm (Focused data in inset of Fig. 5.3) at the InGaAs PD (II) position (1 mm^2-diameter), ensuring the full collection of the SF pulse energy. The emission is so intense that three neutral filters with a total transmittance of $2.3 \cdot 10^{-5}$ are employed to operate the PD far from saturation. Signals corresponding to single photon bunches are acquired at a 6 GHz digital sampling oscilloscope. The bunches rate depends on the excitation intensity and the average time separation of few microseconds

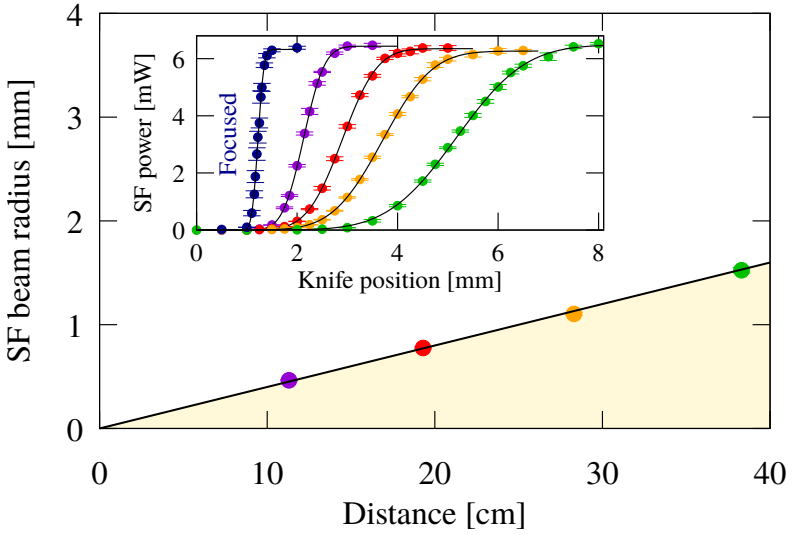

FIGURE 5.3: SF beam propagation. (inset) Measured SF beam power vs relative position of the knife edge at different distance from the crystal centre. The blue dots "focused" are recorded at the focus position of the SF beam when two lenses are introduced (See Sec. 5.1.3). The black lines are fits in the form given by Eq. 5.1. (Main figure) SF beam width vs distance from the crystal centre. The black line is a linear fit.

is observed for highest laser intensities. As shown for some representative pulses plotted in Fig. 5.4a, the recorded temporal profiles are well fitted by the quadratic hyperbolic secant function:

$$I(t) = P\text{sech}^2\left(\frac{t-t_0}{2\tau_R}\right) \tag{5.2}$$

with P the peak amplitude and t_0 is instrumental. The goodness of the fit indicates that each photon bunch is emitted by a single MD. An interesting aspect of our cw pumping scheme is the fact that the MDs are hardly superimposed as their threshold is accidentally attained in independent subensembles and the pulses rate is sufficiently low.

By taking into account the PD quantum efficiency, the neutral density filters attenuation, the overall loss due to other optical components, we are able to convert the measured area and peak intensity of each pulse into a number of emitted photons[4] $\bar{N}$ and peak emitted photon rate R_p, respectively. These two quantities, along with the fit parameter τ_R obtained for two laser fluencies[5], are plotted in Fig. 5.4b,d. We obtain bunches composed by $\approx 10^{12}$ photons and the radiative decay of the Er^{3+} ions is accelerated by a factor $\tau_0/\tau_R \approx 15\,\text{ms}/15\,\text{ns} = 10^6$. This

[4]For the moment we will assume that the number of observed photons per bunch $\bar{N}$ is equal to the number of correlated atoms N.

[5]We have analyzed signals also for $9.8{\cdot}10^{17}$ ph/s fluence. As these data are similar to those recorded for $6.5{\cdot}10^{17}$ ph/s, they are not shown.

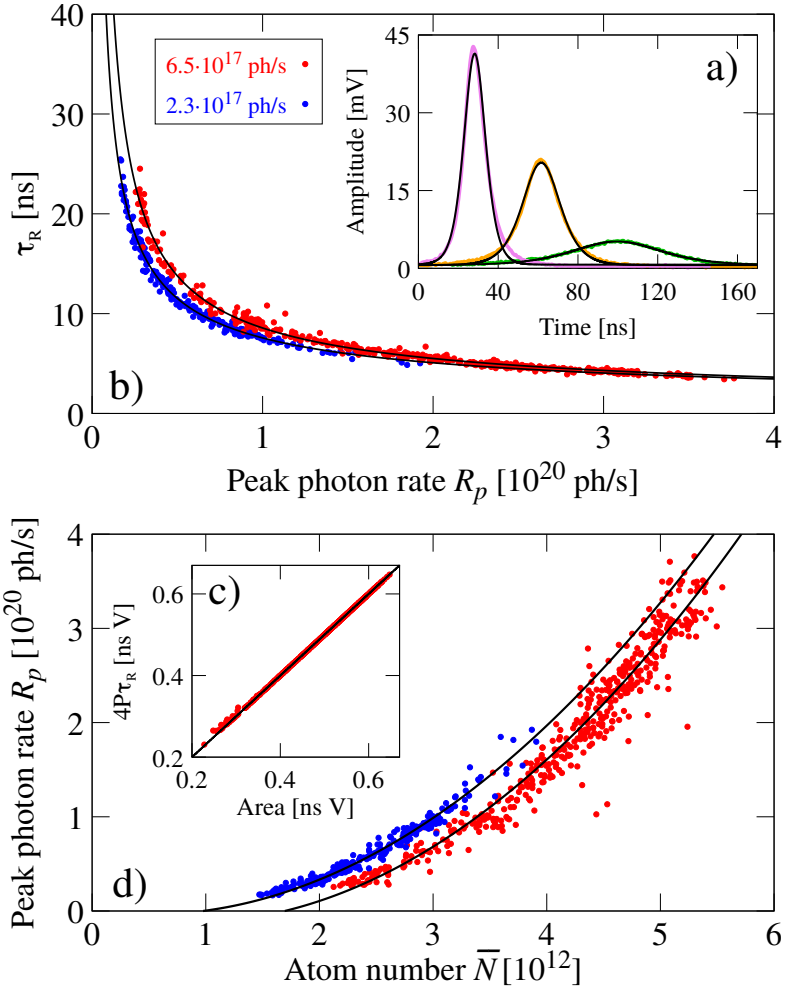

FIGURE 5.4: Spontaneously generated forward SF pulses for two different laser fluence values. a) Representative single time traces (purple, orange, green) of photon bunches recorded under identical excitation conditions. The black lines are obtained by fitting the data with Eq. 5.2 b) τ_R versus peak photon rate R_p. The black lines are fits in the form given by Eq. 5.5. (c) Product of the fit parameters versus integrated pulse area. Linear regression (black line) with unitary slope demonstrates pure SF dynamics for the recorded photon bunch. d) Peak photon rate versus observed photon number. The recorded data scale superlinearly, demonstrating the SF occurrence. The black line is obtained fitting the data with Eq. 5.5

parameter and the number of coupled atoms are at least two orders of magnitude larger than those observed in the systems reported in Chapter 4 for SF in visible-mid infrared range.

The characteristic time of the recorded SF pulses is comparable to the rise time of the PD, therefore we repeat the acquisition under the same experimental conditions by using an ultrafast PD (InGaAs, rise time 25 ps). The shortest recorded

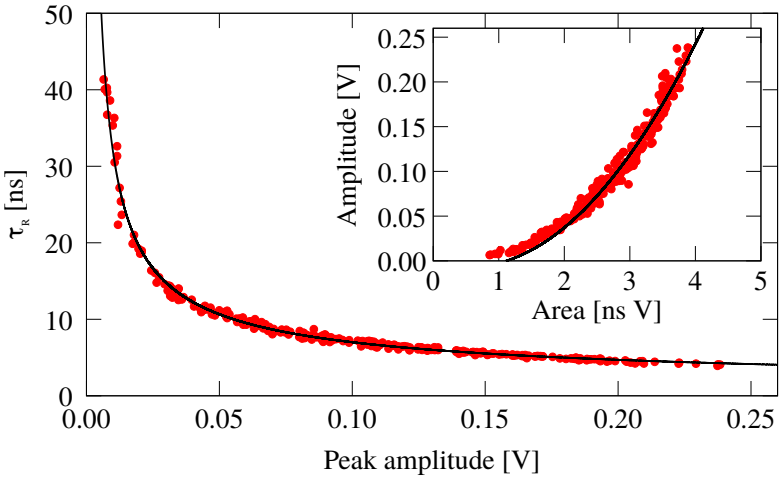

FIGURE 5.5: Spontaneously generated forward SF pulses recorded with 25 ps rise time PD. a) Peak photon rate versus observed photon number. The recorded data scale superlinearly, demonstrating the SF occurrence. The black line is obtained fitting with Eq. 5.5. b) τ_R versus peak amplitude P. The black lines are fit in the form given by Eq. 5.5 adding a scaling factor.

pulses have the same shape of those recorded with the larger area PD, ruling out distortions of the temporal dynamics in the signals diplayed in Fig 5.4.

On the other hand, due to its smallest area (10^{-3} mm^2), data recorded with this PD cannot be used to estimate $\bar{N}$. It is interesting to note that we obtain similar trends when plotting pulse peak P vs area and τ_R vs P with the two PD[6] (Fig. 5.5). The data shown in Fig. 5.5) demonstrate that there are no fluctuations of the emission direction of the pulses and that the spatial profile of a single pulse coincides with the profile measured with the knife-edge technique.

Since the pulse propagation is strictly related to the Er^{3+} dipoles distribution, it is reasonable to assume that the MD is extended on the whole inverted medium.

The gain correction

From Eq. 3.32 and Eq. 3.29 obtained for SF in a extended medium, we derive the following equations:

$$\tau_R = \sqrt{\frac{\bar{\tau}_0}{4\mu P}} \qquad \text{and} \qquad P = \frac{\mu N^2}{4\bar{\tau}_0} \tag{5.3}$$

[6]The different maximum value for the τ_R is determined by the minimum trigger level set to record the pulses. The presented data do not represent the correct density of photon bunches as the pulses are acquired above the trigger level, manually changed during a data set acquisition to obtain a uniform distribution of data amplitudes. The minimum τ_R is instead set by the experimental conditions.

Data in Fig. 5.4d display the expected quadratic dependence even though the parabolic curve intercepts x-axis at non-zero values. This shift is not attributed to any instrumental effects but can be explained if we assume that in our physical system the observed pulses are composed of photons emitted by the MD and by other ions that do not contribute to accelerate the decay. Due to the small inhomogeneneous linewidth and the large inverted population density ($\sim 10^{15}$ total excited ions in samples above threshold), it is possible that the MD radiation is amplified as it propagates along the crystal via stimulated emission.

Let us define α as the gain for unit length at the SF wavelength. The observed photons arise from N coupled ions and from $N\alpha L$ uncorrelated ions: $\bar{N} = N + N\alpha L = N + N_0$. By introducing $\bar{N}$, Eq. 3.32 and Eq. 3.29 are replaced by:

$$I(t) = \frac{\hbar\omega_0}{4\tau_0}\mu\bar{N}(\bar{N} - N_0)\left[\mathrm{sech}^2\left(\frac{t-\tau_D}{2\tau_R}\right)\right] \qquad \tau_R = \frac{\bar{\tau_0}}{\mu(\bar{N} - N_0)} \tag{5.4}$$

and Eq. 5.3 are given by:

$$R_p = \frac{\mu}{4\bar{\tau_0}}\bar{N}(\bar{N} - N_0) \qquad \tau_R = \frac{N_0}{8R_p}\left(1 + \sqrt{1 + \frac{16\bar{\tau_0}}{\mu N_0^2}R_p}\right) \tag{5.5}$$

These two last equations are used to fit the data in Fig. 5.4b,d. The goodness of the fit is even more remarkable if we consider that the only two free parameters have a physical meaning: μ is the geometrical factor and N_0 accounts for the gain due to inverted population. In Tab. 5.1 we report the fit-parameters values for 3 excitation conditions.

TABLE 5.1

Laser fluence [ph/s]	μ	$\bar{N_0}$
$2.3 \cdot 10^{17}$	2.2×10^{-6}	0.88×10^{12}
$6.5 \cdot 10^{17}$	2.5×10^{-6}	1.75×10^{12}
$9.8 \cdot 10^{17}$	2.7×10^{-6}	1.80×10^{12}

The μ values obtained for different laser intensities vary slighly as one might expect because the beam waist is the same. For our geometry $\mu = 8\pi S/3\lambda^2 \approx 3.4 \cdot 10^{-6}$, which is in good agreement with the experimental values reported in the Tab. 5.1. We must take into account that the calculated value μ is valid for a homogeneously excited medium (Eq. 3.31,[75]), whereas our population inversion is induced by a Gaussian laser beam. Note that in previously reported experiments the discrepancy between experimental and theoretical values is much larger.

The values of N_0 show a stronger dependence on the laser excitation, similar to the inverted population trend (as will be detailed in next section 5.1.4), thereby supporting our assumption of amplification of SF pulses via stimulated emission.

When the laser intensity is high, larger fluctuations on the inverted population are observed. This effect may also explain why the data in Figures 5.4b, and 5.4d are more scattered for higher laser fluencies. By taking into account N_0, the MD is formed by cooperative ions in number as large as $4 \cdot 10^{12}$.

The coherence time

The observed pulse durations suggest that $T_2 \gg 40\,\text{ns}$. Even though the coherence time for Er:YSO 0.1% is not reported in literature, we can refer to the two results that are summarized in Tab. 1.3: $T_2 \approx 1\,\mu\text{s}$ for Er:YLF doped at 0.005% at 4.2 K and $T_2 = 100\,\mu\text{s}$ for Er:YSO 0.02% at 1.6 K and magnetic field B=3 T. According to the discussion in Sec. 1.3, we can thus expect a coherence time for our sample in the order of few μs, in a good agreement with our findings.

Off-axis superfluorescence

The forward SF has a well defined properties which are in agreement with the theoretical expectations. In backward direction, on the contrary, we have not registered any SF trace. The Ederly and Rehler model actually predicts different intensities for the forward and backward direction and this aspect deserves more investigations and specific simulations. Unexpectedly, we observe SF bunches in off-axis emission. Above the laser threshold of the forward SF (≈30 mW) and up to $\sim$ 230 mW ($\approx 7.8 \cdot 10^{17}$ph/s) laser power, we record small amplitude signals that are all in coincidence with those in forward direction and have the same duration. These pulses correpond to the forward SF photon bunches scattered by the crystal and window surfaces. For the highest laser power values, other much more intense off-axis pulses are observed that are uncorrelated with those emitted in the forward direction, and whose duration is a little longer as shown in Fig. 5.6a. They are well described by Eq 5.2 and the relation between τ_R and P follows Eq 5.5[7]. This off-axis SF arises when the excited ions density is so high that MD radiation is no longer tied to the cylinder axis. At the laser wavelengths and polarizations investigated, the absorption is strong ($\alpha > 1\,\text{cm}^{-1}$) which implies a high excitation density in the first part of the crystal, most likely to generate off-axis SF.

[7]The off-axis pulses cannot properly be collimated and focused. Instead of the calibrated R_p we use the peak amplitude of the signal and a scaling factor is added to the fit formula as free parameter.

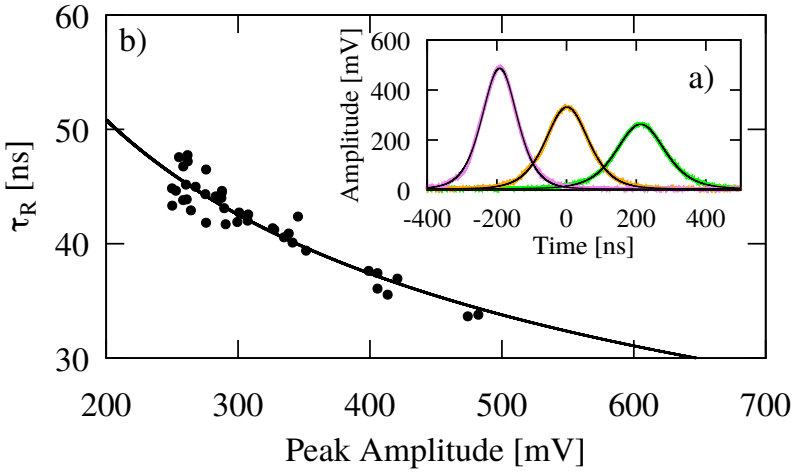

FIGURE 5.6: Spontaneously generated off-axis SF pulses. a) Representative single time traces (purple, orange, green) of photon bunches recorded under identical excitation conditions. The black lines are obtained by fitting the data with Eq. 5.2. b) τ_R versus peak amplitude P. The black lines are fits in the form given by Eq. 5.5.

5.1.4 Dependence on excitation intensity

To assess the effect and the SF dependence on the level population we carry out measurements of the emitted intensity by averaging over several thousands of photon bunches. We apply a magnetic field to reduce the peak absorption (see Fig. 5.7a) and to obtain a more homogeneous population inversion density along the crystal. The forward SF averaged intensity is measured by the Ge-based bolometer and at the same time also the incident and transmitted laser powers are recorded. In addition, off-axis emissions are monitored by the near-infrared spectrometer.

The intensity of the seven "ordinary" lines of the emission spectrum is proportional to the isotropic, incoherent emission power. The absolute value of the latter and the related inverted population are obtained as follows. At low laser excitation, we are able to estimate the number of inverted atoms N_e from the measured absorbed power Φ because at steady-state we have $\Phi = N_e/\tau_0$. For high laser excitation, the previous equation cannot be applied any longer due to the occurrence of SF. However, N_e/τ_0 still gives the intensity of incoherent emission and, hence, from the spectral intensity of the seven lines and their calibration at low excitation, we are able to estimate N_e in the whole range of pump laser intensity. Basically, the integrated spectral intensity of the isotropic spontaneous emission is converted to the number inverted atoms by imposing a linear dependence with slope τ_0 to the data recorded at low pumping levels (see Fig. 5.7c).

The averaged spectral intensity at 1545 nm (see Fig. 5.2 and Fig. 5.1) accounts for several contributions which take place at different inverted population levels.

For low intensity, the line simply represents the incoherent emission, such as the other seven. Above the forward SF threshold, the relative intensity of the line at 1545 nm grows with respect to the other seven. Scattered light of the forward SF beam is responsible for this contribution. At higher laser intensity, off-axis SF can be appreciated by the spectrometer. The first contribution is proportional to the spectral intensity of the seven ordinary lines and the second has the same trend of the measured forward SF. The third term can be thus estimated by subtracting the other two from the observed spectral intensity.

In Fig. 5.7a we show again for convenience the absorption spectrum with and without the magnetic field for the transitions of interest. We repeat our analysis for two laser wavelengths indicated by blue ($\lambda = 808.0025$ nm) and red ($\lambda = 808.0015$ nm) dots. Fig. 5.7b shows the forward SF power as function of the inverted population. It has a quadratic dependence above threshold as long as off-axis SF becomes relevant (Fig. 5.7d). By fitting the data with a function: $SF(N_e) = a(N_e - N_t)^2$ where a is a scaling factor, we finely estimate the inverted population threshold N_t for the forward SF. The different thresholds for the two laser wavelengths seem to indicate the dependence of the process on the excited ion density instead of the total inverted population.

The relation between the inverted population and the absorbed laser fluence can be approximately described by the simple steady-state equations:

$$\Phi - N_e/\tau_0 = 0 \qquad (N_e < N_t) \tag{5.6}$$

$$\Phi - \mathrm{N_e}/\tau_0 - b(N_e - N_t)^2 = 0 \qquad (N_e > N_t) \tag{5.7}$$

where b quantifies the level depletion by the forward SF and is the only free parameter. The equations predict a linear dependence on laser excitation below threshold and a sublinear dependence above it. Fig. 5.7b shows that the data are well fitted by this solution as long as the off-axis SF is not relevant. In this case Eq. 5.7 is not valid and a much complex model has to be introduced. However, we are able to estimate the maximum fraction of excited ions that relax via coherent emission. As we measure the absorbed laser power and estimate the incoherent emission power, we can obtain the total SF power. In other words, the gap between the projected linear fluorescence and the measured values gives the fraction of ions that cooperatively radiate, which we find to be 74% for the highest laser absorption.

The MDs involve only a little fraction of the inverted population, and we believe that this selection is determined by the inhomogeneous linewidth. We record pulses composed of up to $4 \cdot 10^{12}$ photons, when more than 10^{15} ions are in an excited state. By considering the values in Tab. 1.3, we expect a linewidth for the transition at 1545 nm larger than 600 MHz, which corresponds to a dephasing time

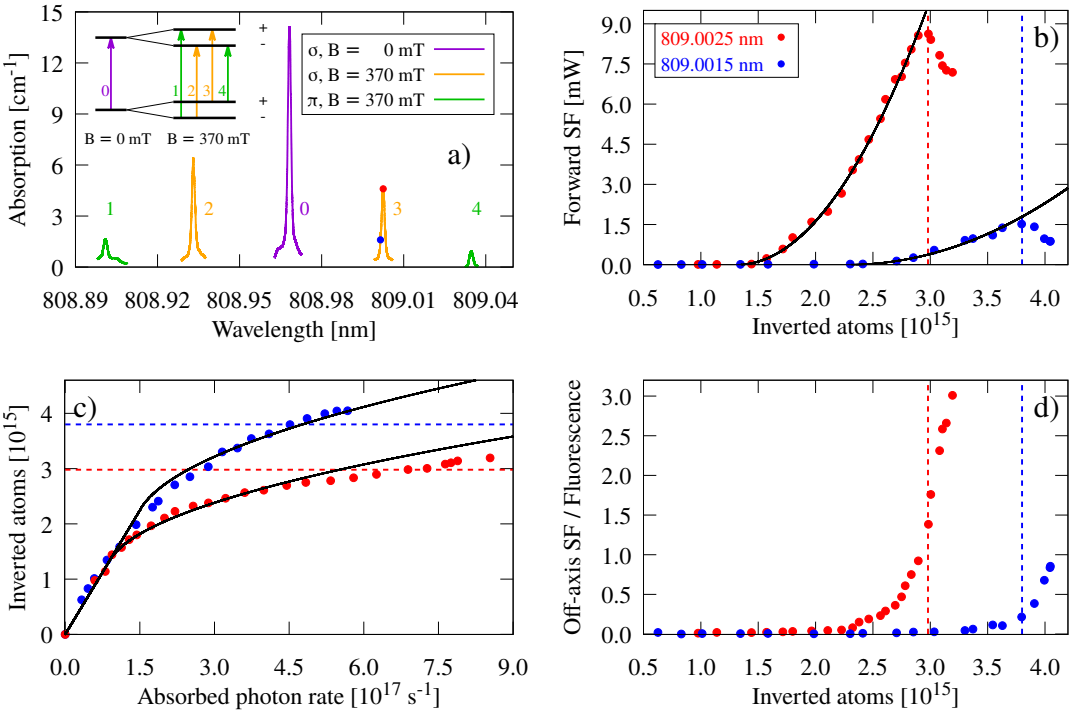

FIGURE 5.7: Absorption laser spectroscopy for the transition $^4I_{9/2}(1) \rightarrow {}^4I_{15/2}(1)$. (b) Forward (d) and off-axis SF average intensity for different longitudinal profiles of the inverted population density at absorption coefficients 1.6 cm^{-1} (809.0015 nm, blue dots) and 4.6 cm^{-1} (809.0025 nm, red dots). The black lines are a parabolic fit to the data. (c) Data agreement with steady-state rate equations analysis. The dotted lines indicate when the off-axis emission is so important as to reverse the growth trend in the forward emission. The data selected for the fit is bounded in y-range by 0 and the dotted lines.

less than 500 ps[8]. This timescale would be shorter or comparable to the SF delay time τ_d even if all 10^{15} ions were involved in cooperative emission. Hence, the excited ion population is divided into a large number of subensembles from which SF pulses can be generated independently. From our results, we can estimate $T_2^* > \tau_d \approx 10\tau_R \approx 300$ ns corresponding to an ion subensemble with a linewidth smaller than 1 MHz.

We draw the conclusion that SF manages to take place in Er:YSO because the required number of coupled identical ions to fulfill $\tau_R \ll T_2$ are available thanks to the narrow frequency spread. In other words, SF occurs for the long coherence time T_2 and the existence of large enough subensemble of identical ions.

[8]The laser linewidth is ≥10 MHz but it is tuned to another transition and we do not know how a fine excitation of a higher level is reflected to the excitation width of the lower ones.

5.2 Superfluorescence in Er:YLF 0.01% and Er:YLF 1%

In Er:YSO 0.1% we have obtained remarkable SF features, involving $\sim 10^{12}$ cooperative ions with a characteristic lifetime of several tens of nanoseconds. We repeat the experimental procedure for the Er:YLF crystals and here we present the preliminary findings. This allows us to gain a deeper understanding of the role played by host matrix and concentration in the manifestation of SF.

Thanks to the low phonon energy of the YLF matrix, the $^4I_{11/2}$ manifold has a measured lifetime of (7.8 ± 0.1) ms at 1.6 K with an efficient emission at $\sim$2700 nm (see Fig. 4.7) and at $\sim$1000 nm. The $^4I_{13/2}$ lifetime is (16.5 ± 0.1) ms, and also in this case SF characterizes the strongest transition which involves the second Stark level of the ground state with an estimated branching ratio $\beta \approx 24\%$. The time associates to the SF transition is thus $\bar{\tau_0} = \tau_0/\beta \approx 69$ ms.

Er-doped YLF has much smaller absorption coefficient and for both concentration the excitation along the medium is more uniform compared to Er:YSO. As the Er:YLF crystals length is 5 mm and the beam waist 163 μm, the Fresnel number is ≈ 11.

5.2.1 Dependence on excitation intensity

The quadratic dependence of the SF intensity on the incoherent fluorescence intensity, proportional to the inverted population is shown in Fig, 5.8. For higher pump laser intensities, only a small fraction of the absorbed power is emitted via cooperative emission in Er:YLF 0.01% as demonstrated by the plot in Fig, 5.8c. Er:YLF 1% is instead characterized by a more intense SF, which deviate from the $(N_e - N_t)^2$ dependence as a result of off-axis emission.

5.2.2 Superfluorescence Pulses Analysis

We record the SF pulses for Er:YLF 0.01% and 1% at 1.6 K with the Ti:Sapphire laser (II) wavelength tuned on the $^4I_{15/2}(1) \rightarrow ^4 I_{9/2}(1)$ transition. The crystals orientation is set as described in Chapter 2, with the c-axis orthogonal to the laser propagation. In this case, the InGaAs PD is set as close as possible to the cryostat output window to record the SF pulses. Their pulses shape is well fitted by Eq. 5.2 and if we report in the same plot (Fig. 5.9) the two data sets τ_R vs R_p and R_p vs $\bar{N}$ obtained with Er:YLF doped at 1% and 0.01% in different runs, they lie on the same fitting curve given by Eq 5.5. These data further demonstrate that

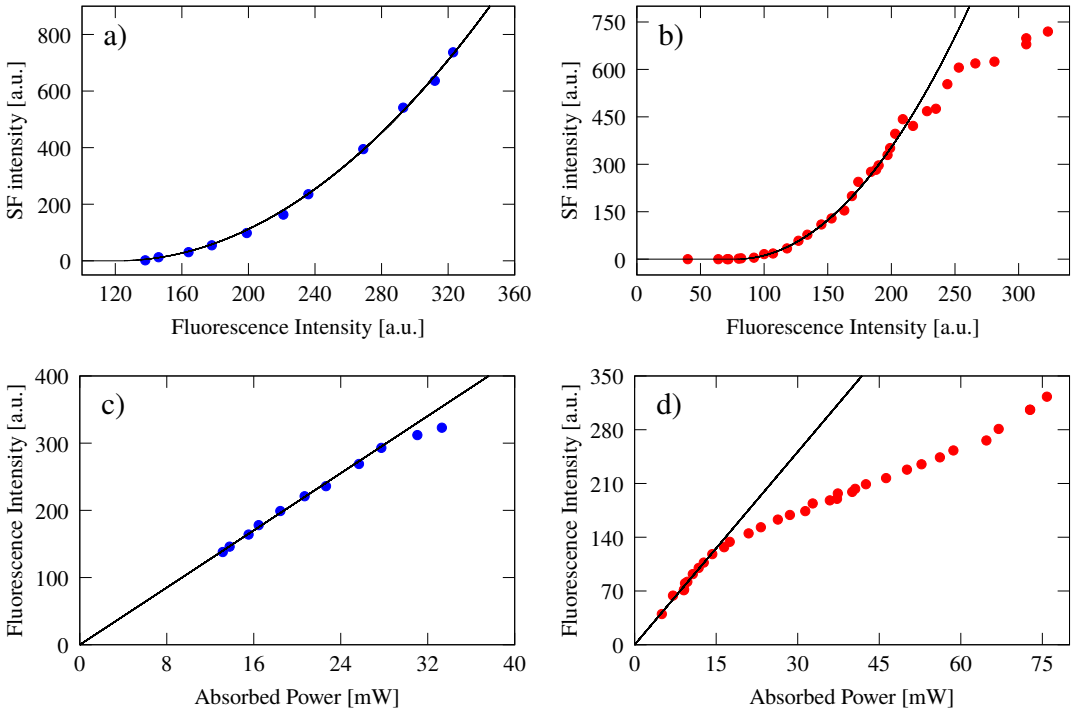

FIGURE 5.8: Relation between time averaged SF at 1534 nm, incoherent fluorescence in (1500-1700) nm range and absorbed laser power for Er:YLF 0.01% (blue dot, laser wavelength 808.992 nm) and for Er:YLF 1% (red dot, laser wavelength 809.0016 nm).

the pencil-shaped geometry coefficient μ and the time related to the transition $\bar{\tau}_0$, which coincide for the two crystals, are the only factors that determine the SF relationships. However, the different coherence time for the two sample, due to the different concentration as discussed in Chapter 1, has a strong impact on the characteristic number of ions involved into the superradiant decay.

SF takes place in Er:YLF 0.01% with less intense and longer pulses than Er:YLF 1%. The obtained fit parameters are $\mu = 1.5 \cdot 10^{-6}$ and $N = 5.3 \cdot 10^{11}$ for Er:YLF 0.01% and $\mu = 1.3 \cdot 10^{-6}$ and $N = 3 \cdot 10^{11}$ for Er:YLF 1%. We observe that N_0 and μ found in both Er:YLF crystals have smaller values than those found in Er:YSO. For the N_0 parameters it is probably due to the lower absorption coefficient and related inverted population, whereas for the geometry factor μ the reason of this discrepancy is not still clear. The results of Er:YSO in Tab. 5.1 seem to show a slight dependence of μ on the inverted population, but also a more homogeneously excited medium could be the cause of the low obtained values.

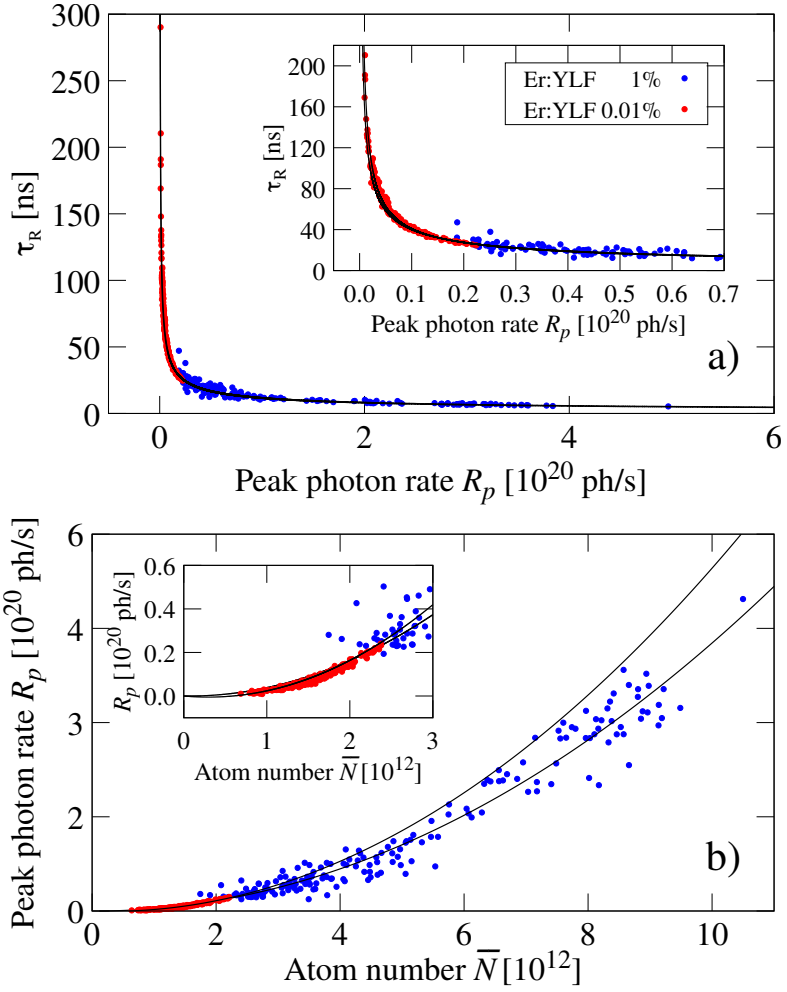

FIGURE 5.9: Main relations between SF pulses parameters. Black lines represent the data fit in the form given by Eq 5.5. In insets, the magnification highlights the common duration range for the pulses of the two crystals.

5.2.3 Cascaded Superfluorescence

A spectroscopic analysis of the coherent light beam extended to the mid infrared range reveals another highly directional emission at 2718 nm in addition to that at 1534 nm (Fig. 5.10). The mid infrared peak is compatible with the $^4I_{11/2}(1) \rightarrow {}^4I_{13/2}(2)$ transition [42, 134], already investigated by Auzel [133] and mentioned in Sec. 4.3.

The time evolution of the pulses within the emitted light beam is studied directly by using the InAs detector and representative examples of the recorded signals are shown in Fig. 5.11.

In this case, we observe the stochastic occurrence of two coupled pulses, separated by hundreds of nanoseconds. The use of bandpass filters enables us to assess that

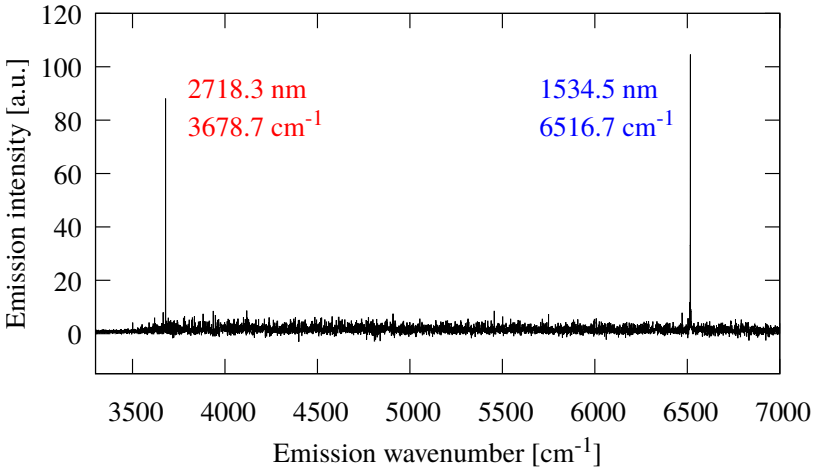

FIGURE 5.10: Cooperative emission spectrum of Er:YLF 0.01%. The spectrum is recorded by Equinox 55 (Bruker) FTIR-interferometer with a 0.5 cm^{-1} resolution, using the InAs PD as detector.

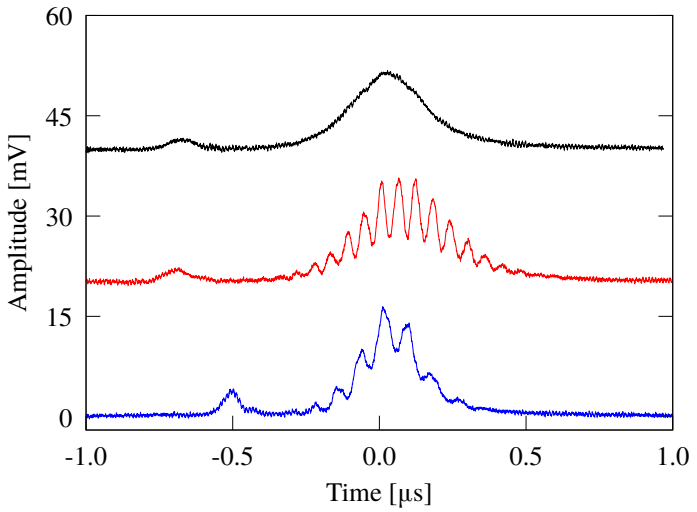

FIGURE 5.11: InAs signal of the overlapping two SF beams from Er:YLF 0.01%. An offset is added for clarity and the starting acquisition time is arbitrary.

the first pulse is related to the $^4I_{11/2}(1) \rightarrow {}^4I_{13/2}(2)$ transition (2.7 μm) and the second pulse to $^4I_{13/2}(1) \rightarrow {}^4I_{15/2}(2)$ transition (1.5 μm), as in a cascaded process[9].

It is important to note that the final level of the first transition and the starting level of the second one do not coincide and these two levels are connected by a multiphonon relaxation that destroys any coherence among the Er^{3+} ions. The coherence that gives rise to the superradiant emission at 1534 nm is thus a result of a spontaneous process, instead of the natural final state of a previous cooperative

[9]Observed pulses can have a modulation in the 10s MHz-few GHz range, which depends on the crystal-laser propagation alignment. We believe that such interference is due to unwanted reflections. This explanation is supported by the fact that these modulations are missing in the pulses emitted from Er:YSO, where the absorption of the laser power is more relevant.

transition. The use of the term "superfluorescence" for the 1534 nm cooperative emission (SF_2) is therefore correct. Cooperative nature of the emission at 2718 nm (SF_1) is proved by the quadratic dependence of the peak intensity with the number of involved atoms (Fig. 5.12).

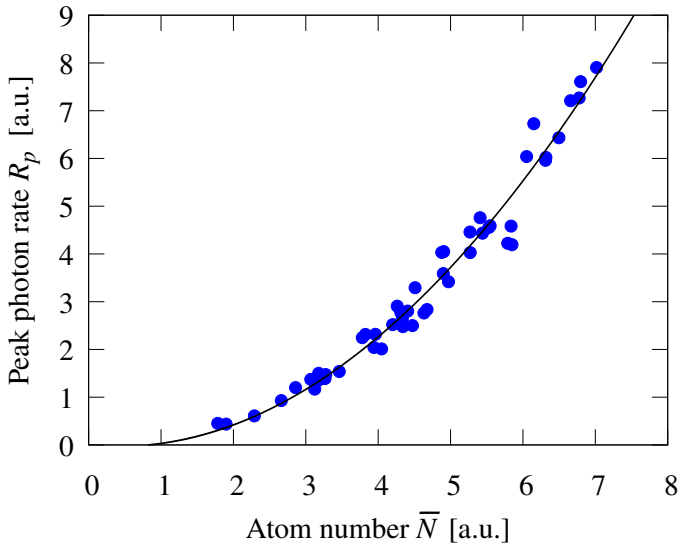

FIGURE 5.12: Peak photon rate versus observed photon number. The pulses are recorded with the InAs PD and using a bandpass filter (Thorlabs, FB2500-500). Black lines represent the data fit in the form given by Eq 5.5. We cannot properly estimate the number of photons per bunch because the total transmittance of the optical elements for such wavelength is unknown.

The $^4I_{11/2}$ has stronger emission line towards the ground state $^4I_{15/2}$ than $^4I_{13/2}$ [34], nonetheless SF does not occur for such transition. We must recall that the inverted population threshold N_t depends not only on the transition rate but also on λ^{-2} (Eq. 3.34) and thus the longer wavelengths are favored. In Er:YSO the $^4I_{11/2}$ manifold has a short lifetime even at low temperature and no SF transition in the mid infrared range has been detected. The $^4I_{11/2}$ lifetime in YLF matrix is much longer and the high excitation density could seed the cooperative emission.

When both the SF_1 and SF_2 emissions are observed, the delay time of the photon bunches at 1534 nm can be measured. The SF_1 pulses quickly drive a large number of ions from the $^4I_{11/2}(1)$ manifold to one of the excited Stark levels of the $^4I_{13/2}$ manifold, which in turn immediately relax to the lowest Stark level losing their macroscopic coherent state. Here, MD is formed again that generates the SF_1 at 1534 nm. The distance between the maxima of the SF pulses is to a first approximation the delay time for SF_2, in which the measurement accuracy is set by τ_{R1}.

The analysis of the pulses is shown in Fig. 5.13 and no correlation between τ_{R1} and τ_{R2} can be deduced. Probably this is due to the stochastic nature of SF or to the inverted population on the $^4I_{13/2}$ manifold which provides additional ions to the

SF_2 pulses. It is of interest that the estimated τ_d is proportional to τ_{R2}. In this way, we add another important evidence of the SF_2 occurrence instead of ASE. In fact, according to the Ederly and Rehler model and by assuming $N_2 = 10^{12}$ we should have:

$$\frac{\tau_{d2}}{\tau_{R2}} = ln(N_2\mu) \approx 15, \tag{5.8}$$

but the linear fit provides the value τ_{d2}/τ_{R2}=8.4. It is quite common that the predicted value of this ratio differs from the experimental one as it is difficult to properly consider in the model also the quantum fluctuations that give rise to the MD formation.

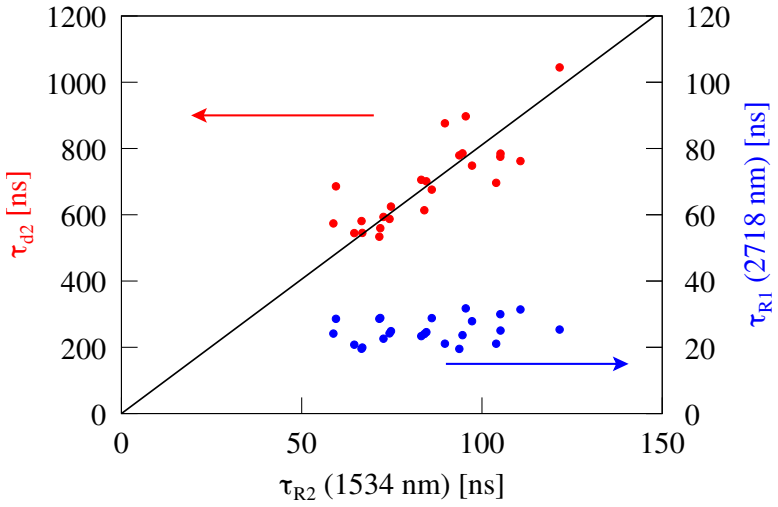

FIGURE 5.13: Time delay of SF_2 vs SF_2 time (red dots) in Er:YLF 0.01% recorded with InAs PD. The black line is a linear fit. No correlation between SF_2 time and SF_1 time (blue dots).

Summary and Outlook

We have thoroughly studied the pulsed coherent emission from Erbium-doped YSO and YLF crystals at 1.6 K. We have investigated the coherent beam propagation, the pulse features and the radiated power as a function of the laser excitation intensity and inverted population. For the first time, we have been able to unambiguously identify the occurrence of superfluorescence (SF) processes in Rare-Earth doped crystals, ruling out amplified spontaneous emission (ASE). An impressive agreement between the experimental results and the SF relationships has been found, as long as we introduce a term that accounts for the gain of the SF pulse as it propagates in the inverted medium.

The impressive number of measured correlated atoms ($\sim 10^{12}$) represents the highest value reported in the literature for the visible-near infrared band. This result is of importance, considering the fact that the active medium is excited by a cw pumping laser rather than by ultra-short laser pulses. In addition, the characteristic lifetime of the observed macro-coherent state ranges between tens to hundreds of nanoseconds, much longer than the typical values measured in other physical systems (See Section 4.2).

The obtained values make the Er:YLF and Er:YSO crystals an ideal test-bed for quantum optics effects, especially the macrocoherent amplification processes. In particular, the cooperative absorption of photons, namely superabsorption, can be investigated by tuning a second laser between the excited level, on which the macrocoherence is established, and a higher one.

The possible applications of the quantum coherence can emerge also in particle physics. We have shown that the background related to the upconversion process in the Sikivie's scheme investigated in this work, can be so large to prevent the observation of the axion signal. The macro-coherent state could be employed to boost the axion interaction rate, as well as that of other elusive event, including neutrino pair emission in atomic transition. To check these possibilities and to devise the best detection scheme based on the macro-coherent states, the demonstration of the superabsorption in these physical systems and the enhancement of the coherent amplification, proportional to the cooperative atom number, represent fundamental steps in this direction.

The data regarding the Er:YSO presented in this thesis, indicates that an increase of the number of correlated atoms can be obtained with larger inverted population, which can be achieved with higher laser intensity and larger excited volume. It is useful to recall that the increase of the correlated atom number and the relative accelerated emission is limited by the fact that the SF time cannot exceed the photon escape time. For this reason, an arbitrarily large gain cannot be obtained considering longer media. If we increase the diameter of the active medium and thus the μ parameter, we could avoid the further acceleration of the emission time. However, the turning away from the ideal pencil-shape condition leads to a growing of the off-axis SF emission and thus to a reduction of the forward SF intensity.

The studies on the Er:YLF crystals have shown that the dopant concentration plays a role on the required atom number for the SF occurrence. The reduced coherence time due to a higher interaction rate between the dopants ions implies that SF must include a larger number of correlated atoms to occur. However, too short coherence times and a inhomogeneous linewidth broadening due to the higher concentration totally suppress the cooperative processes.

Appendix

Amplified spontaneous emission in Tm:LLF 12%

In Chapter 5, we have reported the SF observation in Er-doped crystals with a concentration up to 1%. Now, we present a similar study carried out on the Tm:$LiLuF_4$ crystal doped at 12%. This observation allows us to compare the results obtained for a different RE ions dopant with a much higher concentration and the cooperative emission with the lasing effect.

Crystal growth

The Tm:$LiLuF_4$ doped at 12% crystal was growth by Pisa group with a procedure similar to that used for YLF crystals as described in Sec.1.4.2. The 5N purity powder of LiF and YF_3 along with 12% of TmF_3 has the melt temperature of 860 °C and the pulling rate was fixed to 1 mm/h.

Excitation scheme

The energy level scheme of Tm^{3+} is shown in Fig. 5.14a. We measure a lifetime for the $^3F_4(1)$ level as long as 17.3 ms at 1.6 K making possible to easily produce a large inverted population and to investigate the occurrence of cooperative processes. The excitation required to directly excite the level of interest cannot be provided by our laser system. However, we can exploit the energy transfer process discussed in Sec. 1.2.3 to overcome this problem. The cross relaxation $(^3H_4, ^3H_6) \rightarrow (^3F_4, ^3F_4)$ depicted in Fig. 5.14 is very efficient, indeed. The lifetime at low temperature of the $^3H_4$ manifold decreases with the increasing of Tm concentration from 3 ms for Tm:LLF 0.3% down to less than 50 μs for our crystal, thereby indicating that more than 95% of the ions in $^3H_4$ manifold relax for energy transfer process.

The Ti:Sa laser (II) is tuned between the ground state and the $^3H_4(1)$ level at 792.11 nm and the absorption line (Fig. 5.14b) is obtained by recording the fluorescence at ∼1800 nm in the same configuration adopted for the Er-doped crystal

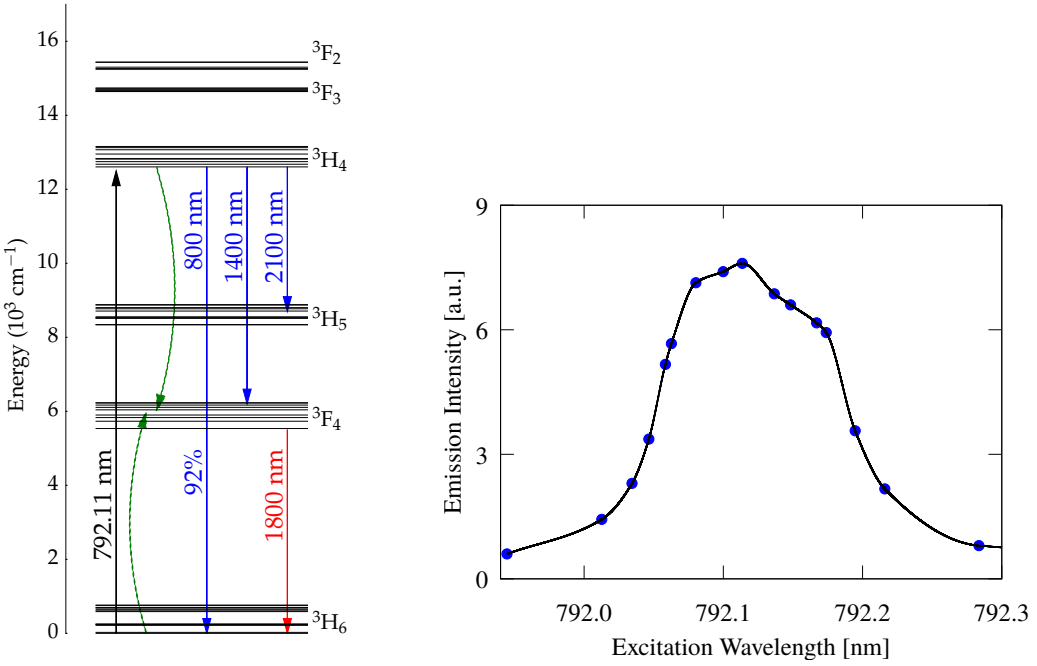

FIGURE 5.14: (left) The energy level scheme of Tm-doped YAG is presented here as a reference because the energy levels for LLF are not available in literature. The cross relaxation path is represented with green arrows. (right) Absorption line of the transition $^3\mathrm{H}_6(1) \rightarrow {}^3\mathrm{H}_4(1)$.

spectroscopic studies. A linewidth as broad as $\sim$ 70 GHz is found due to the inhomogeneous broadening caused by the heavy concentration.

Amplified spontaneous emission features

No highly directional emission is observed for laser power up to 800 mW when the beam waist is 163 μm. However, ASE takes place when a large excited ion density is achieved by reducing the laser beam waist on the crystal to 52 μm. In Fig. 5.15 the intensity of the high directional emission and the "ordinary" incoherent luminescence are shown as a function of the incident pump laser power. The linear dependence above threshold of the coherent emission is the clear signature of lasing effect, i.e. ASE. Note that the inverted population represented by the incoherent emission intensity is almost constant above the ASE threshold. The additional excited ions provided by the increasing laser intensity completely relax via stimulated emission.

The analysis of the time evolution of the ASE beam shows that it is composed by photon bunches with the same shape of SF pulses described by the Eq. 5.2 (Fig. 5.15 inset). However, the analysis of the fit parameters clearly indicates a linear dependence of peak intensity on the area of the pulse proportional to the

number of ions involved in the process. This trend unambiguously identifies the occurrence of ASE.

There are no pieces of information about the coherence time of Tm:LLF 12%, but it is surely limited by the high concentration satisfying the condition $\tau_R < T_2 < \sqrt{\tau_R \tau_d}$ set for the ASE.

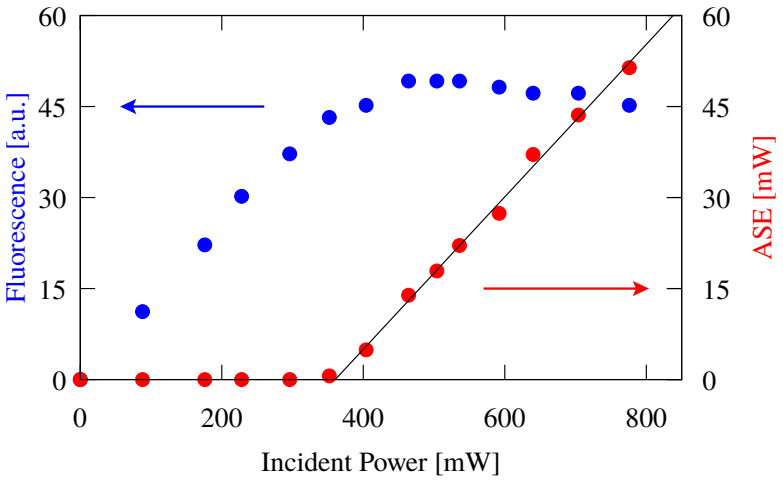

FIGURE 5.15: ASE (red dots) and incoherent emission (blue dots) dependence on the incident laser power.

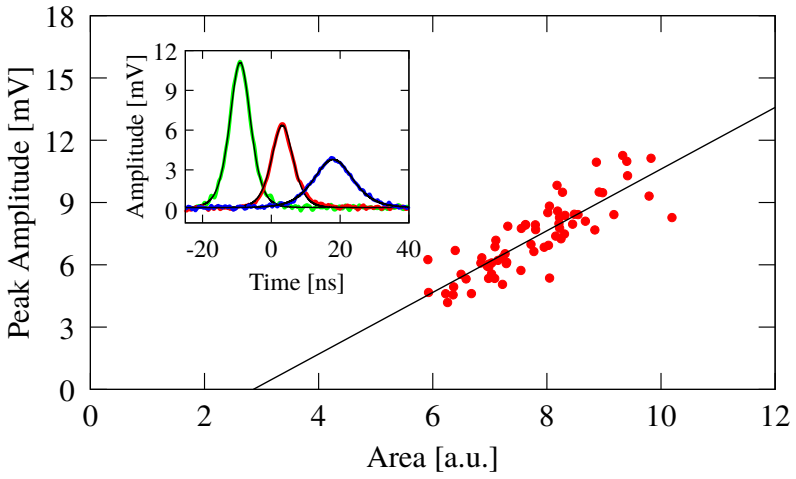

FIGURE 5.16: In inset are shown the three representative pulses generated by ASE process. In the main figure, the peak pulse amplitude vs pulse area is plotted. The black line is a linear fit.

Bibliography

[1] P. Sikivie. Axion Dark Matter detection using atomic transitions. *Physical Review Letters*, 113:201301, 2014.

[2] N. Bloembergen. Solid state infrared quantum counters. *Physical Review Letters*, 2:84, 1959.

[3] R. H. Dicke. Coherence in spontaneous radiation processes. *Physical Review*, 93:99110, 1954.

[4] D. Yang, S. Oh, J. Han, G. Son, J. Kim, J. Kim, and K. An. Observation of superabsorption by correlated atoms. *arXiv preprint arXiv:1906.06477*, 2019.

[5] A. Fukumi, S. Kuma, Y. Miyamoto, K. Nakajima, I. Nakano, H. Nanjo, C. Ohae, N. Sasao, M. Tanaka, T. Taniguchi, et al. Neutrino spectroscopy with atoms and molecules. *Progress of Theoretical and Experimental Physics*, 2012:04D002, 2012.

[6] Y. Miyamoto, H. Hara, S. Kuma, T. Masuda, I. Nakano, C. Ohae, N. Sasao, M. Tanaka, S. Uetake, A. Yoshimi, et al. Observation of coherent two-photon emission from the first vibrationally excited state of hydrogen molecules. *Progress of Theoretical and Experimental Physics*, 2014:113C01, 2014.

[7] Y. Miyamoto, H. Hara, T. Masuda, N. Sasao, S. Uetake, A. Yoshimi, K. Yoshimura, and M. Yoshimura. Vibrational two-photon emission from coherently excited solid parahydrogen. *The Journal of Physical Chemistry A*, 121:3943–3951, 2017.

[8] Guo-yuan Huang and Shun Zhou. Probing cosmic axions through resonant emission and absorption in atomic systems with superradiance. *arXiv preprint arXiv:1905.00367*, 2019.

[9] H. Hara and M. Yoshimura. Raman stimulated neutrino pair emission. *The European Physical Journal C*, 79:684, 2019.

[10] H. Hara, N. Sasao, and M. Yoshimura. Divalent lanthanoid ions in crystals for neutrino mass spectroscopy. *arXiv preprint arXiv:1909.06554*, 2019.

[11] H Hara, N Sasao, A Yoshimi, and M Yoshimura. Neutrino mass spectroscopy using Er^{3+} ions placed at inversion center of host crystals. *arXiv preprint arXiv:1910.14318*, 2019.

[12] G. Liu. *Spectroscopic properties of rare earths in optical materials*. Tsinghua Univ. Press, 2010.

[13] B. G. Wybourne and L. Smentek. *Optical spectroscopy of lanthanides: magnetic and hyperfine interactions*. CRC press, 2007.

[14] S. Hufner. *Optical Spectra of Transparent Rare Earth Compounds*. Elsevier Science, 2012.

[15] W. T. Carnall, G. L. Goodman, K. Rajnak, and R. S. Rana. A systematic analysis of the spectra of the lanthanides doped into single crystal LaF_3. *The Journal of Chemical Physics*, 90:3443–3457, 1989.

[16] P. S. Peijzel, A. Meijerink, R. T. Wegh, M. F. Reid, and G. W. Burdick. A complete energy level diagram for all trivalent lanthanide ions. *Journal of Solid State Chemistry*, 178:448–453, 2005.

[17] B. M. Walsh. Judd-Ofelt theory: principles and practices. In *Advances in spectroscopy for lasers and sensing*. Springer, 2006.

[18] Y. Chen and F. Auzel. Investigation of multiphonon assisted side band absorptions in rare-earth-doped halide glasses and crystals. *Journal of Non-Crystalline Solids*, 184:278–281, 1995.

[19] B. Henderson and G. F. Imbusch. *Optical spectroscopy of inorganic solids*, volume 44. Oxford University Press, 2006.

[20] K. Rademaker. *Rare earth-doped alkali-lead-halide laser crystals of low-phonon energy*. Cuvillier, 2005.

[21] J. D. Zuegel and W. Seka. Direct measurements of $^4I_{11/2}$ terminal-level lifetime in Nd:YLF. *IEEE journal of quantum electronics*, 31:1742–1746, 1995.

[22] C. Bibeau, S. A. Payne, and H. T. Powell. Direct measurements of the terminal laser level lifetime in neodymium-doped crystals and glasses. *Journal of Optical Society of America B*, 12:1981–1992, 1995.

[23] T. Böttger, C. W. Thiel, Y Sun, and R. L. Cone. Optical decoherence and spectral diffusion at 1.5 μ m in Er^{3+}: Y_2SiO_5 versus magnetic field, temperature, and Er^{3+} concentration. *Physical Review B*, 73:075101, 2006.

[24] Q. Chen, A. Troshyn, I. Ernsting, S. Kayser, S. Vasilyev, A. Nevsky, and S. Schiller. Spectrally narrow, long-term stable optical frequency reference based on a Eu^{3+}:Y_2SiO_5 crystal at cryogenic temperature. *Physical review letters*, 107:223202, 2011.

[25] T. Miyakawa and D. L. Dexter. Phonon sidebands, multiphonon relaxation of excited states, and phonon-assisted energy transfer between ions in solids. *Physical Review B*, 1:2961, 1970.

[26] A. Abragam and A. Abragam. *The principles of nuclear magnetism*. Oxford university press, 1961.

[27] G. K. Liu and R. L. Cone. Laser-induced instantaneous spectral diffusion in Tb^{3+} compounds as observed in photon-echo experiments. *Physical Review B*, 41:6193, 1990.

[28] G. Kawamura, R. Yoshimura, K. Ota, S. Oh, N. Hakiri, H. Muto, T. Hayakawa, and A. Matsuda. A unique approach to characterization of sol-gel-derived rare-earth-doped oxyfluoride glass-ceramics. *Journal of the American Ceramic Society*, 96:476–480, 2013.

[29] M. D. Dramićanin, B. Viana, Andrić Ž., V. Djoković, and A. S. Luyt. Synthesis of Y_2SiO_5: Eu^{3+} nanoparticles from a hydrothermally prepared silica sol. *Journal of Alloys and Compounds*, 464:357–360, 2008.

[30] M. A. Couto Dos Santos, E Antic-Fidancev, J. Y. Gesland, J. C. Krupa, M Lemaıtre-Blaise, and P Porcher. Absorption and fluorescence of Er^{3+}-doped $LiYF_4$: measurements and simulation. *Journal of Alloys and Compounds*, 275:435–441, 1998.

[31] K. I. Gerasimov, M. M. Minnegaliev, B. Z. Malkin, E. I. Baibekov, and S. A. Moiseev. High-resolution magneto-optical spectroscopy of $^{7}LiYF_4$:$^{166}Er^{3+}$, $^{167}Er^{3+}$ and analysis of hyperfine structure of ultranarrow optical transitions. *Physical Review B*, 94:054429, 2016.

[32] X. X. Zhang, A. Schulte, and B. H. T. Chai. Raman spectroscopic evidence for isomorphous structure of $GdLiF_4$ and $YLiF_4$ laser crystals. *Solid State Communications*, 89:181–184, 1994.

[33] L. Zheng, G. Zhao, C. Yan, X. Xu, L. Su, Y. Dong, and J. Xu. Raman spectroscopic investigation of pure and ytterbium-doped rare earth silicate crystals. *Journal of Raman Spectroscopy*, 38:1421–1428, 2007.

[34] A. M. Tkachuk, I. K. Razumova, A. A. Mirzaeva, A. V. Malyshev, and V. P. Gapontsev. Up-conversion and population of excited erbium levels in $LiY_(1-x)Er_xF_4$ (x=0.003-1) crystals under cw InGaAs laser-diode pumping. *Optics and Spectroscopy*, 92:67–82, 2002.

[35] C. Li, C. Wyon, and R. Moncorge. Spectroscopic properties and fluorescence dynamics of Er^{3+} and Yb^{3+} in Y_2SiO_5. *IEEE Journal of Quantum Electronics*, 28:1209–1221, 1992.

[36] T. Böttger, C. W. Thiel, R. L. Cone, and Y. Sun. Effects of magnetic field orientation on optical decoherence in Er^{3+} :Y_2SiO_5. *Physical Review B*, 79: 115104, 2009.

[37] N. Kukharchyk, D. Sholokhov, O. Morozov, S. L. Korableva, A. A. Kalachev, and P. A. Bushev. Optical coherence of ^{166}Er:^{7}$LiYF_4$ crystal below 1 K. *New Journal of Physics*, 20:023044, 2018.

[38] C. W. Thiel, W. R. Babbitt, and R. L. Cone. Optical decoherence studies of yttrium oxyorthosilicate Y_2SiO_5 codoped with Er^{3+} and Eu^{3+} for optical signal processing and quantum information applications at 1.5 microns. *Physical Review B*, 85:174302, 2012.

[39] M. N. Popova, E. P. Chukalina, B. Z. Malkin, and S. K. Saikin. Experimental and theoretical study of the crystal-field levels and hyperfine and electron-phonon interactions in $LiYF_4$:Er^{3+}. *Physical Review B*, 61:7421–7427, 2000.

[40] M. M. Minnegaliev, E. I. Baibekov, K. I. Gerasimov, S. A. Moiseev, M. A. Smirnov, and R. V. Urmancheev. Photon echo of an ultranarrow optical transition of $^{167}Er^{3+}$ in $^{7}LiYF_4$ crystals. *Quantum Electronics*, 47:778–782, 2017.

[41] N. Kukharchyk, D. Sholokhov, A. A. Kalachev, and P. A. Bushev. Enhancement of optical coherence in ^{167}Er:Y_2SiO_5 crystal at sub-Kelvin temperatures. *arXiv preprint arXiv:1910.03096*, 2019.

[42] M. N. Popova, E. P. Chukalina, B. Z. Malkin, and S. K. Saikin. Experimental and theoretical study of the crystal-field levels and hyperfine and electron-phonon interactions in $LiYF_4$:Er^{3+}. *Physical Review B*, 61:7421–7427, 2000.

[43] T. Böttger, C. W. Thiel, R. L. Cone, and Y. Sun. Controlled compositional disorder in Er^{3+}:Y_2SiO_5 provides a wide-bandwidth spectral hole burning material at 1.5μm. *Physical Review B*, 77, 2008.

[44] Y Sun, C.W. Thiel, R. L. Cone, R. W. Equall, and R. L. Hutcheson. Recent progress in developing new rare earth materials for hole burning and coherent transient applications. *Journal of Luminescence*, 98:281–287, 2002.

[45] I. G. Irastorza and J. Redondo. New experimental approaches in the search for axion-like particles. *Progress in Particle and Nuclear Physics*, 102:89–159, 2018.

[46] R. D. Peccei and H. R. Quinn. CP conservation in the presence of instantons. *Physical Review Letter*, 38:1440–1443, 1977.

[47] R. Essig, A. Manalaysay, J. Mardon, P. Sorensen, and T. Volansky. First direct detection limits on sub-GeV Dark Matter from XENON10. *Physical Review Letters*, 109:021301, 2012.

[48] C. Kouvaris and J. Pradler. Probing sub-GeV Dark Matter with conventional detectors. *Physical Review Letters*, 118:031803, 2017.

[49] J. E. Kim. Weak-interaction singlet and strong CP invariance. *Physical Review Letters*, 43:103, 1979.

[50] M. Dine, W. Fischler, and M. Srednicki. A simple solution to the strong CP problem with a harmless axion. *Physics Letters B*, 104:199–202, 1981.

[51] M. Dine and W. Fischler. The not-so-harmless axion. *Physics Letters B*, 120:137–141, 1983.

[52] S. Borsanyi, Z. Fodor, J. Guenther, K. H. Kampert, S. D. Katz, T. Kawanai, T. G. Kovacs, S. W. Mages, A. Pasztor, F. Pittler, and et al. Calculation of the axion mass based on high-temperature lattice quantum chromodynamics. *Nature*, 539:69–71, 2016.

[53] D. G. G. Cortona, E. Hardy, J. P. Vega, and G. Villadoro. The QCD axion, precisely. *Journal of High Energy Physics*, 2016:34, 2016.

[54] G. Raffelt. Astrophysical axion bounds. In *Axions*. Springer, 2008.

[55] C. P. D. G. Patrignani, D. H. Weinberg, C. L. Woody, R. S. Chivukula, O. Buchmueller, Y. V. Kuyanov, E. Blucher, S. Willocq, A. Höcker, C. Lippmann, et al. Review of particle physics. *Chinese Physics*, 40:100001, 2016.

[56] J. Bovy and S. Tremaine. On the local dark matter density. *The Astrophysical Journal*, 756:89, 2012.

[57] S. J. Asztalos, G. Carosi, C. Hagmann, D. Kinion, K. Van Bibber, M. Hotz, L. J. Rosenberg, G. Rybka, J. Hoskins, J. Hwang, and et al. SQUID-based microwave cavity search for Dark-Matter axions. *Physical Review Letters*, 104:041301, 2010.

[58] O. Guillot-Noël, V. Mehta, B. Viana, D. Gourier, M. Boukhris, and S. Jandl. Evidence of ferromagnetically coupled Nd^{3+} ion pairs in weakly doped Nd:$LiYF_4$ and Nd:YVO_4 crystals as revealed by high-resolution optical and EPR spectroscopies. *Physical Review B*, 61:15338–15346, 2000.

[59] R. L. Belford, N. D. Chasteen, H. So, and R. E. Tapscott. Triplet state of vanadyl tartrate binuclear complexes and electron paramagnetic resonance spectra of the vanadyl.alpha.-hydroxycarboxylates. *Journal of the American Chemical Society*, 91:4675–4680, 1969.

[60] J. Magario, J. Tuchendler, P. Beauvillain, and I. Laursen. EPR experiments in $LiTbF_4$, $LiHoF_4$, and $LiErF_4$ at submillimeter frequencies. *Physical Review B*, 21:18–28, 1980.

[61] X. Zhou, S. Xia, and P. A. Tanner. Effective spin hamiltonian model for superexchange interaction between rare earth ions in rare earth elpasolite crystals. *The Journal of Physical Chemistry B*, 111:8677–8679, 2007.

[62] Y. Sun, T. Böttger, C. W. Thiel, and R. L. Cone. Magnetic g tensors for the $^4I_{15/2}$ and $^4I_{13/2}$ states of Er^{3+}:Y_2SiO_5. *Physical Review B*, 77:085124, 2008.

[63] T. L Bohan and H. J. Stapleton. Temperature and magnetic field dependence of the spin-lattice relaxation rates for Er^{3+}, Pr^{3+}, and Tb^{3+} in anhydrous $LaCl_3$. *Physical Review*, 182:385, 1969.

[64] D. M. Boye, R. Wannemacher, Y. P. Wang, W. Grill, J. E. Rives, and R. S. Meltzer. Zeeman-switched optical free induction decay in $YLiF_4$:Er^{3+}. *Journal of Luminescence*, 45:431–433, 1990.

[65] A. A. Antipin, B. N. Kazakov, S. L. Korableva, R. M. Rakhmatullin, Yu K. Chirkin, and A. A. Fedii. Spin-lattice relaxation and polarization of nuclei in impurity RE^{3+}-$YLiF_4$ single crystals. *Soviet Physics Journal*, 21:1187–1191, 1978.

[66] C. W. Thiel, T. Böttger, and R. L. Cone. Rare-earth-doped materials for applications in quantum information storage and signal processing. *Journal of Luminescence*, 131:353–361, 2011.

[67] M. P. Hehlen, W. L. Boncher, S. D. Melgaard, M. W. Blair, R. A. Jackson, T. E. Littleford, and S. P. Love. Preparation of high-purity LiF, YF_3, and YbF_3 for laser refrigeration. *Laser Refrigeration of Solids VII*, 9000:900004, 2014.

[68] D. A. Ender, H. J. Guggenheim, M. S. Otteson, R. L. Cone, and M. B. Ritter. Narrowed intermediate resonance in multiresonant four-wave mixing in $LiTbF_4$. *Optics Letters*, 7:611, 1982.

[69] G. K. Liu, J. Huang, R. L. Cone, and B. Jacquier. Spectral hole burning, zeeman effect, and hyperfine structure for Tb^{3+}:$LiYF_4$. *Physical Review B*, 38:11061–11067, 1988.

[70] R. Bonifacio and L. A. Lugiato. Introduction: What are Resonance Fluorescence, Optical Bistability, and Superfluorescence. *Topics in Current Physics Dissipative Systems in Quantum Optics*, pages 1–9, 1982.

[71] M. Gross and S. Haroche. Superradiance: An essay on the theory of collective spontaneous emission. *Physics Reports*, 93:301–396, 1982.

[72] L. Allen and J. H. Eberly. *Optical resonance and two-level atoms*. Dover, 1987.

[73] M. G. Benedict, A. M. Ermolaev, V. A. Malyshev, I. V. Sokolov, and E. D. Trifonov. Super-radiance: Multiatomic coherent emission, iop publ. 1996.

[74] K. Cong, Q. Zhang, Y. Wang, G. T. Noe, A. Belyanin, and J. Kono. Dicke superradiance in solids. *Journal of Optical Society of America B*, 33:C80–C101, 2016.

[75] N. E. Rehler and J. H. Eberly. Superradiance. *Physical Review A*, 3:1735–1751, 1971.

[76] R. Bonifacio and L. A. Lugiato. Cooperative radiation processes in two-level systems: Superfluorescence. II. *Physical Review A*, 12:587–598, 1975.

[77] R. Bonifacio and L. A. Lugiato. Cooperative radiation processes in two-level systems: Superfluorescence. *Physical Review A*, 11:1507–1521, 1975.

[78] P. A. M. Dirac. The quantum theory of the emission and absorption of radiation. *Proceedings of the Royal Society of London. Series A, Containing Papers of a Mathematical and Physical Character*, 114:243–265, 1927.

[79] F. Arecchi and R. Bonifacio. Theory of optical maser amplifiers. *IEEE Journal of Quantum Electronics*, 1:169–178, 1965.

[80] F. T. Arecchi and E. Courtens. Cooperative phenomena in resonant electromagnetic propagation. *Physical Review A*, 2:1730–1737, 1970.

[81] M. F. H. Schuurmans. Superfluorescence and amplified spontaneous emission in an inhomogeneously broadened medium. *Optics Communications*, 34:185–189, 1980.

[82] N. E. Rehler and J. H. Eberly. Superradiance. *Physical Review A*, 3:1735, 1971.

[83] M. F. H. Schuurmans and D. Polder. Superfluorescence and amplified spontaneous emission: A unified theory. *Physics Letters A*, 72:306–308, 1979.

[84] F. Gan and Y. Chen. The spectral characteristics of superfluorescence in rare-earth-doped silica fibres. *Pure and Applied Optics: Journal of the European Optical Society Part A*, 2:359–365, 1993.

[85] J. S. Bakos, D. P. Scherrer, and F. K. Kneubhl. Observation of two-photon noise-initiated fluctuations in far-infrared Dickes superradiance. *Physical Review A*, 46:410–413, 1992.

[86] A. T. Rosenberger and T. A. Detemple. Far-infrared superradiance in methyl fluoride. *Physical Review A*, 24:868–882, 1981.

[87] N. Skribanowitz, I. P. Herman, J. C. MacGillivray, and M. S. Feld. Observation of dicke superradiance in optically pumped HF gas. *Physical Review Letters*, 30:309, 1973.

[88] M. Nagasono, J. R. Harries, H. Iwayama, T. Togashi, K. Tono, M. Yabashi, Y. Senba, H. Ohashi, T. Ishikawa, and E. Shigemasa. Observation of free-electron-laser-induced collective spontaneous emission (superfluorescence). *Physical Review Letters*, 107:193603, 2011.

[89] J. R. Harries, H. Iwayama, M. Nagasono, T. Togashi, M. Yabashi, S. Kuma, K. Nakajima, Y. Miyamoto, C. Ohae, N. Sasao, et al. A streak camera study of superfluorescence at multiple wavelengths from helium atoms excited using free electron laser pulses. *Journal of Physics B: Atomic, Molecular and Optical Physics*, 48:105002, 2015.

[90] J. R. Harries, H. Iwayama, S. Kuma, M. Iizawa, N. Suzuki, Y. Azuma, I. Inoue, S. Owada, T. Togashi, and E. Shigemasa. Observation of extreme ultraviolet superfluorescence from helium atoms ionised and excited using soft x-ray free-electron laser pulses. 2019.

[91] L. Mercadier, A. Benediktovitch, C. Weninger, M. A. Blessenohl, S. Bernitt, H. Bekker, S. Dobrodey, A. Sánchez-González, B. Erk, C. Bomme, et al. Extreme ultraviolet superfluorescence in Xenon and Krypton. *arXiv preprint arXiv:1810.11097*, 2018.

[92] S. Bhattacharyya and S. G. Nakhate. Visible superfluorescence from optically pumped europium atoms. *The European Physical Journal D*, 55:9, 2009.

[93] C. Brechignac and P. Cahuzac. Observation of two visible Dicke-superradiant transitions in atomic europium. *Journal de Physique Lettres*, 40:123–125, 1979.

[94] P. Cahuzac, H. Sontag, and P. E. Toschek. Visible superfluorescence from atomic europium. *Optics Communications*, 31:37–41, 1979.

[95] A. Flusberg, T. Mossberg, and S. R. Hartmann. Observation of Dicke superradiance at 1.30 μm in atomic Tl vapor. *Physics Letters A*, 58:373–374, 1976.

[96] E. Boursey, J. Meziane, and A. Topouzkhanian. Superfluorescence beats in $^{125}Te_2$ emission. *Physical Review A*, 48:3047–3050, 1993.

[97] S. Oullemine and E. Boursey. Perturbation spectroscopy in superfluorescent emission. *Quantum and Semiclassical Optics: Journal of the European Optical Society Part B*, 10:365–374, 1998.

[98] J. P. Girardeau-Montaut and G. Moreau. Optically pumped superfluorescence S_2 molecular laser. *Applied Physics Letters*, 36:509–511, 1980.

[99] M. Gross, C. Fabre, P. Pillet, and S. Haroche. Observation of near-infrared Dicke superradiance on cascading transitions in atomic sodium. *Physical Review Letters*, 36:1035–1038, 1976.

[100] Z. Kuprionis and V. vedas. Superradiating 4P-4S-3P cascade of sodium vapour arising on the leading edge of the exciting laser pulse. *Applied Physics B Laser and Optics*, 59:649–653, 1994.

[101] C. Cremer and G. Gerber. Observation of superfluorescence and stimulated emission in Bi I after nonresonant two-photon pumping. *Applied Physics B Photophysics and Laser Chemistry*, 35:7–10, 1984.

[102] Q. H. F. Vrehen, M. J. Hikspoors, H., and H. M. Gibbs. Quantum beats in superfluorescence in atomic Cesium. *Physical Review Letters*, 38:764–767, 1977.

[103] Q. H. F. Vrehen. Single-pulse superfluorescence in cesium. *Cooperative Effects in Matter and Radiation*, pages 79–100, 1977.

[104] J. Marek. Observation of superradiance in Rb vapour. *Journal of Physics B: Atomic and Molecular Physics*, 12, 1979.

[105] A. Crubellier, S. Liberman, and P. Pillet. Doppler-free superradiance experiments with Rb atoms: Polarization characteristics. *Physical Review Letters*, 41:1237–1240, 1978.

[106] K. Kitano and H. Maeda. Spatiotemporal profile of yoked superfluorescence from Rb vapor in the strong-excitation regime. *Physical Review A*, 97, 2018.

[107] D. Pavolini, A. Crubellier, P. Pillet, L. Cabaret, and S. Liberman. Experimental evidence for subradiance. *Physical Review Letters*, 54:1917–1920, 1985.

[108] A. Kumarakrishnan and X. L. Han. Superfluorescence from optically trapped calcium atoms. *Physical Review A*, 58:4153–4162, 1998.

[109] A. Kumarakrishnan, S. Chudasama, and X. L. Han. Collision-induced superfluorescence. *Journal of the Optical Society of America B*, 22:1538, 2005.

[110] C. Brechignac and P. Cahuzac. Population inversion on the resonance line of strontium by using cascading superfluorescences in a three-level system. *Journal of Physics B: Atomic and Molecular Physics*, 14:221–230, 1981.

[111] J. Okada, K. Ikeda, and M. Matsuoka. Streak camera investigation of superradiance development. *Optics Communications*, 27:321–323, 1978.

[112] M. A. Norcia, M. N. Winchester, Julia R. K. Cline, and J. K. Thompson. Superradiance on the millihertz linewidth strontium clock transition. *Science Advances*, 2:e1601231, 2016.

[113] Torben Laske, Hannes Winter, and Andreas Hemmerich. Pulse delay time statistics in a superradiant laser with Calcium atoms. *Physical Review Letters*, 123:103601, 2019.

[114] S. N. Andrianov, Y. V. Nabokin, V. V. Samartsev, N. B. Silaeva, and Y. E. Shebut. Optical superradiance in a diphenyl crystal with pyrene. *Soviet Physics Uspekhi*, 29:1060–1062, 1986.

[115] S. N. Andrianov, P. V. Zinov'ev, Y. V. Malyukin, Y. V. Naboikin, V. V. Samartsev, N. B. Silaeva, and Y. E. Sheibut. Effect of phonon disequilibrium on the optical Dicke super-radiance. *Zh. Éksp. Teor. Fiz*, 91:1990–2000, 1986.

[116] F. Sasaki, S. Kobayashi, S. Haraichi, H. Yanagi, S. Hotta, M. Ichikawa, and Y. Taniguchi. Pulse-shaped emissions with time delay in single crystals of Thiophene/Phenylene co-oligomers. *Japanese Journal of Applied Physics*, 45:L1206, 2006.

[117] A. Schiller, L. O. Schwan, and D. Schmid. Large-sample effects in superfluorescence of O_2 centers in KCl. *Journal of Luminescence*, 38:243–246, 1987.

[118] R. Florian, L. O. Schwan, and D. Schmid. Time-resolving experiments on dicke superfluorescence of O_2^- centers in KCl. Two-color superfluorescence. *Physical Review A*, 29:2709–2715, 1984.

[119] M. Ashida, O. Morikawa, H. Arai, and R. Kato. Superfluorescence of O_2^- centers in alkali halides. *Progress in Crystal Growth and Characterization of Materials*, 33:105–108, 1996.

[120] R. Florian, L. O. Schwan, and D. Schmid. Time-resolving experiments on Dicke superfluorescence of O_2 centers in KCl. two-color superfluorescence. *Physical Review A*, 29:2709–2715, 1984.

[121] M. Ashida, A. Kato, O. Morikawa, and R. Kato. Superfluorescence from O_2^- molecules in alkali halide crystals. *Journal of Luminescence*, 66-67:259–263, 1995.

[122] C. R. Ding, Z. L. Li, Z. R. Qiu, Z. C. Feng, and P. Becla. Observation of In-related collective spontaneous emission (superfluorescence) in $Cd_{0.8}Zn_{0.2}Te$:In crystal. *Applied Physics Letters*, 101:091115, 2012.

[123] D. C. Dai and A. P. Monkman. Observation of superfluorescence from a quantum ensemble of coherent excitons in a ZnTe crystal: Evidence for

spontaneous Bose-Einstein condensation of excitons. *Physical Review B*, 84, 2011.

[124] A. Angerer, K. Streltsov, T. Astner, S. Putz, H. Sumiya, S. Onoda, J. Isoya, W. J. Munro, K. Nemoto, J. Schmiedmayer, and et al. Superradiant emission from colour centres in diamond. *Nature Physics*, 14:1168–1172, 2018.

[125] K. Miyajima, K. Maeno, S. Saito, M. Ashida, and T. Itoh. Biexcitonic superfluorescence from CuCl quantum dots under resonant two-photon excitation. *Physica Status Solidi (c)*, 8:209–212, 2010.

[126] K. Cong, Y. Wang, J. Kim, G. T. Noe, S. A. Mcgill, A. Belyanin, and J. Kono. Superfluorescence from photoexcited semiconductor quantum wells: Magnetic field, temperature, and excitation power dependence. *Physical Review B*, 91:235448, 2015.

[127] G. Timothy N. Ii, J. Kim, J. Lee, Y. Wang, A. K. Wjcik, S. A. Mcgill, D. H. Reitze, A. A. Belyanin, and J. Kono. Giant superfluorescent bursts from a semiconductor magneto-plasma. *Nature Physics*, 8:219–224, 2012.

[128] G. Rain, M. A. Becker, M. I. Bodnarchuk, R. F. Mahrt, M. V. Kovalenko, and T. Stöferle. Superfluorescence from lead halide perovskite quantum dot superlattices. *Nature*, 563:671–675, 2018.

[129] D. C. Burnham and R. Y Chiao. Coherent resonance fluorescence excited by short light pulses. *Physical Review*, 188:667, 1969.

[130] M. S. Malcuit, Jeffery J. Maki, D. J. Simkin, and A. R. W. Boyd. Transition from superfluorescence to amplified spontaneous emission. *Physical Review Letters*, 59:1189–1192, 1987.

[131] R. Bonifacio, C. Maroli, and N Piovella. Slippage and superradiance in the high-gain FEL: Linear theory. *Optics communications*, 68:369–374, 1988.

[132] M. Yin and J.-C Krupa. Superfluorescence from $NdCl_3$. *Chemical Physics Letters*, 314:27–30, 1999.

[133] F. Auzel, S. Hubert, and D. Meichenin. Very low threshold cw excitation of superfluorescence at 2.72 μm in Er^{3+}. *Europhysics Letters (EPL)*, 7:459–462, 1988.

[134] S. Hubert, D. Meichenin, and F. Auzel. Thermal behaviour of low temperature coherent emission in $LiYF_4$:Er^{3+}. *Journal of Luminescence*, 45:434–436, 1990.

[135] F. Auzel. Coherent emission in rare-earth materials. *Handbook on the Physics and Chemistry of Rare Earths*, 22:507–606, 1996.